Evolution of Circumstellar Disk and Protostellar Structure in the Primordial Star Formation

Kazutaka Kimura

Abstract

In the present-day universe, various astronomical objects such as stars, galaxies, and black holes exist. However, tracing back to the beginning of the universe, there were no such objects, and the universe was in complete darkness, referred to as the Dark Ages. Indeed, observations of the Cosmic Microwave Background have revealed that density fluctuations were tiny just after the Big Bang. These fluctuations grow due to the gravitational interaction, leading to the formation of stars and galaxies. Theoretically, stars formed for the first time several hundred million years after the Big Bang, at redshift $z = 15$–30, and we call these stars as *primordial stars*, *first stars* or *Population III stars*.

Primordial stars play various roles in the evolutionary history of the universe, and understanding their formation processes and typical mass is necessary to elucidate their impact. In the early universe, H_2 molecules are the main coolants due to the lack of heavy elements, and the resultant thermal evolution of the pristine gas leads to the star-forming clouds with masses of $\sim 10^3\ M_\odot$. Moreover, under some special environments where the H_2 cooling is suppressed, primordial stars form from more massive clouds with masses of $\sim 10^5\ M_\odot$ via H atomic cooling. Therefore, primordial stars are expected to be more massive than stars in the present-day universe, where the typical cloud masses are $\sim 1\ M_\odot$. Especially in the case with H cooling, primordial stars can grow into supermassive stars, which are possible origins of the observed high-redshift supermassive black holes, and this formation pathway is called the direct collapse scenario.

However, to determine the final stellar masses, it is necessary to reveal how much of the gas eventually accretes to protostars. The cloud gas does not directly infall onto protostars due to its angular momentum. Alternatively, circumstellar disks appear, which leads to various phenomena such as disk fragmentation. Moreover, protostars also evolve while accreting the gas. If their radiation becomes significant as a result of the evolution of the protostellar structure, the radiative feedback halts the gas accretion.

In this thesis, we study the formation processes of primordial stars, focusing on the evolution of (i) circumstellar disks and (ii) protostellar structure. These ingredients affect the final stellar masses both in the ordinal case and the direct collapse scenario.

First, we investigate circumstellar disks using a newly developed one-dimensional non-steady disk model. Our model shows that the self-gravitating disk gradually expands as the envelope gas around protostars infalls onto the disk. We further find that the accretion rate onto the star is an order of magnitude smaller than the supply rate from the envelope. As a result, the disk becomes more massive than the central star in an early evolutionary stage, which leads to disk fragmentation. This evolutionary feature is observed for various parameters, including the normal primordial star formation and the direct collapse scenario. Moreover, we have performed a three-dimensional simulation to demonstrate the validity of our model. We confirm similar evolution occurs in the simulation, where the disk mass overcomes the stellar mass before the disk fragmentation. Our results suggest that the disk fragmentation generally occurs due to the emergence of

the massive disks in the primordial star formation.

Second, we study the primordial protostellar structure in the direct collapse scenario. We have developed a new radiation-hydrodynamic solver with an explicit M1 closure scheme to consistently solve the gas temperature, chemical abundances, and radiation fields, even in the stellar interior. We follow protostellar evolution until their masses reach $\sim 10\ M_\odot$ from two different initial configurations of spherical and turbulent clouds. We demonstrate that swollen protostars emerge as predicted by the previous one-dimensional stellar calculations. Such protostars have low effective temperatures and emit few ionizing photons, which results in too weak radiative feedback to disturb the gas accretion. Moreover, in the turbulent case, the protostar exhibits a rapid rotation of more than 0.4 times the Keplerian velocity. Our results indicate that we need to consider the rapid stellar rotation to clarify the protostellar evolution in the supermassive star formation.

Contents

Chapter 1

Introduction

1.1 Cosmic History

In modern cosmology, the universe has a beginning referred to as inflation, which drives the exponential expansion of the universe (see Figure 1.1). At the end of the inflation, the "reheating" phase converts the energy of the inflaton into radiation energy, and this transition leads to the Big Bang cosmology. Immediately after the Big Bang, there were no luminous objects in the universe, and this era is called the Dark Ages. After that, the density perturbation grows gradually owing to the gravitational interaction, and about a billion years later, the first luminous objects emerge. These are the so-called primordial stars. Subsequently, the first galaxies form, and their radiation induces the cosmic reionization. Finally, the universe has evolved to the current state over about 13 billion years. Elucidating this evolutionary history is one of the most fundamental problems in astrophysics.

With the James Webb Space Telescope (JWST) launched in 2021, we are now addressing the nature of star and galaxy formation in the early universe. Thanks to its high resolution and sensitivity, JWST has revealed the properties of many high-redshift galaxies (e.g. Harikane et al., 2022). Its observations imply the more existence of bright galaxies than expected by the standard cosmology (Boylan-Kolchin, 2023), and many theoretical studies have been devoted to solving this problem. Moreover, JWST places constraints on star formation activity, which favor the top-heavy initial mass function (IMF) or high star formation efficiency (Inayoshi et al., 2022). In the future, further observations will deepen our understanding of the early universe.

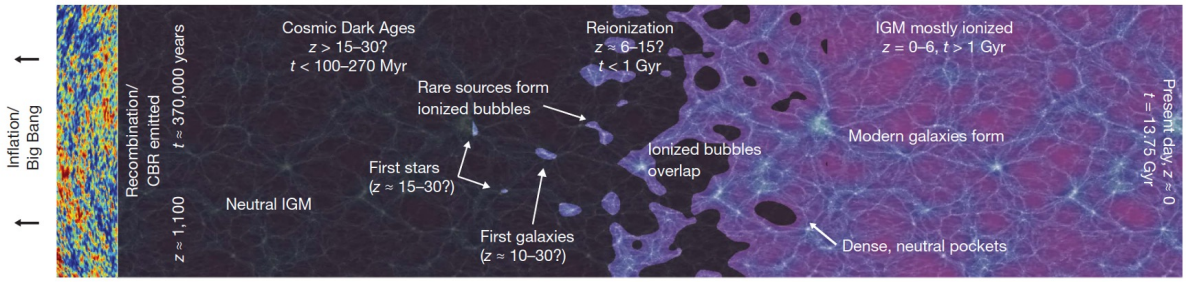

Figure 1.1: Shematic picture of the cosmic history. This figure is taken from Robertson et al. (2010).

In the cosmic evolution, stars are the most fundamental components playing various roles in the structure formation. First, their radiation heats and ionizes the interstellar medium (ISM). This feedback triggers the galactic outflow and prohibits star formation in neighbors. Furthermore, their supernova explosion spread the heavy elements into the primordial gas. This enrichment changes the thermochemical evolution of ISM significantly and leads to the formation of Pop II and I stars we can observe. It is thus necessary to elucidate primordial star formation, which is the main topic in this thesis, for understanding their roles in the subsequent cosmic evolution.

1.2 Star Formation Processes

Here, we briefly introduce how stars form for the subsequent discussion. Despite significant differences between the early and present-day universe, such as the abundance of metals, star formation follows almost the same processes in both environments. Figure 1.2 shows a schematic picture of these processes. Note that the interstellar medium has some angular momentum in general, and consequently, the star-forming clouds also rotate. We can divide the formation processes into two stages: the collapse phase and the accretion phase.

In the collapse phase, the cloud contracts due to the gravity. However, for contraction to continue, it is necessary to discard the thermal energy in the cloud. Otherwise, the pressure halts the gravitational collapse. Radiation from hydrogen molecules or atoms plays this role in the early universe because of the lack of metals. With this radiative cooling, the cloud continues the contraction until the protostellar birth with the timescale of the free-fall time,

$$t_{\rm ff} = \sqrt{\frac{3\pi}{32G\rho}}, \tag{1.1}$$

where ρ is the gas density, and G is the gravitational constant. Since $t_{\rm ff}$ is proportional

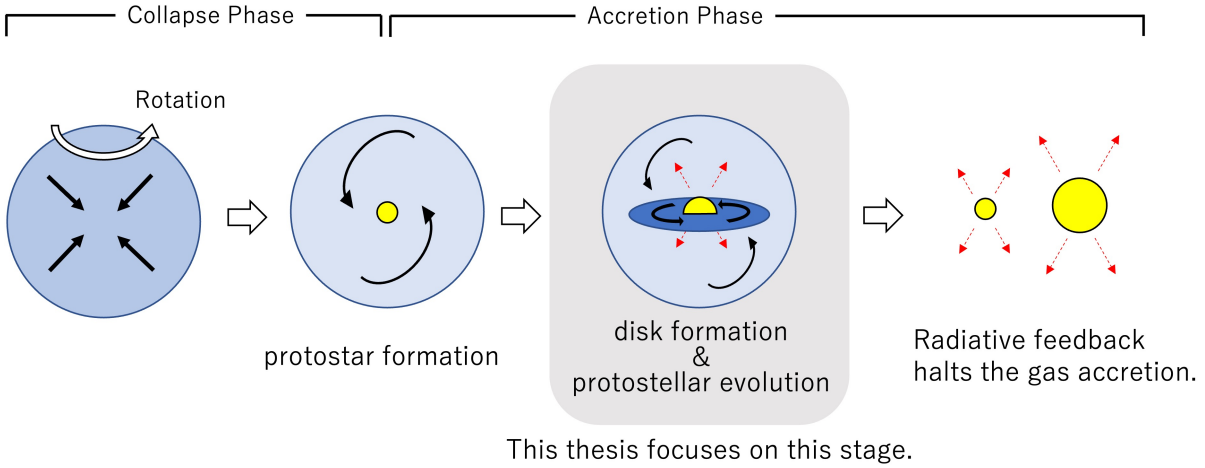

Figure 1.2: Schematic picture of primordial star formation from a rotating cloud. First, the cloud collapses to form a tiny protostar at the center. After that, envelope gas infalls while rotating, and circumstellar disks form. The disk often fragment and lead to multiple system. The protostar evolves while getting mass via disk accretion. Finally, the protostellar radiation halts the gas accretion.

to $\rho^{-1/2}$, the central part of the gas cloud with higher density collapses faster than the outer part, which is the so-called runaway collapse. As a result, a protostar forms at the center, and the leftover gas, called the envelope, surrounds it. The protostellar mass at this time is tiny compared to that of the entire cloud, ranging from 10^{-3}–10^{-1} $M_\odot$ solar masses.

After the collapse phase, the envelope gas infalls onto the center, increasing the protostellar mass. This stage is called the accretion phase. If the gas has angular momentum, it does not infall directly onto the protostar but forms a circumstellar disk. The disk gas rotates with Keplerian velocity due to the protostellar gravity. Since Keplerian rotation is the differential one, the viscous friction between adjacent gas transports the angular momentum within the disk, which results in the gas accretion onto the central protostar. Besides the angular momentum transport, the circumstellar disks play various roles in star formation. When much of the gas accumulates in the disks, they fragment, and multiple stellar systems emerge. Moreover, such disk fragmentation induces the variability of the accretion rate onto the central star. Recent observations reveal direct images of the disk formation and fragmentation in some nearby systems (Tobin et al., 2016; Ilee et al., 2018; Johnston et al., 2020). At the same time, the protostellar structure evolves due to the mass accretion via circumstellar disks during this stage. If the protostellar radiation becomes strong as a result of the evolution, it blows away the surrounding gas and halts its accretion, marking the end of the star formation. Previous theoretical studies of the primordial star formation show that, during this accretion phase, the disk dynamics and stellar evolution significantly affect the final state of the system, as mentioned in the following.

1.3 Primordial Stars

The initial state of the universe just after the Big Bang is well known through the standard cosmology and observations such as the cosmic microwave background (CMB). We can thus estimate when and where primordial stars form with the ab-initio calculations of matter evolution. Past theoretical studies show that primordial star formation begins within the dark matter (DM) minihalos with masses of $\sim 10^6$ $M_\odot$ at $z \sim 15$–30. Pristine gas collapses via H_2 cooling in these halos. As the H_2 cooling is efficient only for $T \gtrsim 200$ K, the temperature of the collapsing clouds cannot drop below ~ 200 K. This temperature is higher than the typical one in the present-day universe, ~ 10 K. The mass scale of the star-forming cloud can be estimated as Jeans mass,

$$M_{\rm Jeans} = \frac{c_s^3}{6}\left(\frac{\pi^5}{G^3\rho}\right)^{1/2} \propto T^{3/2}\rho^{-1}, \tag{1.2}$$

where $c_{\rm s}$ is the sound velocity, and T is the gas temperature. Moreover, we can roughly estimate the accretion rates onto a protostar by

$$\dot{M}_{\rm acc} \sim \frac{M_{\rm Jeans}}{t_{\rm ff}} \propto T^{3/2}. \tag{1.3}$$

Therefore, the high temperature in the primordial star formation leads to massive star-forming clouds and high accretion rates, which implies that primordial stars can grow up to massive stars during the accretion phase. As reviewed in Section 2.2.2, more detailed calculations about the thermal evolution of the pristine gas indicate that the typical mass

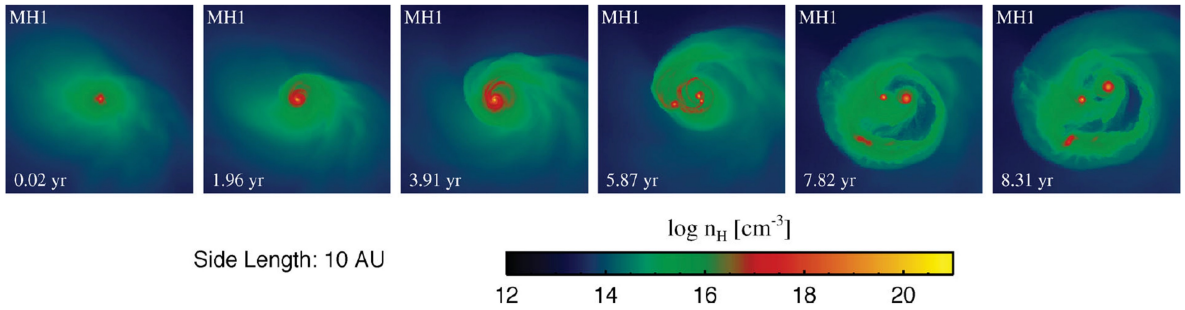

Figure 1.3: Simulation snapshots in the face-on view by Greif et al. (2012). The time after the first protostar formation is denoted at the lower-left corner of each panel.

scale and accretion rates are $\sim 10^3\ M_\odot$ and $\sim 10^{-3}\ M_\odot \mathrm{yr}^{-1}$ (Omukai & Nishi, 1998; Abel et al., 2002; Bromm et al., 2002; Omukai et al., 2005). These values are much larger than those in the present-day star formation, $\sim 1\ M_\odot$ and $\sim 10^{-5}\ M_\odot \mathrm{yr}^{-1}$.

Although primordial stars are expected to be massive from the above estimates, it is necessary to know how the circumstellar disks and protostars evolve for elucidating the IMF of primordial stars as shown in Figure 1.2. Many multi-dimensional simulations focusing on the accretion stage have recently been performed due to the increasing computational power. Multi-dimensional simulations are powerful tools to investigate the dynamics of the circumstellar disks, and they show that disk fragmentation generally occurs in the early universe (e.g. Turk et al., 2009; Stacy et al., 2010; Greif et al., 2012; Matsukoba et al., 2020; Sugimura et al., 2020). This trend lowers the stellar masses since the accreting gas is distributed to not a single star but multiple stars. For example, Figure 1.3 shows the simulation by Greif et al. (2012). They start calculations from the cosmological initial conditions. As seen in the figure, the circumstellar disk forms around the protostar, and the spiral arms develop. These spiral arms are gravitationally unstable and finally fragment. The binary system forms at the end of their simulation.

Protostellar evolution during the accretion stage has also been intensively studied so far. Unlike the disk evolution, the major methodology of studying protostellar evolution is 1D stellar evolution calculations (Hosokawa & Omukai, 2009a; Hosokawa et al., 2012a, 2013; Umeda et al., 2016; Haemmerlé et al., 2018a). This is because the timescale of the stellar interior is very short and it is not easy to follow the long-term evolution with multi-dimensional simulations. Figure 1.4 shows the primordial protostellar evolution for various constant accretion rates. The ordinal primordial star formation corresponds to the solid black line labeled with the accretion rates of $10^{-3}\ M_\odot \mathrm{yr}^{-1}$. Primordial protostars keep their radius more than ten times as large as the solar radius until their masses reach $\sim 10\ M_\odot$. After that, protostars contract by losing their thermal energy through radiation and evolve into main sequence stars. Their effective temperature then increases to $\sim 10^5$ K, and protostars emit a copious amount of extreme ultraviolet (EUV, $h\nu > 13.6$ eV) photons. These photons create an HII region around protostars, and its dynamical expansion due to the high gas pressure blows away the accreting gas (Tan & McKee, 2004; McKee & Tan, 2008; Hosokawa et al., 2011). This radiative feedback can regulate the protostellar masses to smaller values than the masses of the star-forming cloud. As the protostellar evolution changes with the accretion history, their final masses range from 10–$10^3\ M_\odot$ depending on the environments (Hirano et al., 2014).

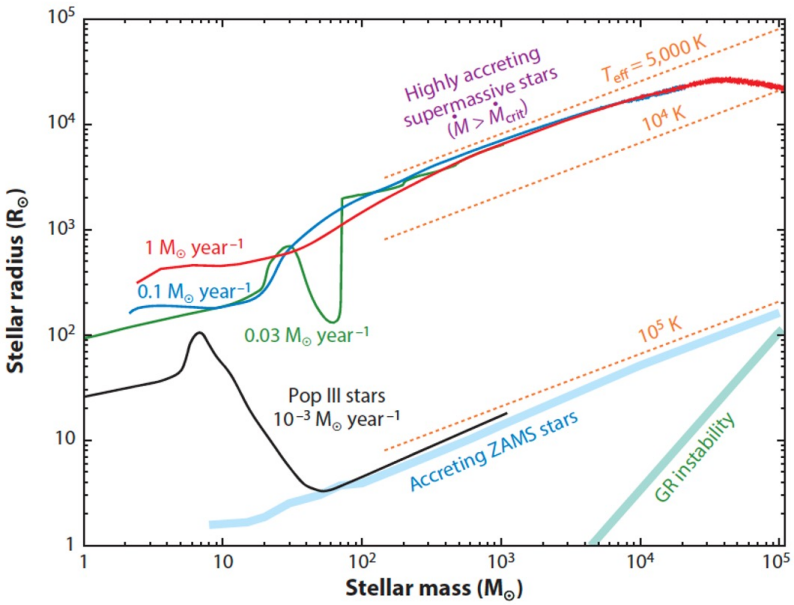

Figure 1.4: Evolution of the protostellar radius for various constant accretion rates. The black, green, blue, and red lines correspond to 10^{-3} $M_\odot \mathrm{yr}^{-1}$,0.03 $M_\odot \mathrm{yr}^{-1}$,0.1 $M_\odot \mathrm{yr}^{-1}$, and 1 $M_\odot \mathrm{yr}^{-1}$, respectively. The orange lines denote the effective temperature. The area below the green line indicates the GR instability regime. This figure is taken from Inayoshi et al. (2020).

1.4 Supermassive Stars

Recent observations have revealed the existence of supermassive black holes (SMBHs) with masses exceeding 10^9 $M_\odot$ at high redshifts of $z > 6$. Very efficient accretion processes are necessary to form such SMBHs from remnant black holes (BHs) from normal primordial stars, and whether these processes are possible or not is still under debate. Alternatively, primordial supermassive stars (SMSs) with masses of 10^4–10^5 $M_\odot$ in the early universe have drawn attention as another formation pathway of the high-redshift SMBHs. SMSs collapse due to the general relativistic (GR) instability and leave massive black holes with the same masses (Zeldovich & Novikov, 1971; Shapiro & Teukolsky, 1983; Shibata & Shapiro, 2002). Such remnant black holes can grow up to the observed SMBHs even if they grow at sub-Eddington rates. This formation scenario is called the direct collapse (DC) scenario (see Volonteri, 2010; Woods et al., 2019; Inayoshi et al., 2020, for reviews).

For the SMS formation, it is required to inhibit the normal primordial star formation by making H_2 cooling inefficient. Several mechanisms that prohibit the H_2 formation or suppress its cooling have been proposed, such as radiation from nearby galaxies, the relative velocity between the baryon and DM, and violent galaxy mergers (e.g. Omukai, 2001; Fernandez et al., 2014; Hirano et al., 2017). In this case, the pristine gas collapses via H atomic cooling. H atomic cooling is efficient for $T \gtrsim 8000$ K, and the star-forming cloud contracts with a higher temperature than in the normal primordial star formation. This thermal evolution leads to the larger mass scale and accretion rates from Equations (1.2) and (1.3). The detailed studies that investigate the thermal evolution of the atomic

cooling cloud indicate the realization of the collapse of massive clouds with the mass scale of $\sim 10^5\ M_\odot$ and the accretion rates of 0.1–1 $M_\odot \mathrm{yr}^{-1}$ (Omukai, 2001). If this rapid accretion onto the protostar continues for 10^6 yr, the typical lifetime of massive stars, the protostellar mass can reach $10^5\ M_\odot$.

Also in the context of the DC scenario, many authors have studied the accretion phase with multi-dimensional simulations, and they show that circumstellar disks form and fragment (Latif et al., 2013; Becerra et al., 2015; Sakurai et al., 2016; Chon et al., 2018; Latif et al., 2020; Matsukoba et al., 2020). Disk fragmentation may hinder the SMS formation. If too much fragmentation occurs, the star-disk system evolves into a stellar cluster instead of the single SMS (e.g., Regan & Downes, 2018). Additionally, disk fragmentation results in significant variability of the accretion rate, and this variability may strengthen the radiative feedback since the stellar evolution depends on the accretion rate (Sakurai et al., 2016).

Stellar evolution calculations indicate that protostars emit few ionizing photons under the high accretion rates realized in the DC scenario, as indicated by the blue or red solid lines in Figure 1.4. Since the rapidly accreting gas brings large entropy into the stellar interior, protostars cannot contract and keep their radius more than 100 times as large as solar radius. Such bloated protostars have a low effective temperature of several thousand Kelvin, and they continue growing without radiative feedback by EUV photons. Finally, when their masses reach $\sim 10^5\ M_\odot$, their core region, which contains most of the protostellar mass, enters the GR instability regime, and remnant massive black hole seeds form.

1.5 Organization of This Thesis

As mentioned above, the evolution of circumstellar disks and protostars during the accretion phase affects the final stellar masses in both the ordinal primordial star formation and the DC scenario. This thesis focuses on these evolutions, as shown in Figure 1.2.

First, we discuss the disk evolution based on the author's published paper, Kimura et al. (2021). We follow the evolution using a one-dimensional (1D) semi-analytic model. Compared to multi-dimensional simulations, 1D models are computationally less expensive and allow high-resolution and long-term calculations for various parameters (Tanaka & Omukai, 2014; Inayoshi & Haiman, 2014; Latif & Schleicher, 2015; Takahashi & Omukai, 2017; Matsukoba et al., 2019). They are also helpful for physical interpretation. However, most previous 1D models assume steady-state and constant accretion rates. The steady disk model cannot describe the mass evolution of the protostar and disk, which is one of the indicators of gravitational instability. Furthermore, their comparison with three-dimensional simulations was insufficient. Here, we have extended 1D models to non-steady ones and compared their results with 3D simulations. We find that the disk becomes more massive than the central star in the early stage of the accretion phase, which leads to disk fragmentation, and confirm that this actually occurs in 3D simulations.

Second, we have investigated the primordial protostellar evolution using 3D radiation hydrodynamic (RHD) simulations, following the author's accepted paper, Kimura et al. (2023). The main methodology of studying stellar evolution has been 1D stellar evolution calculations, which have some limitations. They generally assume the hydrostatic balance for the stellar materials and steady accretion flow, and it is difficult to model the stellar rotation accurately. Since there is some angular momentum and turbulence in the universe, the actual protostellar evolution may differ from what is predicted by 1D

calculations. We have developed a new RHD solver with an explicit M1 closure method and investigated the evolution of primordial protostar born from the collapsing cloud. In this thesis, we focus on the protostellar evolution in the DC scenario, under which the accretion rate is $\dot{M} \sim 1\ M_\odot \mathrm{yr}^{-1}$. We calculate until the protostellar mass reaches $\sim 10\ M_\odot$ and find that protostars born from the turbulent clouds have highly oblate shapes and rotate rapidly at more than 0.4 times Keplerian rotation. Our results suggest that rotation has an impact on the ensuing evolution of the star-disk system.

The rest of this thesis is organized as follows. In Chapter 2, we review previous works as a background for our works. We overview the cosmological structure formation in the early universe and how primordial stars form in this framework. In Chapter 3, we discuss the evolution of circumstellar disks using 1D non-steady disk models. In Chapter 4, we consider the primordial protostellar evolution using 3D radiation hydrodynamic simulations with a newly developed RHD solver. Chapter 5 is dedicated to summary and future direction.

Chapter 2

Review: Primordial Star Formation

In this chapter, we overview the primordial star formation in the early universe. The observation of CMB shows that, just after the Big Bang, only small density fluctuations exist and there are no structures such as stars and galaxies. These fluctuations gradually increase owing to the gravity. However, baryon fluctuations cannot initially grow due to the interaction with photons. On the other hand, DM fluctuations grow since they interact only through gravity. When the interaction between baryons and photons becomes weak enough through the recombination, the baryonic perturbations grow by the gravitational potential of already formed DM structures, the so-called DM halos. Furthermore, baryonic gas undergoes gravitational collapse within these DM halos and forms primordial stars.

In section 2.1, we discuss the growth of the DM density perturbations in the expanding universe and the properties of DM halos. In section 2.2, we briefly describe when and where primordial stars form and review the star formation processes focusing on the evolution of the circumstellar disks and protostars. In section 2.3, we overview the SMS formation and mechanisms triggering the DC scenario.

2.1 Cosmological Structure Formation

In this section, we overview the growth of DM fluctuations by dividing it into linear and nonlinear theories. We first discuss the linear theory. We consider the spatial fluctuations of non-relativistic matter in an expanding universe. While we can ignore pressure in the case of DM, we initially examine the general case including pressure and then eliminate the pressure term later. For simplicity, we neglect the effects of dark energy and curvature in the calculations.

2.1.1 Growth of Dark Matter Perturbation in Linear Theory

Assuming that the matter component is a perfect fluid with mass density ρ, velocity $\boldsymbol{v}$, pressure p, and gravitational potential ϕ, the equations of mass conservation and motion can be written as follows:

$$\frac{\partial \rho}{\partial t} + \boldsymbol{\nabla} \cdot (\rho \boldsymbol{v}) = 0, \tag{2.1}$$

$$\frac{\partial \boldsymbol{v}}{\partial t} + (\boldsymbol{v} \cdot \boldsymbol{\nabla}) = -\frac{\boldsymbol{\nabla} p}{\rho} - \boldsymbol{\nabla} \phi, \tag{2.2}$$

where $\boldsymbol{\nabla} = \boldsymbol{\partial}/\boldsymbol{\partial r}$. These equations are written in the static coordinates $\boldsymbol{r}$ independent of the cosmic expansion. We can rewrite them using the comoving coordinates $\boldsymbol{x} \equiv \boldsymbol{r}/a$, which moves along with the cosmic expansion. Here, a is the scale factor of the universe. As the velocity in the static frame is the sum of the cosmic expansion and the velocity in the comoving frame,

$$\dot{\boldsymbol{r}} = \dot{a}\boldsymbol{x} + a\dot{\boldsymbol{x}}, \tag{2.3}$$

where the overdot denotes the time derivative. While $\boldsymbol{v}$ in Equations (2.1) and (2.2) is the velocity in the static coordinates $\boldsymbol{r}$, we redefine the velocity $\boldsymbol{v}$ as one observed in the comoving frame. In this case, we should replace $\boldsymbol{v}$ in Equations (2.1) and (2.2) with $\boldsymbol{v} + \dot{a}\boldsymbol{x}$ from Equation (2.3). Furthermore, by transformation from the static coordinates to the comoving coordinates $(t, \boldsymbol{r}) \to (r, \boldsymbol{x})$, the partial derivatives are replaced as

$$\frac{\partial}{\partial t} \to \frac{\partial}{\partial t} - \frac{\dot{a}}{a}\boldsymbol{x} \cdot \boldsymbol{\nabla}, \quad \boldsymbol{\nabla} \to \frac{1}{a}\boldsymbol{\nabla}, \tag{2.4}$$

where the $\boldsymbol{\nabla}$ on the right-hand side is defined as $\boldsymbol{\nabla} = \boldsymbol{\partial}/\boldsymbol{\partial x}$. After applying these transformations, Equations (2.1) and (2.2) become

$$\frac{\partial \rho}{\partial t} + 3\frac{\dot{a}}{a}\rho + \frac{1}{a}\boldsymbol{\nabla} \cdot (\rho \boldsymbol{v}) = 0, \tag{2.5}$$

$$\frac{\partial \boldsymbol{v}}{\partial t} + \frac{\dot{a}}{a}\boldsymbol{v} + \frac{1}{a}(\boldsymbol{v} \cdot \boldsymbol{\nabla})\boldsymbol{v} = -\frac{1}{a}\boldsymbol{\nabla}\Phi - \frac{1}{a\rho}\boldsymbol{\nabla}p. \tag{2.6}$$

Here, Φ represents the gravitational potential in the comoving coordinates and can be expressed as

$$\Phi = \phi + \frac{1}{2}a\ddot{a}|\boldsymbol{x}^2|. \tag{2.7}$$

The second term represents the effect of the increasing (decreasing) density due to the expansion (contraction) of spacetime. To solve the above equation, the Poisson equation determining the gravitational potential Φ is necessary in addition to the equation of state of the matter. With the energy density $\varrho_{\rm tot}$ and pressure $p_{\rm tot}$ of all components in the universe, the Poisson equation in the static coordinates is given by

$$\Delta\phi = \frac{4\pi G}{c^2}(\varrho_{\rm tot} + 3p_{\rm tot}), \tag{2.8}$$

where c is the speed of light. From the Einstein equations of a homogeneous and isotropic spacetime, the spatially averaged total density $\bar{\varrho}_{\rm tot}$ and pressure $\bar{p}_{\rm tot}$ are related to the scale factor a as

$$\left(\frac{\dot{a}}{a}\right)^2 = \frac{8\pi G}{3c^2}\bar{\varrho}_{\rm tot}, \tag{2.9}$$

$$\frac{\ddot{a}}{a} = -\frac{4\pi G}{3c^2}(\bar{\varrho}_{\rm tot} + 3\bar{p}_{\rm tot}). \tag{2.10}$$

From the Equations (2.4), (2.7), (2.8), and (2.10), we can get the Poisson equation for the gravitational potential Φ in the comoving coordinates as follows:

$$\Delta\Phi = \frac{4\pi G a^2}{c^2}((\varrho_{\rm tot} + 3p_{\rm tot}) - (\bar{\varrho}_{\rm tot} + 3\bar{p}_{\rm tot})). \tag{2.11}$$

This equation shows that, in comoving coordinates of an expanding universe, only deviations from the mean value contribute to the gravitational potential.

Let us consider the fluctuations from the spatially averaged mass density $\bar{\rho}$ and pressure $\bar{p}$ throughout the universe. First, by spatially averaging Equation (2.5), we obtain

$$\frac{d}{dt}(a^3\bar{\rho}) = 0. \tag{2.12}$$

This equation means the mass conservation in the universe. Next, we define the density and pressure fluctuations as

$$\delta(\boldsymbol{x}, t) \equiv \frac{\rho(\boldsymbol{x}, t) - \bar{\rho}(t)}{\bar{\rho}(t)}, \tag{2.13}$$

$$\delta p(\boldsymbol{x}, t) \equiv p(\boldsymbol{x}, t) - \bar{p}(t). \tag{2.14}$$

By using equations (2.12), (2.13), and (2.14), we can rewrite Equations (2.5), (2.6), and (2.11) as

$$\frac{\partial \delta}{\partial t} + \frac{1}{a}\boldsymbol{\nabla}\cdot[(1+\delta)\boldsymbol{v}] = 0, \tag{2.15}$$

$$\frac{\partial \boldsymbol{v}}{\partial t} + \frac{\dot{a}}{a}\boldsymbol{v} + \frac{1}{a}(\boldsymbol{v}\cdot\boldsymbol{\nabla})\boldsymbol{v} = -\frac{1}{a}\boldsymbol{\nabla}\Phi - \frac{\boldsymbol{\nabla}(\delta p)}{a\bar{\rho}(1+\delta)}, \tag{2.16}$$

$$\Delta\Phi = \frac{4\pi G a^2}{c^2}(\bar{\varrho}_{\rm tot}\delta_{\rm tot} + 3\delta p_{\rm tot}), \tag{2.17}$$

where $\delta_{\rm tot}$ and $\delta p_{\rm tot}$ represent fluctuations in the energy density and pressure of all components. These equations describe the evolution of perturbations in an expanding universe.

Next, we consider the case where the perturbations are sufficiently small and keep only terms up to first order in $\delta\rho$, δp, and v. By adding equations that we can get by applying $\partial/\partial t + 2\dot{a}/a$ to (2.15) and $-a^{-1}\boldsymbol{\nabla}\cdot$ to (2.17), we obtain the following equation, which does not contain the velocity field:

$$\frac{\partial^2\delta}{\partial t^2} + 2\frac{\dot{a}}{a}\frac{\partial\delta}{\partial t} - \frac{\Delta(\delta p)}{a^2\bar{\rho}} = \frac{4\pi G}{c^2}\bar{\varrho}_{\rm tot}\delta_{\rm tot}. \tag{2.18}$$

This is the evolution equation for perturbations of non-relativistic matter. Neglecting the pressure term in (2.18), we obtain the following evolution equation for DM perturbations:

$$\frac{\partial^2\delta_{\rm dm}}{\partial t^2} + 2\frac{\dot{a}}{a}\frac{\partial\delta_{\rm dm}}{\partial t} = 4\pi G\bar{\rho}_{\rm tot}\delta_{\rm tot} \simeq 4\pi G\bar{\rho}_{\rm dm}\delta_{\rm dm}, \tag{2.19}$$

where $\bar{\rho}_{\rm tot}$ and $\delta_{\rm dm}$ are the averaged DM energy density and its fluctuations. Here, we approximate the right-hand side by the DM mass fluctuations. While baryons and photons exist in the universe in addition to DM, this approximation is valid in both the radiation dominant and matter dominated eras. This is because the perturbations of the radiation component cannot gravitationally grow within the horizon due to the strong pressure and DM is dominant compared to baryons.

Using Equation (2.19), we will examine how the fluctuations of DM grow from the radiation dominant era to the matter dominated era in the linear theory. From Equation (2.9), we obtain

$$\left(\frac{\dot{a}}{a}\right)^2 = \frac{8\pi G}{3c^2}(\rho_{\rm dm} + \rho_{\rm r}), \tag{2.20}$$

where $\rho_{\rm r}$ is the energy density of radiation component. By changing the time variable t to $y \equiv \rho_{\rm dm}/\rho_{\rm r} = a/a_{\rm eq}$, where $a_{\rm eq}$ is the scale factor when the energy density of the radiation and DM becomes equal, and using Equation (2.20), Equation (2.19) can be expressed as

$$\frac{d^2\delta_{\rm dm}}{dy^2} + \frac{2+3y}{2y(1+y)}\frac{d\delta_{\rm dm}}{dy} - \frac{3\delta_{\rm dm}}{2y(1+y)}. \tag{2.21}$$

The solution to this equation is given by

$$\delta_{\rm dm} \propto 1 + \frac{3y}{2}, \tag{2.22}$$

$$\delta_{\rm dm} \propto (1+\frac{3y}{2})\ln\left|\frac{\sqrt{1+y}+1}{\sqrt{1+y}-1} - 3\sqrt{1+y}\right|. \tag{2.23}$$

The first corresponds to the growth mode, while the second corresponds to the decay mode. We can understand how the DM fluctuations grow based on the growth mode. During the radiation dominated era, $a < a_{\rm eq}$ and thus $y < 1$, the fluctuations cannot grow significantly. On the other hand, during the matter dominated era, $a > a_{\rm eq}$ and thus $y > 1$, the fluctuations eventually become proportional to the scale factor.

2.1.2 Formation of Dark Matter Halos

In the above, we have considered fluctuations in the linear regime. However, as fluctuations grow, the linear theory finally breaks down. In the following, we examine the nonlinear growth of the fluctuations. Since it is difficult to fully treat the nonlinear theory, we discuss the spherically symmetric case. Note that even this simple model can describe the formation of astronomical objects in the actual universe.

Let us consider the motion of a spherical shell with radius $R(t)$, assuming that matter is spherically distributed. If we set the mass inside the shell as M, then the equation of motion for the shell is

$$\frac{dR(t)}{dt} = -\frac{GM}{R^2}. \tag{2.24}$$

Integrating this equation with respect to time yields the energy conservation law:

$$E = \frac{1}{2}\left(\frac{dR}{dt}\right)^2 - \frac{GM}{R}, \tag{2.25}$$

where E is the total energy of the shell. If $E > 0$, the shell is unbound and escapes to infinity. Since we are interested in the formation of DM halos, we assume $E < 0$ from now. In an expanding universe, a spherical shell initially has an outward velocity. The gravitational force eventually halts its expansion and causes the contraction. We can calculate the shell motion in this case by solving Equation (2.24) as follows:

$$R = A^2(1-\cos\theta), \tag{2.26}$$

$$t = \frac{A^3}{\sqrt{GM}}(\theta - \sin\theta), \tag{2.27}$$

$$A = \sqrt{\frac{R_{\rm turn}}{2}}, \tag{2.28}$$

where θ is an auxiliary variable and $R_{\rm turn}$ is the turning point at which the shell expansion stops. In the Einstein-de Sitter universe, as the averaged mass density is given by

$$\bar{\rho} = \frac{1}{6\pi G t^2}, \tag{2.29}$$

the magnitude of the density fluctuations inside the shell at time t is

$$\delta = \frac{\rho - \bar{\rho}}{\bar{\rho}} = \frac{3GMt^2}{2R^3} - 1. \tag{2.30}$$

The time when the shell reaches the turnaround point corresponds to $\theta = \pi$. At that time, the shell position, the time, and the density fluctuation inside the shell can be described as follows:

$$R_{\rm turn} = 2A^2, \tag{2.31}$$

$$t_{\rm turn} = \frac{\pi A^3}{\sqrt{GM}}, \tag{2.32}$$

$$\delta_{\rm turn} = \frac{9\pi^2}{16} - 1 \simeq 4.55. \tag{2.33}$$

Moreover, the shell reaches the origin, $R = 0$, and the density diverges at $\theta = 2\pi$. At that time, the shell position and time can be given by

$$R_{\rm coll} = 0, \tag{2.34}$$

$$t_{\rm coll} = \frac{2\pi A^3}{\sqrt{GM}}. \tag{2.35}$$

However, perfect spherical symmetry is actually impossible, and the density will not diverge. Alternatively, when the radius R becomes small enough, the velocity dispersion of DM becomes effective, and the system reaches virial equilibrium. Here, we discuss the radius and time when DM achieve the virial equilibrium. We denote the kinetic energy of DM by U and its gravitational potential energy by $\mathcal{W}$. If the system is in virial equilibrium, $2U_{\rm vir} + \mathcal{W}_{\rm vir} = 0$ from the virial theorem. On the other hand, at the turnaround point, the kinetic energy is zero. Thus, considering energy conservation, we have $U_{\rm vir} + \mathcal{W}_{\rm vir} = \mathcal{W}_{\rm turn}$. Combining these two equations, we obtain $\mathcal{W}_{\rm vir} = 2\mathcal{W}_{\rm turn}$ and therefore $R_{\rm vir} = R_{\rm turn}/2$. The time to reach the virial equilibrium is not exactly when the radius reaches $R_{\rm vir}$, but it should take more time. Therefore, we evaluate it by $t_{\rm coll}$ here. At this time, the magnitude of the fluctuation is given by

$$\delta_{\rm vir} = \frac{3M}{4\pi\bar{\rho}(t_{\rm coll})R_{\rm vir}^3} - 1 = 18\pi^2 - 1 \simeq 177. \tag{2.36}$$

Here, we examine how much the fluctuations virtually grow in the linear theory until the DM reaches the virial equilibrium in the nonlinear theory. Linearizing Equations (2.26) and (2.27), we can obtain

$$\delta_L(t) = \frac{3}{20}\left(\frac{6\sqrt{GM}}{A^3}t\right)^{2/3}. \tag{2.37}$$

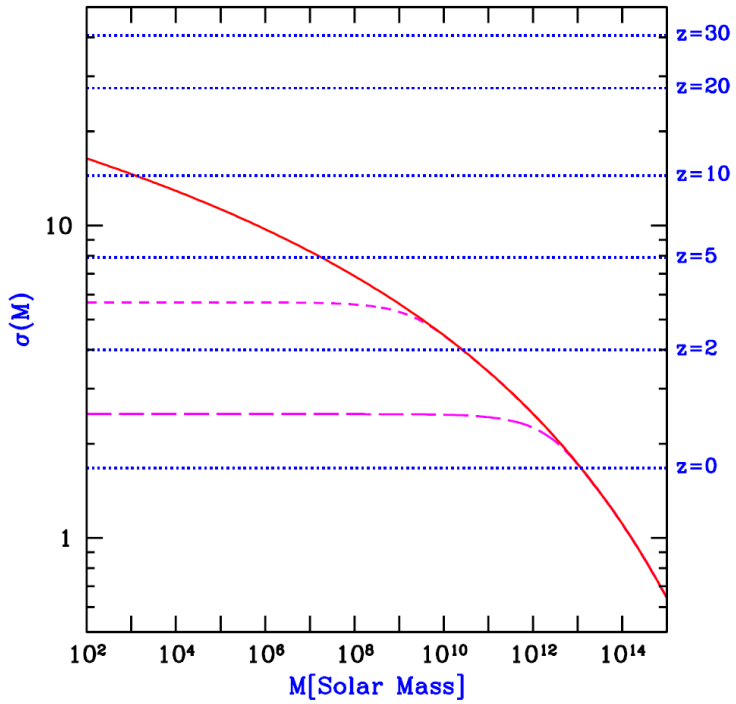

Figure 2.1: Relationship between the mass scale and variance of the fluctuations. The solid line shows results based on the given cosmological parameters, while the dashed lines denote the results in the case with a cutoff in the mass scale. The horizontal dotted lines show the variance that we can get by extrapolating 1.69 from the indicated redshifts to the present-day. This Figure is taken from Barkana & Loeb (2001)

Therefore, the amplitude of the fluctuations at $t_{\rm coll}$ is given by

$$\delta_L(t_{\rm coll}) = \frac{3(12\pi)^{2/3}}{20} \simeq 1.69. \tag{2.38}$$

In other words, when the fluctuation amplitude reaches 1.69 in the linear theory, the DM has achieved virial equilibrium.

In the above, we have discussed how fluctuations grow in linear and nonlinear theories. Form here, we now discuss what kind of DM halos are formed in the universe. Despite its nonlinearity, we can estimate it to some extent by combining linear and nonlinear theories. This method is called the Press-Schechter theory.

Let us consider a region with a radius R around a certain point in the universe. The average mass M in that region is given by $4\pi R^3\bar{\rho}/3$. We define the density fluctuations δ averaged over a sphere with radius R as δ_M, which is described as

$$\delta_M = \frac{3}{4\pi R^3}\int_{|\boldsymbol{x}|\le R} d^3\boldsymbol{x}\,\delta(\boldsymbol{x}). \tag{2.39}$$

This variance can be calculated as

$$\sigma^2(M) \equiv \langle(\delta_M)^2\rangle \tag{2.40}$$

$$= \int_{|\boldsymbol{k}|<1/R}\frac{d^3\boldsymbol{k}}{(2\pi)^3}\,P(k), \tag{2.41}$$

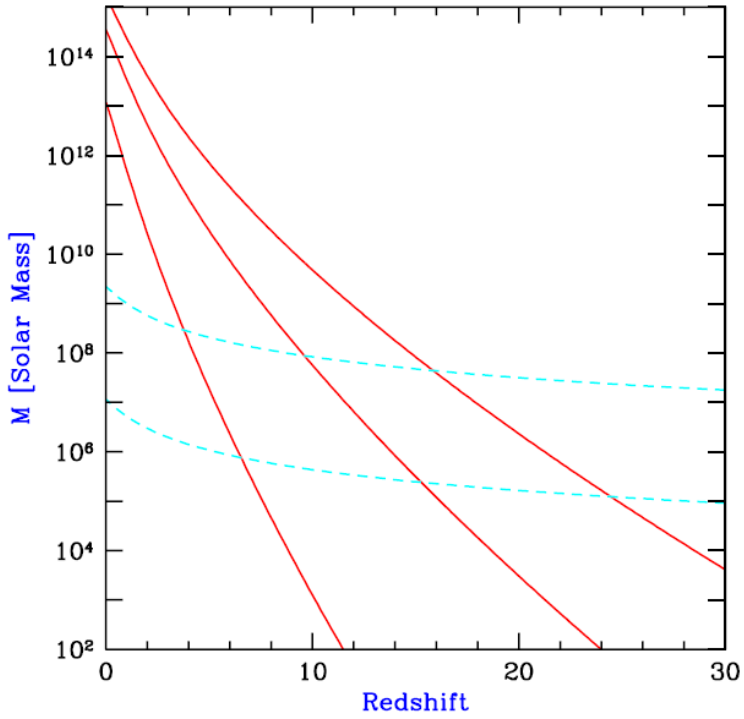

Figure 2.2: The relation between redshfts and the mass scale at which 1–3σ fluctuations have reached the virial equilibrium. The solid lines correspond to the cases of 1σ, 2σ, and 3σ from bottom to top. The dashed lines denote the mass scale with the temperature necessary for efficient cooling via only H atom (upper curve) or via additional H_2 molecules (lower curve), which discussed in Section 2.2.1. This figure is taken from (Barkana & Loeb, 2001)

where $\langle\ \rangle$ denotes the ensemble average, k is the wavenumber of the Fourier component, and $P(k)$ is the power spectrum. Here, we define $P(k)$ as

$$\langle\widetilde{\delta}(\boldsymbol{k})\widetilde{\delta}(\boldsymbol{k}')\rangle \equiv (2\pi)^3\delta_D^3(\boldsymbol{k}+\boldsymbol{k}')P(k), \tag{2.42}$$

where $\widetilde{\delta}(\boldsymbol{k})$ is the Fourier component of the density fluctuations, and δ_D^3 is the three-dimensional Dirac delta function. Figure 2.1 shows the variance $\sigma(M)$ obtained by extrapolating the fluctuations generated during inflation to the present-day with the linear theory. Note that they use the Lambda-Cold Dark Matter (Λ-CDM) model for the calculations. This figure shows that DM halos form in ascending order. This is a characteristic feature of structure formation in the Λ-CDM model.

As mentioned earlier, we assume that the system achieves the virial equilibrium when the amplitude of the fluctuations reaches $\delta_L(t_{\rm coll}) \simeq 1.69$ in the linear theory. Each dotted lines shows the present amplitude of the fluctuations whose variance has reached 1.69 at denoted redshift in the linear theory. For example, the dotted line labeled with $z = 5$ implies that 1-σ fluctuations with a mass scale of $\sim 2 \times 10^7 M_\odot$ have achieved the virial equilibrium at this redshift. Similar interpretations can be made for the other dotted lines. In addition, the fluctuations with a mass of $M \simeq 3 \times 10^{10} M_\odot$ has a variance half of the value of 1.69 at $z = 5$, indicating that the 2-σ fluctuations have reached the virial equilibrium. Figure 2.2 shows the mass scales at which fluctuations of $1\sigma, 2\sigma$, and 3σ have reached virial equilibrium with respect to the redshift.

Finally, we give the virial radius and temperature when the DM halos have achieved the virial equilibrium in the Einstein-de Sitter model (Barkana & Loeb, 2001). By solving the Equation (2.24) with a correction for the dark energy, we can obtain the following formulae:

$$R_{\rm vir} = 0.784 \left(\frac{M}{10^8 h^{-1}\ M_\odot}\right)^{1/3} \left[\frac{\Omega_m}{\Omega_m^z}\frac{\Delta_c}{18\pi^2}\right] \left(\frac{1+z}{10}\right)^{-1} h^{-1}\ {\rm kpc}, \tag{2.43}$$

$$\begin{aligned} T_{\rm vir} &= \frac{\mu m_{\rm p}}{2k_{\rm B}}\frac{GM}{R_{\rm vir}} \\ &= 1.98\times 10^4 \left(\frac{\mu}{0.6}\right) \left(\frac{M}{10^8 h^{-1}\ M_\odot}\right)^{2/3} \left[\frac{\Omega_m}{\Omega_m^z}\frac{\Delta_c}{18\pi^2}\right]^{1/3} \left(\frac{1+z}{10}\right)\ {\rm K}, \end{aligned} \tag{2.44}$$

$$h \equiv \frac{H_0}{100\ {\rm km/s/Mpc}}, \tag{2.45}$$

$$\Omega_k \equiv 1-(\Omega_m+\Omega_\Lambda+\Omega_r), \tag{2.46}$$

$$\Omega_m^z = \frac{\Omega_m(1+z)^3}{\Omega_m(1+z)^3+\Omega_\Lambda+\Omega_k(1+z)^2}, \tag{2.47}$$

$$\Delta_c = 18\pi^2 + 82(\Omega_m^z-1) - 39(\Omega_m^z-1)^2, \tag{2.48}$$

where Ω_m, Ω_Λ and Ω_r are the present contributions to the ratio of the total density to the critical density from matter, dark energy, and radiation, z is the redshift, H_0 is the Hubble constant, μ is the mean molecular weight, m_p is the proton mass, and $k_{\rm B}$ is the Boltzmann constant.

2.2 Formation Processes of Primordial Stars

2.2.1 Minimum Halo Mass for Star Formation

In this section, we focus on the baryonic component and discuss the condition for primordial star formation in the virialized DM halos. For star formation, the density must become sufficiently high due to the gravitational contraction of clouds. However, adiabatic contraction leads to an increase in the gas pressure, which prohibits star formation. For continuous collapse, clouds must efficiently radiate away their thermal energy. While metal and dust cooling dominate in the present-day universe, H atoms and H_2 molecules are alternative coolants in the early universe. Especially, most primordial stars form via H_2 cooling (Tegmark et al., 1997). In the following, we estimate the H_2 cooling rate along with the evolution of H_2 abundance and examine the properties of DM halos where primordial star formation occurs.

For star formation within virialized DM halos, the cooling timescale $t_{\rm cool}$ must be shorter than the Hubble time (cosmic age) at the redshifts of the halos. We can estimate

the Hubble time by

$$\begin{aligned} t_{\rm Hubble} &= \int_0^t dt = \int_z^\infty \frac{dz}{(1+z)H} = \frac{1}{H_0}\int_z^\infty \frac{dz}{(1+z)(H/H_0)} \\ &\simeq \frac{1}{H_0}\int_z^{z_{\rm eq}} \frac{dz}{(1+z)^{5/2}} \simeq \frac{2}{3H_0(1+z)^{3/2}} \\ &\simeq 6.5\times10^6\, h^{-1}\left(\frac{1+z}{100}\right)^{-3/2} \ {\rm yr}. \end{aligned} \tag{2.49}$$

Here, we neglect the integration over the radiation dominated era as the redshift of matter–radiation equality $z_{\rm eq} \simeq 3.129\times10^3$ is much larger than that when primordial star formation occurs. Moreover, we use the relation $H^2 = H_0^2(1+z)^3$, which holds in the matter dominated era.

Next, we estimate the H_2 cooling timescale. H_2 molecules have many excited levels corresponding to rotation and vibration. In the low density regime, almost all the H_2 molecules excited by collisions will return to the ground state via spontaneous emission. Since the collision rate per unit time is proportional to $n_{\rm H}^2$, the cooling rate Λ (in erg/s/cm^3) also scales as $\Lambda \propto n_{\rm H}^2$. On the other hand, in the high density regime, the H_2 molecules are in local thermal equilibrium due to collisions, and the level populations follow the Boltzmann's relation. Using the Einstein A coefficient $A_{\rm ul}$, which indicates the transition probability from a higher to a lower energy level, we can estimate the cooling rate as $\Lambda \propto n_{\rm u}A_{\rm ul} \propto n_{\rm H}$ where $n_{\rm u}$ is the number density of molecules in the upper energy level. In the temperature range of primordial star formation, 10^2 K $\lesssim T \lesssim 10^3$ K, the critical density at which the $n_{\rm H}$ dependency of Λ changes is $10^3 - -10^4$ cm^{-3}. The DM has achieved the virial equilibrium when the density fluctuation reaches $\delta_{\rm vir} \simeq 177$ from Equation (2.36). At this time, using the properties of virialized DM halos discussed in Section 2.1, the gas density can be given by

$$n_{\rm H} \approx 23\left(\frac{h^2\Omega_b}{0.015}\right)\left(\frac{1+z}{100}\right)^3 \ {\rm cm}^{-3}, \tag{2.50}$$

where Ω_b is the present contributions to the ratio of the total density to the critical density from the baryon. Therefore, we assume $\Lambda \propto n_{\rm H}$. In this case, the cooling rate can be described as follows (Hollenbach & McKee, 1979):

$$\Lambda \approx \frac{5}{4}\gamma_2(E_2-E_0)e^{-(E_2-E_0)/k_{\rm B}T} + \frac{7}{4}\gamma_3(E_3-E_1)e^{-(E_3-E_1)/k_{\rm B}T} \ {\rm erg\ cm^3\ s^{-1}}. \tag{2.51}$$

Here, $E_J = J(J+1)E_1/2$ where $E_1/k_{\rm B} \approx 171$ K. The γ_2 and γ_3 are the collisional de-excitation rates from the rotational levels with $J=2$ and $J=3$. Hydrogen molecules have two types of states depending on whether the nuclear spins are aligned (ortho) or anti-aligned (para). The first and second terms in Equation (2.51) represent the contribution from para and ortho states under the assumption that the ratio of ortho to para is a statistical weight ratio of 3:1. However, almost all ortho states change to para states through the chemical reaction,

$$H_2\ ({\rm ortho}) + H^+ \rightarrow H_2\ ({\rm para}) + H^+, \tag{2.52}$$

as reported by Abel et al. (1997). Thus, by multiplying the first term in (2.51) by 4, the cooling rate is given by

$$\Lambda \approx 5\gamma_2(E_2-E_0)e^{-(E_2-E_0)/k_{\rm B}T} \ {\rm erg\ cm^3\ s^{-1}}. \tag{2.53}$$

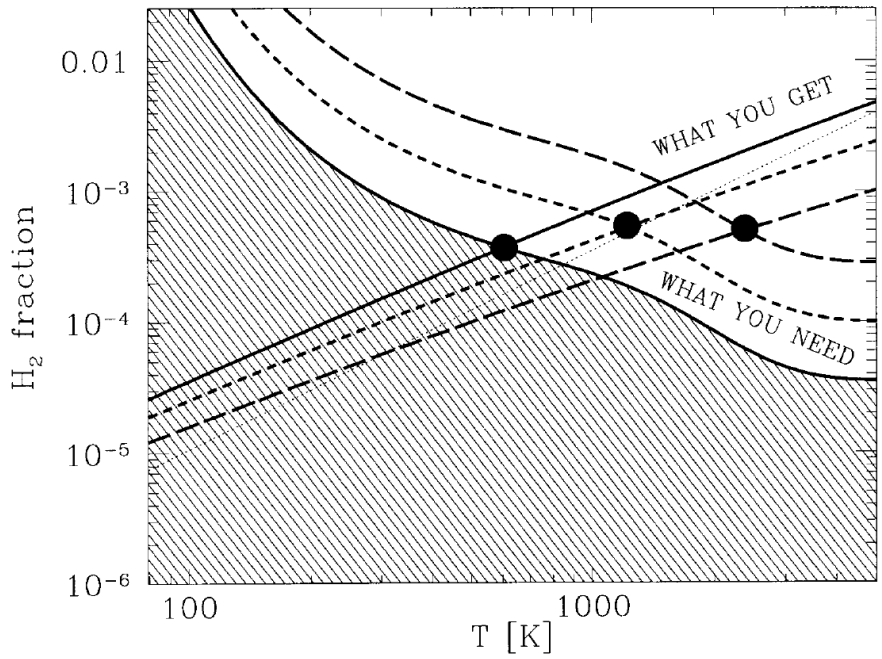

Figure 2.3: The downward sloping lines denote the necessary H_2 molecular fraction for primordial star formation. The upward sloping lines indicate the realized fraction in the early universe. The solid, short-dashed, and long-dashed lines correspond to the case where the DM halo has reached virial equilibrium at $z_{\rm vir} = 100, 50$, and 25, respectively. In the region above the shaded area, primordial star formation occurs within the Hubble time due to the H_2 molecular cooling. This figure is taken from Tegmark et al. (1997).

Using this equation, we can estimate the cooling timescale as

$$t_{\rm cool} \approx 4.82 \times 10^4 \left(1 + \frac{10T_3^{7/2}}{60 + T_3^4}\right)^{-1} e^{(512\ {\rm K}/T)} (f n_{\rm H})^{-1}\ {\rm yr}, \tag{2.54}$$

where $T_3 = T/1000$ K and f represents the hydrogen molecular fraction. With Equations (2.49), (2.50), and (2.54), we can rewrite the condition $t_{\rm cool} < t_{\rm Hubble}$ as follows:

$$f > 1.6 \times 10^{-4} \left(\frac{h\Omega_b}{0.03}\right) \left(\frac{1+z}{100}\right)^{-2/3} \left(1 + \frac{10T_3^{7/2}}{60 + T_3^4}\right)^{-1} e^{(512\ {\rm K}/T)}. \tag{2.55}$$

Figure 2.3 shows this condition. In the region above the shaded area, primordial star formation occurs due to the H_2 cooling within the Hubble time.

To investigate whether the Equation (2.55) is satisfied in the early universe, we discuss the amount of H_2 molecules formed by chemical reactions. In the following, we denote the number density of chemical species A as n(A). We consider the chemical reactions in Table 2.1. There are two formation channels for H_2. One is the H^- channel, where H^- is first formed through reaction (2). This H^- forms H_2 vis reaction (3). Meanwhile, the CMB radiation converts H^- back to H through reaction (6). When $k_2 \ll k_3, k_6$, reaction (2) is the rate-limiting step for the H_2 formation. As the H^- fraction that is used for H_2 formation is given by

$$\frac{n({\rm H}^-)n({\rm H})k_3}{n({\rm H}^-)n({\rm H})k_3 + n({\rm H}^-)k_6} = \frac{n({\rm H})k_3}{n({\rm H})k_3 + k_6}, \tag{2.56}$$

Table 2.1: Chemical reactions and their reaction rates k.

Reaction	Rate k (in cm^3 s^{-1})	Reference
(1) $H^+ + e^- \rightarrow H + h\nu$	$k_1 \approx 1.88 \times 10^{-10} T^{-0.64}$	Hutchins 1976
(2) $H + e^- \rightarrow H^- + h\nu$	$k_2 \approx 1.83 \times 10^{-18} T^{0.88}$	Hutchins 1976
(3) $H^- + H \rightarrow H_2 + e^-$	$k_3 \approx 1.3 \times 10^{-9}$	Hirasawa 1969
(4) $H^+ + H \rightarrow H_2^+ + h\nu$	$k_4 \approx 1.85 \times 10^{-23} T^{1.8}$	Shapiro & Kang 1987
(5) $H_2^+ + H \rightarrow H_2 + H^+$	$k_5 \approx 6.4 \times 10^{-10}$	Karpasb et al. 1979
(6) $H^- + h\nu \rightarrow H + e^-$	$k_6 \approx 0.114 T_\gamma^{2.13} e^{-8650/T_\gamma}$	Tegmark et al. 1997
(7) $H_2^+ + h\nu \rightarrow H + H^+$	$k_7 \approx 6.36 \times 10^5 e^{-71600/T_\gamma}$	Tegmark et al. 1997
(8) $e^- + h\nu \rightarrow e^- + h\nu$	$k_8 \approx 4.91 \times 10^{-22} T_\gamma^4$	

NOTE.— T and T_γ are the gas and CMB temperature. All temperatures are in Kelvin. Regarding the last three reactions, the reaction rates k are in units of s^{-1}.

the effective H_2 formation rate $k_{2,\rm eff}$ is

$$k_{2,\rm eff} = k_2 \frac{n(\rm H) k_3}{n(\rm H) k_3 + k_6}. \tag{2.57}$$

One additional pathway for the H_2 formation is H_2^+ process. The H_2^+ formation occurs first through reaction (4). The H_2^+ then form H_2 via reaction (5) or dissociate into H and H^+ through reaction (7). In the case where $k_4 \ll k_5, k_7$, reaction (4) is the rate-limiting step. Similar to before, the effective H_2 formation rate $k_{5,\rm eff}$ can be expressed as:

$$k_{4,\rm eff} = k_4 \frac{n(\rm H) k_5}{n(\rm H) k_5 + k_7}. \tag{2.58}$$

Therefore, the time evolution of the H_2 number density can be written as:

$$\frac{dn(\rm H_2)}{dt} = n(\rm H) n(e^-) k_{2,\rm eff} + n(\rm H) n(H^+) k_{4,\rm eff}. \tag{2.59}$$

As the abundance of H^- and H_2^+ is generally very small in the early universe, we assume $n(H^+) \approx n(e^-)$. Then, the evolution of the H_2 fractional abundance $f \equiv n(H_2)/n_{\rm H}$ can be expressed by

$$\begin{aligned} \frac{df}{dt} &= \frac{1}{n_{\rm H}} \frac{dn(\rm H_2)}{dt} - \frac{n(\rm H_2)}{n_{\rm H}^2} \frac{dn_{\rm H}}{dt} \\ &\approx (k_{2,\rm eff} + k_{4,\rm eff}) n_{\rm H} (1 - x - 2f) x, \end{aligned} \tag{2.60}$$

where $x \equiv n(H^+)/n_{\rm H}$. Since $n_{\rm H}$ remains approximately constant, we neglect its time variation. In the high-redshift universe ($z \gg 200$), the CMB temperature is so high that CMB radiation destroys H_- without forming H_2 via reaction (6). Therefore, the H_2^+ process dominates. In the later stage ($z \ll 100$), $k_4 \ll k_2$, and the H^- process is dominant. To solve Equation (2.60), it is necessary to determine the ionization fraction of hydrogen, x. With the approximation of $n(H^+) \approx n(e^-)$, the evolution of x can be given by

$$\frac{dx}{dt} = -k_1 n_{\rm H} x^2. \tag{2.61}$$

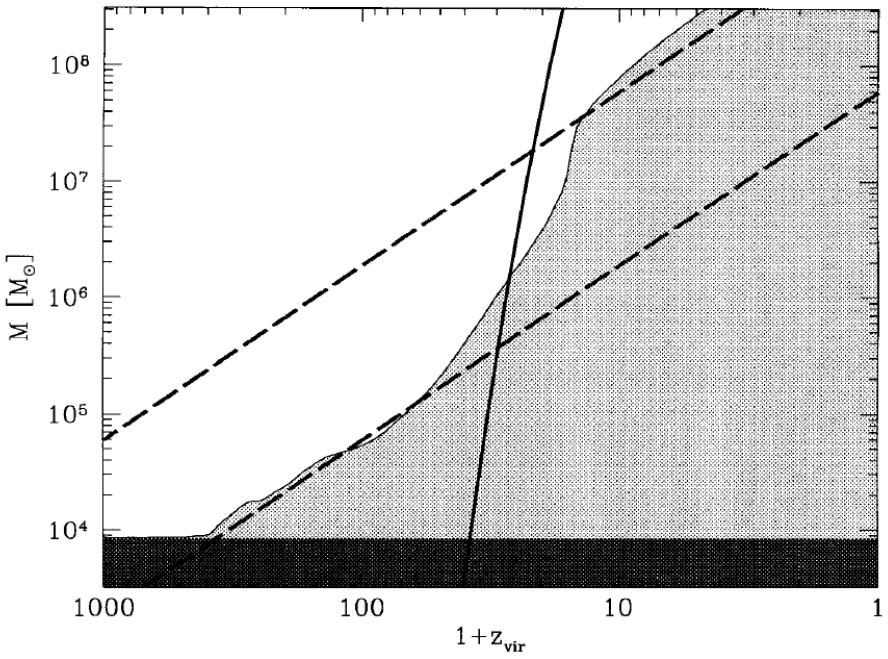

Figure 2.4: The horizontal and vertical axes represent the redshift and the mass scale of the fluctuation. The shaded region indicates the range where star formation cannot occur due to the lack of cooling. The lower black region denotes the regime where the halo temperature is lower than the CMB temperature and the cooling is inefficient. The solid line indicates the mass scale at which more than 3σ fluctuations reach virial equilibrium. The dashed lines correspond to $T_{\rm vir} = 10^4$K (upper) and $T_{\rm vir} = 10^3$K (lower), respectively. This figure is taken from (Tegmark et al., 1997).

Solving Equations (2.60) and (2.61), we can get the value of f, which corresponds to the upward sloping lines in Figure 2.3. For each redshift, star formation occurs in the DM halo with a higher virial temperature than that indicated by the black circles. Based on the above discussion, we can estimate in what kind of DM halo star formation occurs in the standard CDM model ($\Omega_b = 0.06$). Figure 2.4 shows this result. Primordial star formation occurs within a DM halo with the mass of $\sim 2 \times 10^6 M_\odot$ at $z \approx 30$. At this time, the gas mass within the halo is about $\Omega_b \times 2 \times 10^6 M_\odot \simeq 10^5 M_\odot$.

2.2.2 Thermal Evolution of Primordial Cloud

In the above, we have examined in what mass scale of the DM halo cooling becomes effective and star formation occurs. In this section, we overview the thermal evolution of the collapsing gas based on the one-zone model by Omukai et al. (2005).

The one-zone model focuses on the central core during the gravitational collapse. First, using the specific internal energy e, density ρ, pressure p, and the net energy loss through radiation and chemical reactions $\Lambda_{\rm net}$, the energy equation can be written as:

$$\frac{de}{dt} = -p\frac{d}{dt}\frac{1}{\rho} - \Lambda_{\rm net}. \tag{2.62}$$

(2.63)

The first term on the right-hand side represents the compressional heating due to the gravitational contraction. Furthermore, with the mean molecular weight μ and the adiabatic index $\gamma_{\rm ad}$, we can express e and p can as

$$p = \frac{\rho k_{\rm B} T}{\mu m_H}, \tag{2.64}$$

$$e = \frac{1}{\gamma_{\rm ad} - 1} \frac{k_{\rm B} T}{\mu m_{\rm H}}, \tag{2.65}$$

where $m_{\rm H}$ is the mass of a hydrogen nucleus. The net energy loss $\Lambda_{\rm net}$ consists of three main components as follows:

$$\Lambda_{\rm net} = \Lambda_{\rm line} + \Lambda_{\rm cont} + \Lambda_{\rm chem}, \tag{2.66}$$

where $\Lambda_{\rm line}$ is the line cooling, $\Lambda_{\rm cont}$ is the continuum cooling, and $\Lambda_{\rm chem}$ is the net cooling by chemical reactions. In addition to Equation (2.62), which determines the temperature evolution, we need an equation for the density evolution. Based on the Larson's self-similar solution, we calculate density evolution by

$$\frac{d\rho}{dt} = \frac{\rho}{t_{\rm col}}, \tag{2.67}$$

$$\text{where} \quad t_{\rm col} = \frac{1}{\sqrt{1-f}} t_{\rm col,0}, \tag{2.68}$$

$$t_{\rm col,0} = \sqrt{\frac{3\pi}{32 G \rho}}. \tag{2.69}$$

Here, $t_{\rm col,0}$ represents the timescale for collapse without the pressure, referred to as the free-fall time, and f denotes the ratio of the pressure gradient force to gravity. When these forces become equal in magnitude ($f = 1$), $t_{\rm col}$ diverges to infinity. Fitting the numerical calculations of the Larson's self-similar solution, f is expressed by

$$f = \begin{cases} 0, & (\gamma < 0.83), \\ 0.6 + 2.5(\gamma - 1) - 6.0(\gamma - 1)^2, & (0.83 < \gamma < 1), \\ 1.0 + 0.2(\gamma - 4/3) - 2.9(\gamma - 4/3)^2, & (\gamma > 1). \end{cases} \tag{2.70}$$

In order to evaluate the amount of radiation escaping from the gas cloud, we need the optical depth of the system τ. With the central density ρ and the Jeans length $\lambda_J = c_s \sqrt{\pi / G\rho}$, which is the typical size of the core, τ can be estimated as

$$\tau = \kappa_\nu \rho \lambda_J, \tag{2.71}$$

where κ_ν is the opacity. While solving the chemical reactions and radiative cooling to get $\Lambda_{\rm net}$, We can obtain the evolution of the density $n_{\rm H}$ and temperature T from Equations (2.62) and (2.67).

We show the results in Figure 2.5. First, as the density increases, the temperature increases due to the compressional heating, and H_2 molecules form. When the temperature reaches approximately 10^3 K, the H_2 cooling becomes effective. As mentioned in Section 2.2.1, at low densities, the H_2 cooling rate is proportional to $n_{\rm H}^2$, causing the temperature to decrease as the cloud contracts. When the density reaches $n \simeq 10^4$ cm^{-3}, the H_2 molecules achieve local thermal equilibrium and the cooling rate increases linearly with

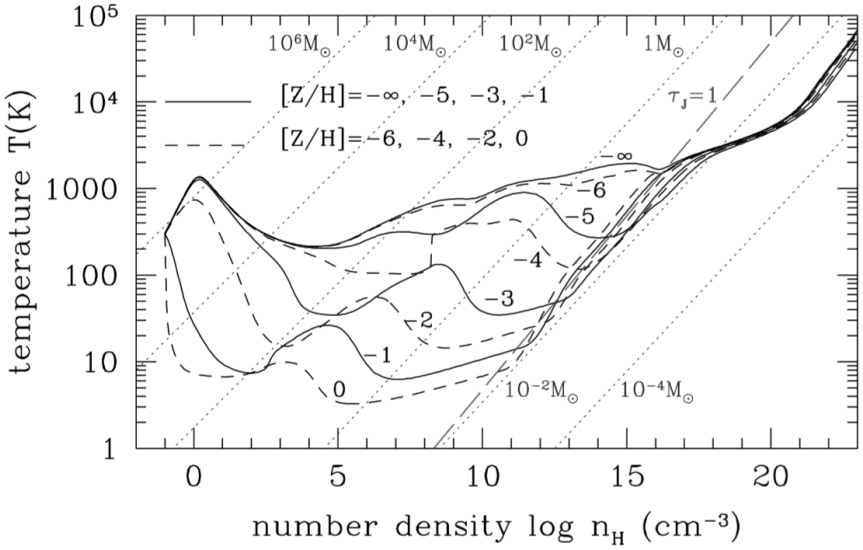

Figure 2.5: The thermal evolution of the collapsing gas clouds for various metallicities. The horizontal axis is the hydrogen number density. The vertical axis is the temperature. The diagonal dashed line represents the constant Jeans mass. This figure is taken from (Omukai et al., 2005).

the density. From this point, the cooling rate per unit mass becomes constant, and the temperature rises due to compressional heating.

Based on this temperature evolution, we discuss the fragmentation of the gas cloud. In regions where the density is $n < 10^4$ cm^{-3}, the temperature decreases due to H_2 cooling. As a result, an effective specific heat ratio $\gamma_{\rm eff}$ is less than unity. Since the critical specific heat ratio for filamentary gas clouds is unity, the gas collapses while maintaining the filamentary structure during this period (Inutsuka & Miyama, 1992). On the other hand, when the density exceeds $n > 10^4$ cm^{-3}, the temperature increases with the effective specific heat ratio $\gamma_{\rm eff} \simeq 1.1$. As the specific heat ratio exceeds 1, the filamentary collapse stops due to the pressure. Alternatively, as the critical specific heat ratio for spherical clouds is $\gamma_{\rm crit} = 4/3$, the filamentary gas fragments and collapses spherically. Finally, these fragments contract until the gas becomes adiabatic and protostars form at $n_{\rm H} \simeq 10^{21}$ cm^{-3}. Using the Jeans mass when the fragmentation occurs, we can evaluate the mass scale of these fragments as

$$M_{\rm Jeans} = \frac{c_s^3}{6}\left(\frac{\pi^5}{G^3\rho}\right)^{1/2} \simeq 10^3\ M_\odot\ \left(\frac{T}{250\ {\rm K}}\right)^{3/2}\left(\frac{n_{\rm H}}{10^4\ {\rm cm}^{-3}}\right)^{-1}. \tag{2.72}$$

Moreover, we can estimate the accretion rates in this fragmented cloud with

$$\dot{M} \sim \frac{M_{\rm Jeans}}{t_{\rm freefall}} \sim \frac{c_s^3}{G} \sim 10^{-3}\ M_\odot {\rm yr}^{-1}\ \left(\frac{T}{250\ {\rm K}}\right)^{3/2}. \tag{2.73}$$

These mass scale and accretion rates are much larger than the typical values in the present-day star formation, 1 $M_\odot$ and 10^{-5} $M_\odot$yr^{-1}. If the gas accretion onto the protostar continues for 10^6 yr, the typical lifetime of massive stars, the protostellar mass can reach 10^3 $M_\odot$. However, for elucidating the actual mass distribution of primordial stars, we need to understand the disk and protostellar evolution during the accretion phase as seen in the following sections.

2.2.3 Disk Fragmentation

In the subsequent accretion phase after the protostellar birth, the gas infalls onto the center from the envelope, and the circumstellar disks emerge, as shown in Figure 1.2. Many simulations have demonstrated that the circumstellar disks around primordial stars often fragment. These fragments follow various evolution paths, which complicate primordial star formation. Some fragments undergo rapid inward migration due to the gravitational interaction with the disk gas and finally merge with the central star. Others migrate outward and stay in the disk for a long time (Hirano & Bromm, 2017; Chon & Hosokawa, 2019). If the binaries with enough small separations are formed, they may evolve into the black hole binaries that emit gravitational waves within the Hubble time. These binaries are the possible origin of the massive black hole binaries observed with gravitational waves (Kinugawa et al., 2014; Hartwig et al., 2016). If the star clusters emerge due to the fragmentation, the binary orbits can shrink by N-body interaction (Hong et al., 2018; Kumamoto et al., 2020; Tanikawa et al., 2020; Liu et al., 2020). Moreover, this N-body interaction may eject some protostars from the cluster. Notably, if a star with a mass lower than 0.8 $M_\odot$ is ejected, it remains on the main sequence even in the present-day universe (Ishiyama et al., 2016).

Many previous studies have investigated disk dynamics. In particular, understanding the conditions for disk fragmentation has been one of the main problems. An often used indicator for disk fragmentation is the Toomre Q parameter,

$$Q \equiv \frac{c_s \kappa}{\pi G \Sigma}, \tag{2.74}$$

where κ is the epicyclic frequency of the disk and Σ is the disk surface density (Toomre, 1964). The linear analysis with some assumptions implies that the perturbation in the disk is gravitationally unstable when $Q < 1$, which is called the Toomre criterion. On the right hand side in Equation (2.74), the denominator represents the destabilization due to self-gravity. In contrast, the numerator represents the stabilization by the gas pressure and rotation. The 3D simulations that follow the disk evolution around primordial stars also demonstrate the Toomre Q parameter drops below unity at the places where disk fragmentation occurs (Clark et al., 2011; Greif et al., 2012)

However, the criterion based on Toomre Q parameter cannot describe disk fragmentation completely. While the analysis deriving the Toomre criterion is based on the linear theory, disk fragmentation is a nonlinear process. It is not obvious whether perturbations unstable according to the Toomre criterion will eventually lead to fragmentation. There is the possibility that the unstable modes saturate at some amplitude. Furthermore, their analysis is applicable only to the geometrically thin disk and limited to the axisymmetric mode. The finite disk thickness stabilizes the disk by diluting the self-gravity (Vandervoort, 1970; Bertin, 2000; Binney & Tremaine, 1987), and non-axisymmetric mode with $m = 1$ rapidly grows when the disk is so massive that the central protostar no longer stays at the center of the system (SLING instability, Adams et al., 1989; Shu et al., 1990). Actually, Greif et al. (2012) show that the circumstellar disk around primoridal stars does not necessarily fragment at the location of $Q < 1$.

In simulations that solve the self-gravity of the circumstellar disk, spiral arms emerge when the Toomre Q parameter approaches unity, as shown in Figure 2.6. These spiral arms transport angular momentum and facilitate the gas accretion through the gravitational torque, stabilizing the disk (Lynden-Bell & Kalnajs, 1972; Binney & Tremaine, 1987).

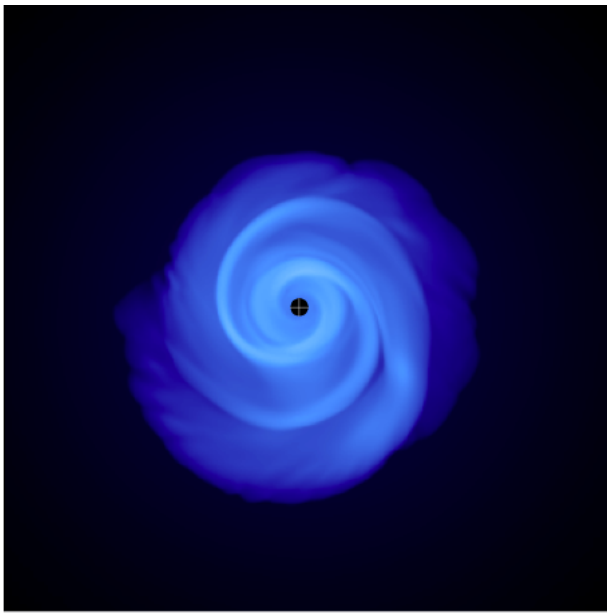

Figure 2.6: Snapshot of 3D hydrodynamic simulation by Kratter & Lodato (2016) that follows the disk evolution under the mass supply from the envelope. The black circle with plus sign denotes the position of the sink particles corresponding to the protostar. In this simulation, the disk avoids fragmentation, although Toomre Q value has a minimum value less than unity.

With the Poisson equation, we can rewrite the gravitational force as

$$\begin{aligned} -\rho\boldsymbol{\nabla}\Psi &= -\frac{1}{4\pi G}(\nabla^2\Psi)(\boldsymbol{\nabla}\Psi) \\ &= -\mathrm{div}\ \boldsymbol{T}, \end{aligned} \tag{2.75}$$

where Ψ is the gravitational potential and $\boldsymbol{T}$ is the followng stress tensor

$$T_{ij} = \frac{1}{4\pi G}(\partial_i\Psi)(\partial_j\Psi) - \frac{(\partial_k\Psi)^2}{8\pi G}\delta_{ij}. \tag{2.76}$$

Here, δ_{ij} is the Kronecker delta function, and k is the summation index. We can estimate the angular momentum flux by the gravitational force at disk radius r as follows:

$$\int rT_{\phi r}\ dS \propto \int (\partial_\phi\Psi)(\partial_r\Psi)\ dS, \tag{2.77}$$

where dS is the area element directed outward. When the spiral arms are trailing, the sign of $(\partial_\phi\Psi)(\partial_r\Psi)$ is always positive, and the gravitational torque transport the angular momentum outward.

The gravitational stability of disks with spiral arms depends on various factors, and many authors have investigated the fragmentation condition (see Kratter & Lodato, 2016, for review). If the mass supply rates from the envelope are larger than the accretion rates within the disk by the gravitational torque, the disk fragments due to the gas accumulation. The gas thermal evolution also affects the gravitational stability (Gammie, 2001). The gas with a low specific heat ratio is more prone to fragmentation as the pressure against the collapse is weak. Takahashi et al. (2016) perform the linear analysis

for the self-gravitating spiral arms and show that spiral arms with $Q < 0.6$ fragment. This criterion is consistent with their two-dimensional simulations that follow the disk evolution. Kratter et al. (2010) conduct numerical experiments for various parameters of collapsing clouds and find that the disk-to-star mass ratio $\xi \equiv M_{\rm disk}/M_*$ is the quantity related to the disk stability. While the disk with higher ξ is more stable as the disk gas can spread in the z-direction due to the disk thickness, the disk with $\xi \gtrsim 1$ eventually framents.

2.2.4 Protostellar Evolution

Protostellar masses increase due to the gas accretion via circumstellar disks. At their birth, protostellar masses are tiny and only $10^{-3}\ M_\odot$, which is the Jeans mass scale when the gas becomes adiabatic at $n_{\rm H} \sim 10^{22}\ {\rm cm}^{-3}$. As mentioned in Section 2.2.2, protostars can grow up to $\sim 10^3\ M_\odot$ if the accretion continues for the stellar lifetime. However, accretion does not necessarily continue for such a long time. As protostars grow, their luminosity increases, and in some cases, they begin to emit a copious amount of ionizing photons. These photons ionize and heat the surrounding gas, acting as feedback on the accretion (Tan & McKee, 2004; McKee & Tan, 2008; Hosokawa et al., 2011). As shown in Figure 2.7, Hosokawa et al. (2011) demonstrates that protostellar radiation creates an HII region around primordial stars, and its expansion blows away the surrounding gas. This feedback regulates the protostellar masses only to $\sim 40\ M_\odot$ in their simulation. Therefore, for elucidating primordial stellar masses, it is necessary to understand how the accreting protostars evolve and how many ionizing photons they emit. In this section, we review the evolution of primordial accreting protostars based on Hosokawa & Omukai (2009b).

To understand stellar evolution, we introduce two timescales at first. One is the accretion timescale, over which the protostellar mass grows by accretion,

$$t_{\rm acc} = \frac{M_*}{\dot{M}_*}, \tag{2.78}$$

where M_* is the protostellar mass and $\dot{M}_*$ is the accretion rate onto the protostar. Another one is the Kelvin-Helmholtz timescale, over which protostars lose their entropy through their radiation,

$$t_{\rm KH} = \frac{GM_*^2}{R_* L_*}, \tag{2.79}$$

where R_*, and L_* are protostellar radius and luminosity. We note that there are two types of luminosity for protostars: interior and accretion luminosity. The former originates from the stellar interior, while the latter from the accretion shock at the stellar surface. Assuming that nearly all the thermal energy released at the surface is radiated away, accretion luminosity can be expressed as

$$L_{\rm acc} = \frac{GM_*\dot{M}_*}{R_*}. \tag{2.80}$$

When $t_{\rm acc} < t_{\rm KH}$, the accretion properties determine the evolution. In the opposite case, the radiative energy loss controls the evolution. As for primordial star formation, $t_{\rm acc}$ is shorter than $t_{\rm KH}$ in the beginning owing to the large accretion rates of $10^{-3}\ M_\odot {\rm yr}^{-1}$.

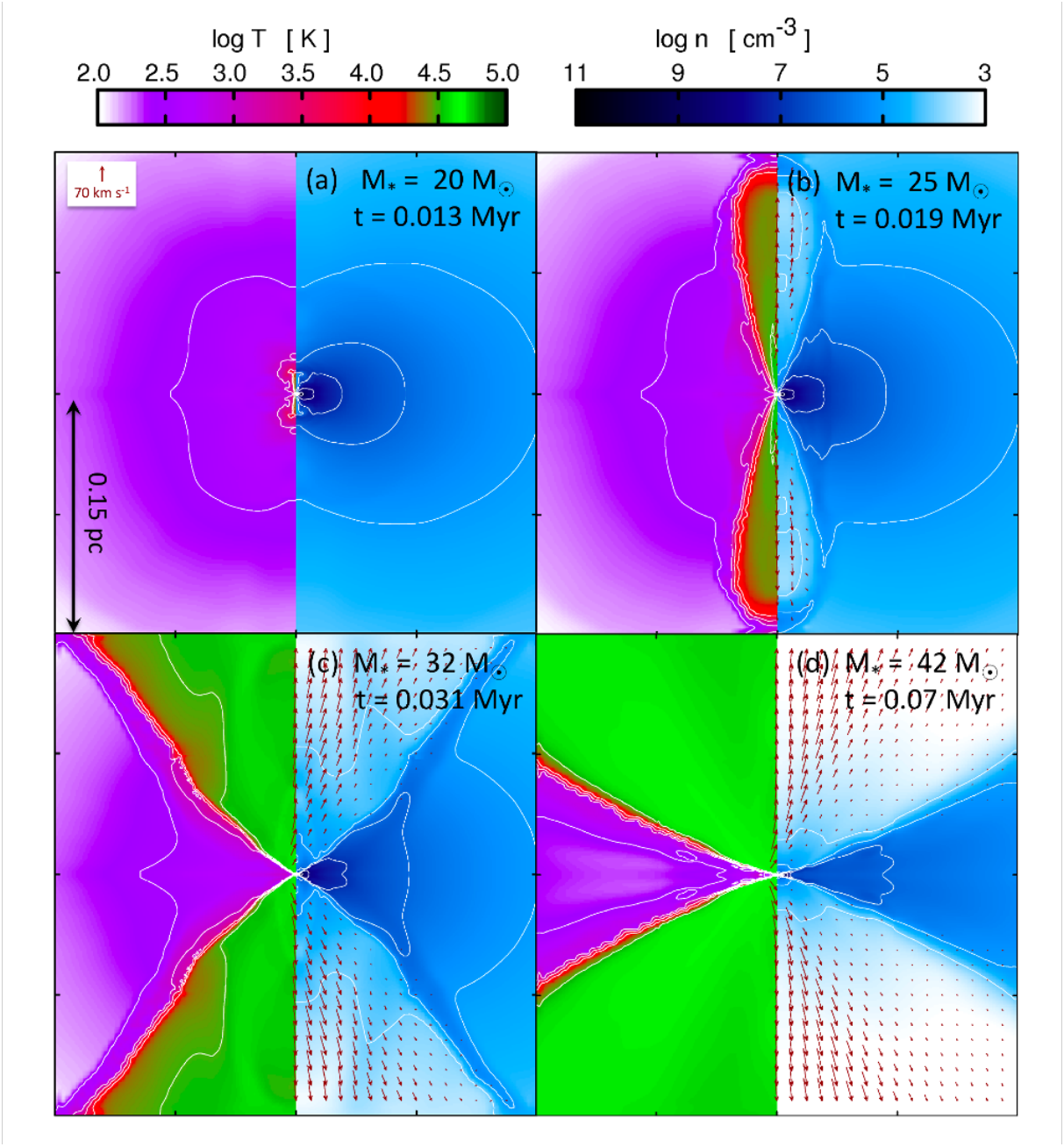

Figure 2.7: Simulation by Hosokawa et al. (2011) that follows the primordial star formation including its radiative feedback. Each panel shows the spatial distributions of gas temperature (left), number density (right), and velocity (right, arrows). The four panels correspond to the epoch when the stellar mass is 20 $M_\odot$ (a), 25 $M_\odot$ (b), 35 $M_\odot$ (c), and 42 $M_\odot$ (d). The protostellar ionizing photons create the HII region in the polar direction, and it gradually expands due to the high pressure.

However, the luminosity increases as the stellar mass increases, and $t_{\rm KH}$ gradually decreases. Once $t_{\rm KH}$ becomes shorter than $t_{\rm acc}$, the radiative energy loss becomes efficient, leading to substantial changes in the stellar evolution.

Here, following Hosokawa & Omukai (2009b), we first overview the stellar evolution with the constant accretion rates of 10^{-3} $M_\odot {\rm yr}^{-1}$ in solar metallicity case shown in Figure 2.8. The basic evolutionary features are similar even in the metal-free case, and we

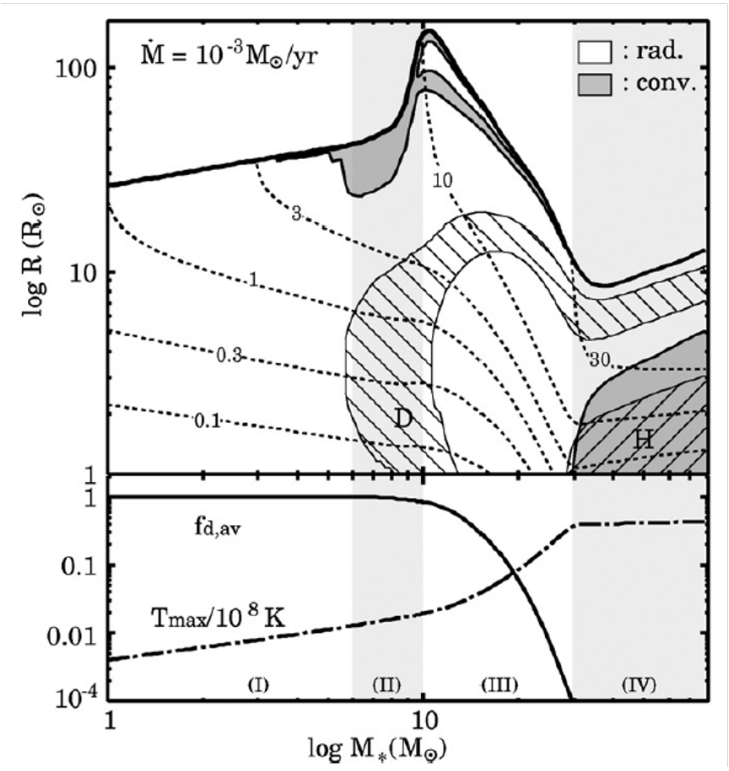

Figure 2.8: Protostellar Evolution with the accretion rates of 10^{-3} $M_{\odot}\mathrm{yr}^{-1}$ and solar metallicity. *Upper panel* : The thick solid line represents the protostellar radius corresponding to the shock front. The gray region indicates the convective region, while the uncolored area denotes the radiative zone. The hatched areas show the region where deuterium or hydrogen burning occurs. The dotted lines represent mass coordinates. *Lower panel* : The solid line shows the evolution of the mass-averaged deuterium concentration. The dot-dashed line indicates the maximum temperature inside the protostar. The background shading represents the four evolutionary phases : (I) adiabatic accretion, (II) swelling, (III) Kelvin-Helmholtz contraction, and (IV) main-sequence accretion phases. This figure is taken from Hosokawa & Omukai (2009b)

mention the minor differences later. We can divide the stellar evolution into four phases as labeled in Figure 2.8: (I) the adiabatic accretion, (II) swelling, (III) KH contraction, (IV) main-sequence accretion phases. In the following, we discuss each phase.

In the adiabatic accretion phase, $t_{\rm acc} < t_{\rm KH}$ and the accreting gas keep its entropy without radiative energy loss. We can roughly understand the evolution in this phase from the following estimates. The typical density and pressure of protostar with the mass M_* and radius R_* can be expressed as

$$\rho \sim \frac{M_*}{R_*^3}, \qquad P \sim G\frac{M_*^2}{R_*^4}. \tag{2.81}$$

The specific entropy of an ideal monoatomic gas can be written as

$$s = \frac{3\mathcal{R}}{2\mu}\ln\left(\frac{P}{\rho^{5/3}}\right) + \text{const}, \tag{2.82}$$

where $\mathcal{R}$ is the gas constant. From these equations, the dependence of stellar radius on

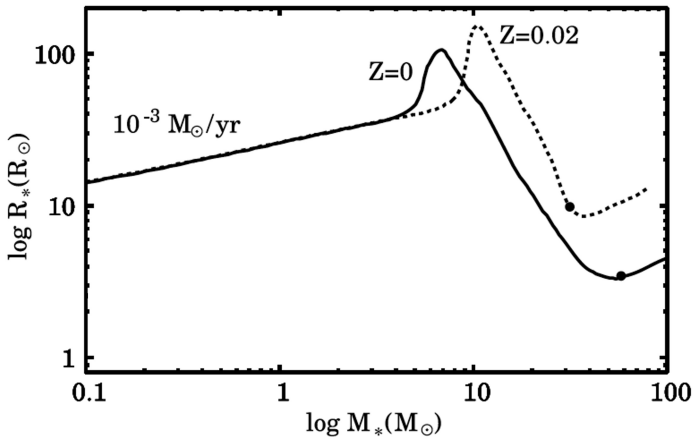

Figure 2.9: Protostellar mass-radius relations for the accretion rates of $10^{-3}\ M_{\odot}\mathrm{yr}^{-1}$. The solid and dotted lines indicate the metal-free and solar metallicity cases. The filled circles denote the epoch when the energy production rate by the hydrogen burning accounts for 80 % of the interior luminosity. This figure is based on Hosokawa et al. (2012a)

its mass and specific entropy follows

$$R_* \propto M_*^{-1/3} \exp\left(\frac{2\mu}{3\mathcal{R}} s\right). \tag{2.83}$$

This equation means that the specific entropy of the accreting gas must increase for the continuous protostellar expansion. Actually, R_* is proportional to $M_*^{0.27}$ from Figure 2.8, and the thermal energy released at the shock front ($\sim GM_*/R_*$) rises with the increasing mass, which leads to larger specific entropy. The mass dependence of the radius itself can be understood with the very steep temperature dependence of H^- bound-free absorption (Stahler et al., 1986). Note that the internal temperature,

$$T \sim \frac{\mu m_{\mathrm{H}}}{k_{\mathrm{B}}} \frac{P}{\rho} \sim \frac{\mu m_{\mathrm{H}} G}{k_{\mathrm{B}}} \frac{M_*}{R_*}, \tag{2.84}$$

also rises with the increasing mass, as seen in the lower panel in Figure 2.8.

As the internal temperature increases, the opacity decreases following the Kramers' law. This leads to efficient radiative transfer inside protostars. Meanwhile, the opacity is larger due to the lower temperature near the stellar surface. As a result, a small amount of gas in the outer layers receives the entropy, and the protostar expands, which corresponds to (II) the swelling phase in Figure 2.8. We note that deuterium burning during this phase has little impact on the stellar structure. This is in contrast to the case with lower accretion rates. When the accretion rate is $10^{-5}\ M_{\odot}\mathrm{yr}^{-1}$, the protostar expands owing to deuterium shell burning (Palla & Stahler, 1990). In the case with high accretion rates, the density is lower due to the large entropy, and the opacity is smaller. Hence, the radiative energy transport is effective enough to transfer the energy originating from the deuterium burning.

At the end of the swelling phase, the interior luminosity overwhelms the accretion luminosity due to the increasing internal temperature. The ratio $t_{\mathrm{KH}}/t_{\mathrm{acc}}$ is equivalent to L_{acc}/L_*, Thus, the protostar radiates away its internal energy efficiently via radiation,

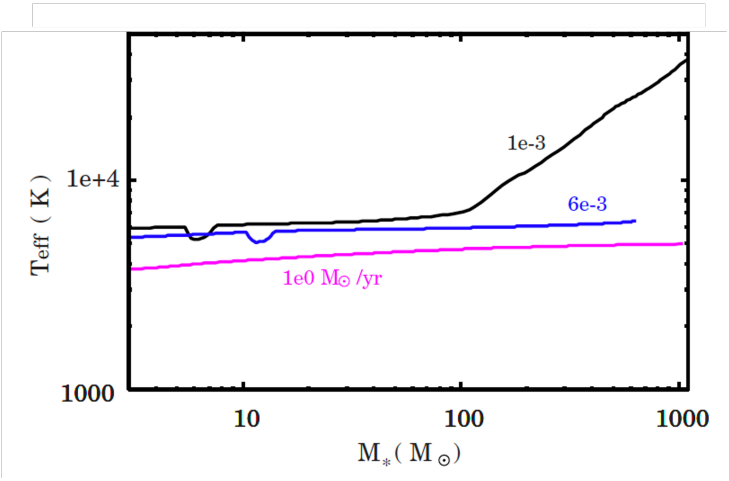

Figure 2.10: The stellar effective temperature in metal-free case. The black, blue, and magenta lines represent cases with $\dot{M} = 10^{-3}\ M_{\odot}\mathrm{yr}^{-1}, 6$, respectively. This figure is taken from Hosokawa & Omukai (2009b)

leading to the stellar contraction. This period is (III) the KH contraction phase. During this phase, the internal temperature increases from the virial equilibrium. The contraction ceases when hydrogen nuclear burning, which compensates for the radiative energy loss, begins at $M_* \simeq 30 M_{\odot}$. After that, the protostar evolves obeying the mass-radius relation of main-sequence stars, which corresponds to the (IV) main-sequence accretion phase.

In the following, we examine how the above stellar evolution changes in the metal-free case. Figure 2.9 shows the evolution for solar metallicity and metal-free cases with an accretion rate of $10^{-3}\ M_{\odot}\mathrm{yr}^{-1}$. In the metal-free case, the protostar follows similar evolution as the solar metallicity case and experiences the four evolutionary phases. However, there are two differences, as explained below. First, the swelling phase occurs earlier in the metal-free case. This phase begins when the decrease in the opacity makes the radiative energy transport effective. In the metal-free case, the opacity is lower due to the lack of metals, leading to the earlier onset of the swelling phase. Secondly, the radius at which the KH contraction stops is smaller for the metal-free case. This is because, in the absence of carbon (C) and nitrogen (N), sufficient energy supply through the CN cycle does not occur even when the central temperature rises to a similar value to that of the solar metallicity case ($\sim 10^7$ K). In the metal-free case, the contraction ceases when the internal temperature reaches 10^8 K, and a small amount of carbon produced through He burning enables a sufficient CN cycle.

Figure 2.10 shows the evolution of the stellar effective temperature at the photosphere for various accretion rates in metal-free case. The black line corresponds to the accretion rate of $10^{-3}\ M_{\odot}\mathrm{yr}^{-1}$. After the Kelvin-Helmholtz contraction, the effective temperaturea increases with the increasing mass following the evolution of main-sequence stars. Consequently, protostars emit more and more EUV photons, which eventually lead to the formation of the HII region around them. Such an HII region expands due to its gas pressure and ultimately halts gas accretion onto the primordial star by blowing away the surrounding gas.

2.3 Direct Collapse Scenario

In the early universe, there is another pathway for primordial star formation than the one described in Section 2.2. It is called the DC scenario (Bromm & Loeb, 2003). In this section, we briefly overview the motivation and physical processes of this scenario.

2.3.1 Supermasive Black Holes at High-Redshift Universe

DC scenario is mainly motivated by the discovery of SMBHs in the early universe. Figure 2.11 shows masses and redshifts of SMBH observed at high-redshift ($z > 6$). As we can see, many SMBHs exceed $10^9\ M_\odot$ until $z \sim 6$. Although the very efficient accretion is necessary to form such SMBHs from the ordinally stellar mass BHs ($M_{\rm BH} \sim 10{-}10^3\ M_\odot$), the radiative feedback regulates the maximum accretion rate to the Eddington accretion rate

$$\dot{M}_{\rm Edd} \equiv \frac{4\pi c G M_{\rm BH}}{\epsilon c^2 \kappa_{\rm es}}, \tag{2.85}$$

where $M_{\rm BH}$ is the black hole mass, $\kappa_{\rm es}$ is the electron scattering opacity and ϵ is the radiative efficiency. This accretion rate originates from the balance between the radiation pressure and gravity exerted on the accreting gas. The solid lines in the Figure 2.11 indicate the evolutionary path of BHs growing at the Eddington accretion rates. They show that we can explain the existence of the observed SMBHs if the Eddington accretion continue for $\sim 10^9$ yr since $z = 35$. However, considering the feedback from the BH onto the accretion and primordial stars onto the gas reservoir, Eddington accretion unlikely continues for such a long period.

One proposed solution to this challenge is allwoing BHs to grow at accretion rates that exceed the Eddington one. When the accretion rates are sufficiently high, photons are trapped and advected inward with the accreting gas, which results in the reduction of radiation (Begelman, 1978). Indeed, multi-dimensional simulations have demonstrated that the accretion rates exceeding the Eddington limit can be realized in the vicinity of black holes (e.g. Ohsuga et al., 2005; Jiang et al., 2014). Furthermore, Inayoshi et al. (2016) investigate the structure of accreting gas including larger scales, and show that accretion rates hundreds of times higher than the Eddington rate can be achieved in certain conditions.

Another solution is the so-called the DC scenario. In this scenario, we need to prepare heavy BH seeds at first. As reviewed in the following section, primordial stars can grow into SMSs with masses of $M_* \sim 10^5$–$10^6\ M_\odot$ under some special environments. SMSs exceeding a ciritical mass can directly collapse into BHs due to GR instability (Chandrasekhar, 1964; Zeldovich & Novikov, 1971; Shapiro & Teukolsky, 1983). Theoretical studies imply that the critical stellar mass for GR instability is $\sim 10^5$–$10^6\ M_\odot$ depending on the deteailed SMS structure. This GR instability leads to the formation of BHs with almost the same masses of SMSs (Shibata & Shapiro, 2002). Such remnant BH seeds can grow into the ovserved high-redshift SMBHs even with the sub-Eddington accretion rates. In this thesis, we focus on this scenario and review the formation processes of SMSs in the following sections.

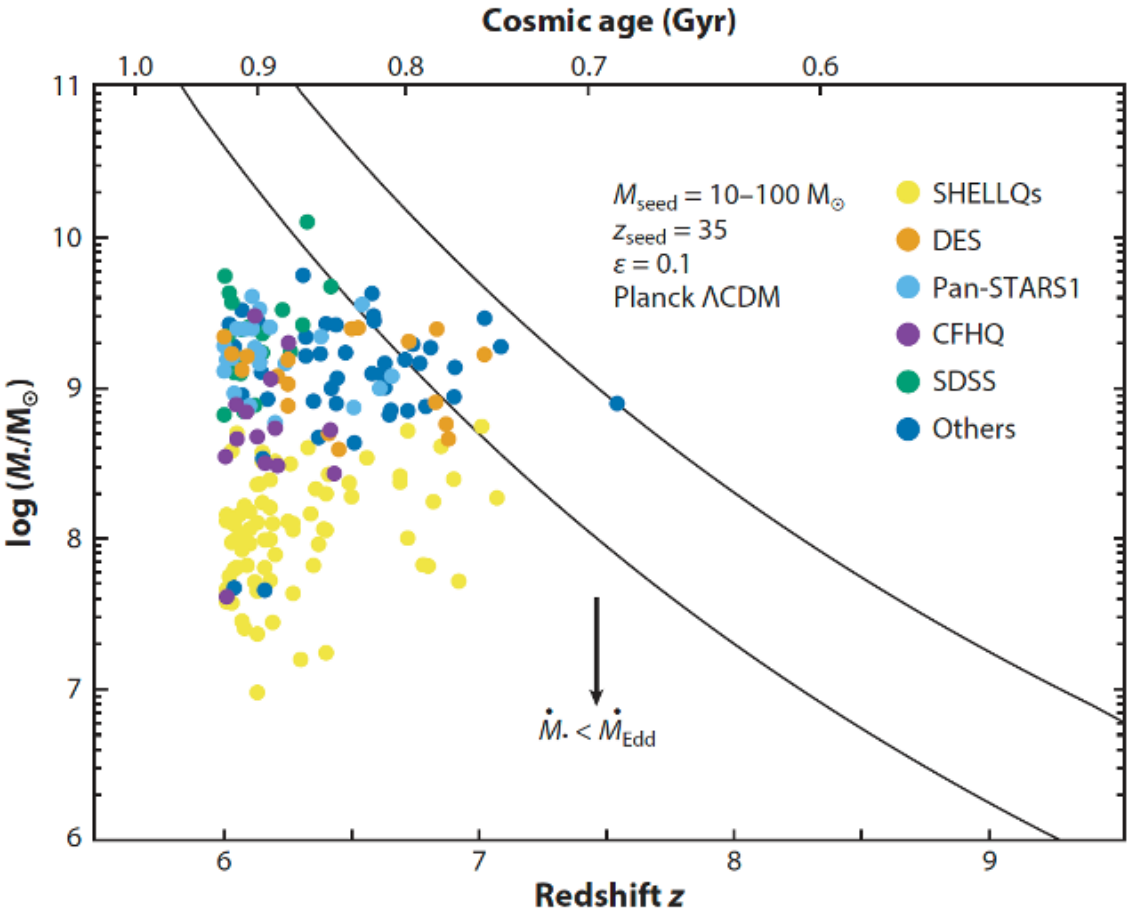

Figure 2.11: Masses and redshifts of the SMBH observed at $z > 6$. The colors denotes what kind of survey discover the SMBH. The solid lines show the evolutionary path of BH mass growing at the Eddington accretion rate with a radiative efficiency of $\epsilon = 0.1$ and comological parameter given by Planck Collaboration et al. (2020). The lower and upper lines starts from the initial masses of 10 $M_\odot$ and 100 $M_\odot$ at $z = 35$, respectively. This figure is taken from Inayoshi et al. (2020)

2.3.2 Supermassive Star Formation in Atomic Cooling Halo

As seen in Section 2.2, H_2 cooling triggers gravitational collapse in the early universe, and primordial stars form from clouds with masses of $\sim 10^3$ $M_\odot$ as a result of core fragmentation. Moreover, protostellar radiative feedback halts the gas accretion. For SMS formation, we need more massive star-forming clouds with masses of at least 10^5 $M_\odot$ by avoiding the small scale fragmentation and larger accretion rates that bloat protostars and weaken EUV feedback. Such situations can be realized in the DM halo where not H_2 but H atomic cooling is efficient. Although there are several mechanisms suppressing H_2 cooling as seen in Section 2.3.3, we discuss the atomic cooling collapse triggered by the far-ultraviolet (FUV) radiation from nearby galaxies in this section.

Figure 2.12 shows the thermal evolution of the primordial collapsing clouds with various intensities of the background Leyman-Werner (LW, 11.2 eV $< h\nu <$ 13.6 eV) radiation. If there is enough LW radiation, it dissolves H_2 molecules and make their cooling

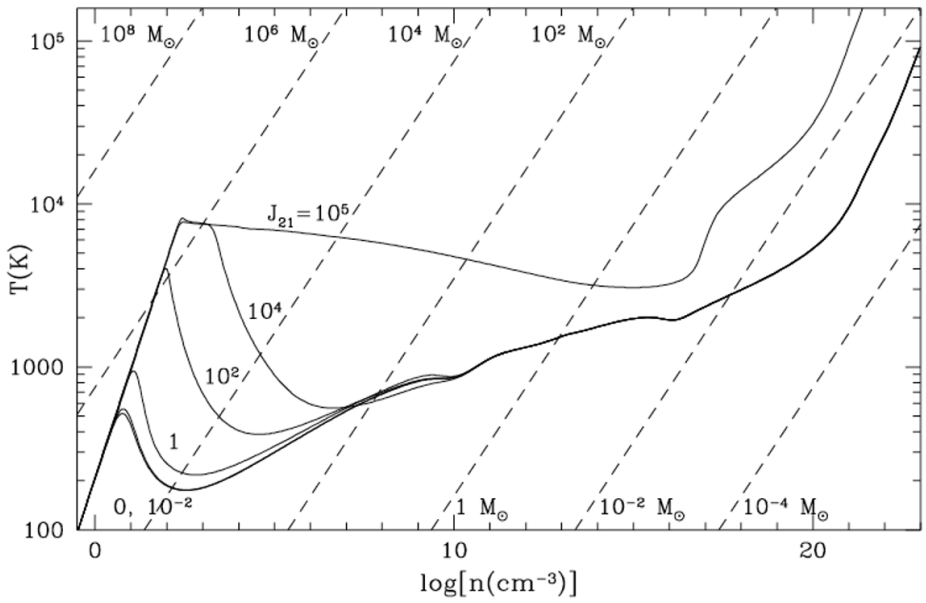

Figure 2.12: The thermal evolution of the primordial collapsing clouds for various FUV intensity. The horizontal and vertical axis is the number density and temperature. The diagonal dashed line represents the constant Jeans mass. J_{21} is FUV intensity normalized at LW band (unit in 10^{-21} erg/s/Hz/cm^2/str). This figure is taken from Omukai (2001)

inefficient When $J_{21} \leq 10^4$, H_2 molecules form during the collapse and their cooling returns the evolutionary path to the case with no FUV radiation. Meanwhile, when $J_{21} = 10^5$ $M_\odot$, the cloud collapses with H atomic cooling. The cloud avoids a rapid temperature decrease and contracts almost isothermally. Although the central region of the core is unstable to non-spherical perturbations during collapse even in this case, it does not lead to vigorous fragmentation unlike the H_2 cooling case (Inayoshi et al., 2014; Sugimura et al., 2017). Moreover, we can estimate the cloud mass in the atomic cooling case. The atomic cooling becomes efficient when the temperature reaches $\sim 10^4$ K. The corresponding virial mass for this temperature is approximately $\sim 10^7$–10^8 $M_\odot$ at $z = 10$–20 from Equation (2.44). Therefore, the atomic cooling collapse occurs in clouds with masses of $\Omega_\mathrm{b} \times M_\mathrm{DM} \sim 10^5$–$10^6$ $M_\odot$. This mass reservoir is enough for SMS formation. Moreover, with Equation (2.73), the accretion rate onto the protostar can be roughly estimated as follows:

$$\dot{M} \sim 10^{-1}\ M_\odot \mathrm{yr}^{-1} \left(\frac{T}{8000\ \mathrm{K}}\right)^{3/2}. \tag{2.86}$$

If this very high accretion rate continues for 10^6 yr without the radiative feedback, SMSs with masses of 10^5 $M_\odot$ can be formed. Of course, whether SMSs can actually be formed depends on the evolution of circumstellar disks and protostellar structure.

Multi-dimensional simulations have confirmed the disk formation and its fragmentation even in the SMS formation (Becerra et al., 2015; Chon et al., 2018). Especially, as the accretion rates are high in the atomic cooling halos, the disks rapidly become massive, leading to gravitational instability. Latif et al. (2020) demonstrate that the binary and small multiples of SMSs can form due to the disk fragmentation. If massive remnant BHs merge with others, there is the possibility of detecting its gravitational waves with the Laser Interferometer Space Antenna. Moreover, the inward migration of fragments

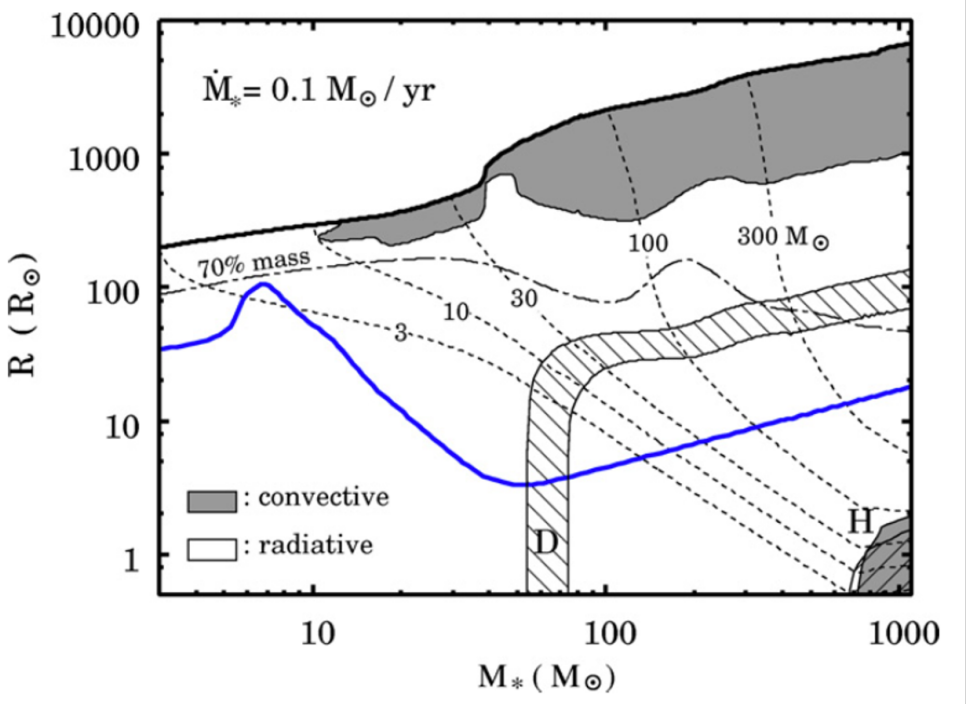

Figure 2.13: Same as the upper panel of Figure 2.8 but for the case with the accretion rates of 0.1 $M_\odot \mathrm{yr}^{-1}$ and $Z = 0$. The dotted lines denote the radius corresponding to the mass coordinates of 3, 10, 30, 100, and 300 $M_\odot$. The dot-solid line shows the radius within which 70 % of the stellar mass is enclosed. The solid blue line indicates the stellar evolution for the case with the accretion rates of 10^{-3} $M_\odot \mathrm{yr}^{-1}$ and $Z = 0$ shown in Figure 2.9. This figure is taken from Hosokawa et al. (2012a)

induces episodic burst-like accretion onto the central protostars. However, the variable timescale of the accretion rates is too short to affect the stellar structure (Sakurai et al., 2016).

We show the protostellar evolution under the accretion rate of 0.1 $M_\odot \mathrm{yr}^{-1}$ in Figure 2.13. The solid black line indicates the protostellar radius. Unlike the normal primordial stars, protostars grow in mass keeping their large radius. Note that the internal part loses its internal energy via the radiative energy transport and contracts, as shown by the dashed lines in the figure. Meanwhile, the outer layer accepts that energy flux and swells up. The protostellar effective temperature remains several thousand Kelvin due to the steep temperature dependence of H^- bound-free absorption, like the blue and magenta lines in Figure 2.10. As a result, protostars emit few EUV photons, which enables the formation of SMSs and their remnant massive BH seeds without the radiative feedback (Umeda et al., 2016; Haemmerlé et al., 2018a).

2.3.3 Mechanisms Supressing Hydrogen Molecular Cooling

As seen in Section 2.3.2, SMSs can form if H_2 cooling is ineffective. Several mechanisms which suppress its cooling have been proposed so far. One major mechanism is the FUV radiation from primordial stars in nearby galaxies. Previous studies indicate that primordial stellar masses are typically 10–10^3 $M_\odot$ (Hirano et al., 2014). Such massive stars have an effective temperature of $\sim 10^5$ K and emit a large amount of ultraviolet

photons. Particularly, EUV photons ionize atomic hydrogen and create an HII region around stars, and FUV photons at the Lyman-Werner band ($11.2 < h\nu < 13.6$ eV) dissociate the hydrogen molecules. The size of the HII region is restricted by the balance of the EUV emissivity and the recombination rate of hydrogen. Meanwhile, hydrogen atoms do not absorb FUV photons, and FUV propagates further than EUV. As a result, the photodissociated region of H_2 molecules is larger than the HII region.

In the region with strong FUV background, the hydrogen molecules deplete through two types of reactions. One is the dissociation by FUV photons (Stecher & Williams, 1967). These photons are absorbed efficiently by H_2 and excite the electron states. About 10 % of H_2 in the exited states decays radiatively into two H atoms. Another is the destruction of H^- by photons with the energy of photodissociation ($h\nu > 0.76$ eV). This prohibits H_2 formation through H^- process reviewed in Section 2.2.1. Basically, the former process plays a major role while the latter reduces the critical FUV intensity necessary for atomic cooling halo $J_{\rm crit}$ by several tens percent (Wolcott-Green et al., 2017, 2021).

The exact value of $J_{\rm crit}$ remains subject to debate. When the gas density is high enough as in atomic cooling halo, the self-shielding of H_2 molecules becomes effective. H_2 molecules have many rovibrational states, making it challenging to calculate the H_2-photodissociation rate in such an optically thick region. Additionally, the intensity and shape of FUV radiation spectra depend on the properties of nearby galaxies, such as the distance from the atomic cooling halo and the star formation history within those galaxies, which increases uncertainty in the estimation of $J_{\rm crit}$. Eventually, previous studies indicate that $J_{\rm crit}$ range $\sim 10^3$–10^5 J_{21} with halo-to-halo variation.

Other than the FUV background, various processes trigger the DC scenario. For example, the relative velocities of baryon and DM, the so-called streaming velocity, is one candidate. Before the cosmological recombination at $z \sim 1100$, baryon gas couples to the photons, and DM and baryon move separately. As a result, the relative motion coherent on Mpc scale and with a typical magnitude of 30 km/s $[(1 + z)/100]$ can be produced. This streaming velocity delay the collapse of baryon gas into the DM halo potential, and the halo becomes more massive until the onset of the star formation (Greif et al., 2011). In this case, although the H_2 molecules form via three-body reactions and become efficient coolants, the entire cloud contracts rapidly with the mass accretion rate of ~ 1 $M_\odot$/yr (Hirano et al., 2017). Dynamical heating by galaxy merger also interrupts the H_2 cooling. Especially, unusually frequent mergers, which induce the continuous shock-heating on a shorter time-scale than the H_2 cooling time, can inhibit the original primordial star formation (Fernandez et al., 2014). Moreover, some simulations show that the combination of galaxy merger and LW radiation with $J_{21} \ll J_{\rm crit}$ increases the gas temperature on ~ 10 pc scale and forms massive clouds with high accretion rates necessary for SMS formation (Wise et al., 2019).

Chapter 3

Growth of Massive Disk and Early Disk Fragmentation

As reviewed in Section 2, previous multi-dimensional simulations demonstrate that disk formation and its fragmentation ubiquitously occur in primordial star formation. Many authors have surveyed the stability of the circumstellar disks around primordial stars using 1D models (Inayoshi & Haiman, 2014; Latif & Schleicher, 2015; Matsukoba et al., 2019). Although 1D models are computationally less expensive, previous models have some limitations. They cannot follow the mass evolution of the disk and star, which is an indicator of the gravitational instability (Kratter et al., 2010). Moreover, the comparison between 1D models and 3D simulations has also been limited. For instance, previous 3D simulations show that the disk generally fragments in an early accretion stage in both the normal primordial star formation and the DC scenario. No previous 1D models reveal why the gravitational instability causes the disk fragmentation so early.

In this chapter, we develop a 1D non-steady semi-analytical model to investigate the growth of accretion disks around primordial protostars. While our formulation is based on the framework established by Takahashi et al. (2013), this model includes effective cooling processes and chemical reactions associated with the pristine gas. We especially focus on the early stage of the accretion phase before protostellar masses reach 10 $M_\odot$ and investigate how the disk evolves under the rapid mass supply from the surrounding envelope. To verify our model, we perform a high-resolution 3D simulation with an adaptive mesh refinement (AMR) code (Sugimura et al., 2020). We compare the evolution in our 1D model and 3D simulation, both of which start from the same initial condition.

The remainder of this chapter is organized as follows. In Section 3.1, we provide a detailed description of our non-steady model. In Section 3.2, we show the disk evolution in our model with varying model parameters. Section 3.3 is devoted to the comparison between our model and 3D simulation. We discuss the implications of our findings in Section 3.4. Finally, we give summary and conclusion in Section 3.5. Note that this chapter is based on the author's paper Kimura et al. (2021).

3.1 Model

In this section, we present our 1D non-steady disk model for primordial star formation. The mass supply onto the disk is modeled in Section 3.1.1. We describe the governing equations of the disk in Section 3.1.2. In Section 3.1.3, we describe the numerical method to solve the equations and the model parameters for which we calculate.

3.1.1 Mass Supply from Envelope onto Disk

We follow the method of Takahashi et al. (2013) to model the mass supply onto the disk, with some modifications. They set the Bonnor-Ebert sphere as the initial condition and solve the equation of motion approximately to estimate when and where gas infalls onto the disk. While their method provides a reasonable approximation for the mass supply onto the disk during the late accretion stage, we find its substantial underestimation of the rate for ~ 100 yr after the protostellar birth. Instead, we set an envelope structure consistent with the early run-away collapse, which occurs in a self-similar fashion (Omukai & Nishi, 1998).

Taking into account the equation of state $\mathrm{P} = \mathrm{K}\rho^{\gamma}$, the envelope structure at the birth of the protostar can be described as

$$\rho = C_1 K^{1/(2-\gamma)} r^{-2/(2-\gamma)} , \tag{3.1}$$

$$v = C_2 K^{1/2(2-\gamma)} r^{(1-\gamma)/(2-\gamma)} , \tag{3.2}$$

where r is the radial distance, ρ is the gas mass density, v is the radial velocity, γ is the effective polytropic index, and C_1 and C_2 are constants (Larson, 1969; Penston, 1969). We determine the values of K, γ, C_1, and C_2 so that the resulting envelope structure agrees with the outcome of a 1D hydrodynamic calculation by Omukai & Nishi (1998), who follow the gravitational collapse of a primordial cloud. During the collapse, the gas temperature gradually increases due to the compressional heating counterbalanced by H_2 molecular cooling. The resulting thermal evolution can be described as

$$T \simeq 200 \left(\frac{n_{\mathrm{H}}}{10^4 \mathrm{cm}^3}\right)^{0.1} \ \mathrm{K} , \tag{3.3}$$

where n_{H} is the number density of hydrogen nuclei, which is related to the mass density ρ as

$$n_{\mathrm{H}} = \frac{\rho}{(1 + 4y_{\mathrm{He}})m_{\mathrm{H}}}, \tag{3.4}$$

where $y_{\mathrm{He}} = 8.333 \times 10^{-2}$ is the number fraction of He relative to hydrogen nuclei, and m_{H} is the mass of hydrogen nucleus. Equation (3.3) indicates that γ is 1.1 ($T \propto \rho^{\gamma-1}$). The parameter values that closely match the numerical result are $K = 4.2 \times 10^{11}$ (hereinafter denoted as K_{fid}), $C_1 = 6.1 \times 10^7$, $C_2 = -7.0$ (in cgs), and $\gamma = 1.1$. In this fiducial case, we can rewrite Equations (3.1) and (3.2) as

$$\rho = 2.6 \times 10^{-9} \left(\frac{K}{K_{\mathrm{fid}}}\right)^{10/9} \left(\frac{r}{1\mathrm{AU}}\right)^{-20/9} \ \mathrm{g/cm}^3, \tag{3.5}$$

$$v = -6.9 \times 10^5 \left(\frac{K}{K_{\mathrm{fid}}}\right)^{5/9} \left(\frac{r}{1\mathrm{AU}}\right)^{-1/9} \ \mathrm{cm/s}. \tag{3.6}$$

To investigate the variation of the disk evolution for different mass supply rates from the envelope, we also consider the cases where $K = 0.1K_{\mathrm{fid}}$ and $K = 10K_{\mathrm{fid}}$ (see Section 3.2.2).

Assuming a weak rotation of the cloud, we approximate the elapsed time t until the gas on a spherical shell with the original radius r reaches the disk as

$$t \simeq \frac{r}{v(r)}. \tag{3.7}$$

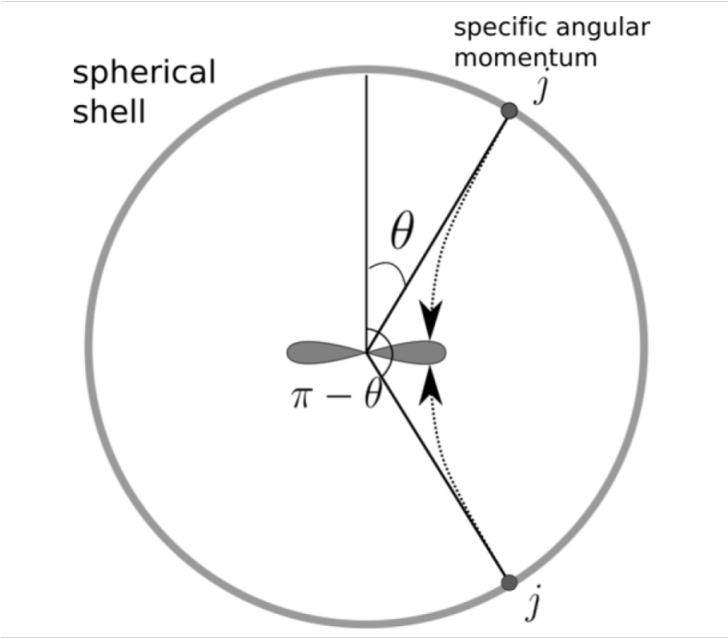

Figure 3.1: Schematic picture of the gas infall from the envelope onto the disk. The gases with an initial angle θ and $\pi - \theta$ have the same specific angular momentum. Thus, these gases infall onto the same part of the disk determined by the centrifugal balance. This figure is taken from Takahashi et al. (2013).

With the relation $r = r(t)$ obtained from Equation (3.7), the total mass supply rate from the envelope to the disk can be expressed by

$$\dot{M}_{\rm e,tot}(t) = 4\pi\rho(r)r^2\frac{dr}{dt}. \tag{3.8}$$

We assume that the initial rotational velocity of the envelope is $f_{\rm Kep}$ times the Kepler values everywhere:

$$\Omega_0 = f_{\rm Kep}\Omega_{\rm Kep} = f_{\rm Kep}\sqrt{\frac{GM_r}{r^3}}, \tag{3.9}$$

where Ω_0 is the angular velocity and M_r is the enclosed mass of the envelope within the radius r. According to previous 3D simulations starting from cosmological initial conditions (e.g., Abel et al., 2002; Yoshida et al., 2006), $f_{\rm Kep}$ typically takes the value of $\simeq 0.5$. To examine how the disk structure depends on the envelope rotation, we consider the cases where $f_{\rm Kep} = 0.3,\ 0.5$, and 0.8 (see Section 3.2.3).

Depending on the angular momentum j of the infalling gas, the mass supply at the total rate $\dot{M}_{\rm e,tot}(t)$ is distributed into different parts of the disk, as shown in Figure 3.1. The angular momentum j changes with the polar angle θ ($0 \leq \theta \leq \pi/2$) of the original position as follows:

$$j \ = \ r^2 \sin^2\theta\ \Omega_0. \tag{3.10}$$

We assume the angular momentum conservation during the gas infall onto the disk. We consider the mass supply rate only inside a given radius ϖ of the disk, $\dot{M}_{\rm e}(\varpi, t)$. We can

obtain the local rate at the radius ϖ by the ϖ-derivative of $\dot{M}_{\rm e}(\varpi, t)$ as

$$\begin{aligned}\frac{\partial \dot{M}_{\rm e}(\varpi,t)}{\partial \varpi} &= \frac{\partial j}{\partial \varpi}\frac{\partial \dot{M}_{\rm e}(j,t)}{\partial j} \\ &= 2\frac{\partial j}{\partial \varpi}\frac{\partial \theta}{\partial j}\frac{\partial \dot{M}_{\rm e}(\theta,t)}{\partial \theta} \\ &= \frac{\dot{M}_{\rm e,tot}}{2\Omega_0 r^2}\left(1-\frac{j}{\Omega_0 r^2}\right)^{-1/2}\frac{\partial j}{\partial \varpi}, \end{aligned} \tag{3.11}$$

where we have substituted the relation

$$\frac{\partial \dot{M}_{\rm e}(\theta,t)}{\partial \theta} = \frac{\sin\theta}{2}\dot{M}_{\rm e,tot}. \tag{3.12}$$

3.1.2 Disk Evolution

Next, we describe the equations governing the disk evolution. From here, we take a cylindrical coordinate system (ϖ, ϕ, z) and assume the axial symmetry. We also assume that the disk rotation is Keplerian one, i.e., the angular velocity Ω and specific angular momentum j are given by

$$\Omega = \sqrt{\frac{GM_\varpi}{\varpi^3}}, \tag{3.13}$$

$$j = \varpi^2\Omega = \sqrt{\varpi G M_\varpi}, \tag{3.14}$$

where $M_\varpi = M_* + \int_{\varpi_{\rm in}}^{\varpi} 2\pi\varpi\Sigma d\varpi$ is the enclosed mass of the disk within the radius ϖ, M_* is the protostellar mass, and $\varpi_{\rm in}$ is the inner boundary radius of the disk.

3.1.2.1 Mass and Angular Momentum Conservation

The mass and angular momentum conservation are described as follows:

$$\frac{\partial}{\partial t}(2\pi\varpi\Sigma) - \frac{\partial \dot{M}_{\rm d}}{\partial \varpi} = \frac{\partial \dot{M}_{\rm e}}{\partial \varpi}, \tag{3.15}$$

$$\frac{\partial}{\partial t}(2\pi\varpi\Sigma j) - \frac{\partial}{\partial \varpi}(\dot{M}_{\rm d} j) = \frac{\partial}{\partial \varpi}\left((2\pi\varpi\Sigma)\nu\varpi^2\frac{\partial \Omega}{\partial \varpi}\right) + \frac{\partial \dot{M}_{\rm e}}{\partial \varpi} j, \tag{3.16}$$

where $\dot{M}_{\rm d} \equiv -2\pi\varpi\Sigma v_\varpi$ is the accretion rate through the disk, Σ is the surface density, v_ϖ is the radial velocity, and ν is the viscosity coefficient. By subtracting the product of j and Equation (3.15) from Equation (3.16), we can get

$$2\pi\varpi\Sigma\frac{\partial j}{\partial t} - \dot{M}_{\rm d}\frac{\partial j}{\partial \varpi} = \frac{\partial}{\partial \varpi}\left((2\pi\varpi\Sigma)\nu\varpi^2\frac{\partial \Omega}{\partial \varpi}\right). \tag{3.17}$$

Here, from Equation (3.14), we can describe $\partial j/\partial t$ and $\partial j/\partial \varpi$ as

$$\frac{\partial j}{\partial t} = \frac{1}{2}\sqrt{\frac{\varpi G}{M_\varpi}}\frac{\partial M_\varpi}{\partial t} = \frac{1}{2}\sqrt{\frac{\varpi G}{M_\varpi}}\left(\dot{M}_{\rm d} + \dot{M}_{\rm e}\right), \tag{3.18}$$

$$\begin{aligned}\frac{\partial j}{\partial \varpi} &= \frac{1}{2}\sqrt{\frac{GM_\varpi}{\varpi}}\left(1 + \frac{\varpi}{M_\varpi}\frac{\partial M_\varpi}{\partial \varpi}\right) \\ &= \frac{1}{2}\sqrt{\frac{GM_\varpi}{\varpi}}\left(1 + \frac{2\pi\varpi^2\Sigma}{M_\varpi}\right). \end{aligned} \tag{3.19}$$

With the above Equations (3.17)–(3.19), we finally obtain

$$\dot{M}_{\rm d} = -2\sqrt{\frac{\varpi}{GM_\varpi}}\frac{\partial}{\partial\varpi}\left\{(2\pi\varpi\Sigma)\nu\varpi^2\frac{\partial\Omega}{\partial\varpi}\right\} + 2\pi\Sigma\frac{\varpi^2}{M_\varpi}\dot{M}_{\rm e}. \tag{3.20}$$

In Equation (3.20), the first term on the right-hand side corresponds to the mass flux due to the viscosity. Meanwhile, the second term denotes the accretion induced by the mass supply from the envelope. Recall that, at a given radius ϖ, the enclosed disk mass M_ϖ increases at the supply rate $\dot{M}_{\rm e}$. As the centrifugal force with the fixed specific angular momentum no longer balances with the enhanced gravity, the gas can move inward without viscosity.

As for the viscosity coefficient ν, we employ the α prescription, wherein the gravitational torque is expressed as a function of Toomre Q (Shakura & Sunyaev, 1973):

$$\nu = \alpha c_s H = \alpha\frac{c_s^2}{\Omega}, \tag{3.21}$$

$$\alpha = A\exp(-BQ^4), \tag{3.22}$$

$$Q = \frac{c_s\Omega}{\pi G\Sigma}, \tag{3.23}$$

$$c_s = \sqrt{\frac{\gamma k_B T}{\mu m_{\rm H}}}, \tag{3.24}$$

where $H \equiv c_s/\Omega$ is the disk scale height, T is the midplane temperature, k_B is the Boltzmann constant, μ is the mean molecular weight, and A and B are arbitrary non-dimensional constants. The functional form of Equation (3.22) implies that the gravitational torque is effective only when $Q \lesssim 1.4$ (e.g., Boley et al., 2006), and this formulation has been often used in previous works (e.g., Zhu et al., 2010; Takahashi et al., 2013). Throughout this paper, we set $(A, B) = (1, 1)$. We have confirmed that the disk evolution is almost the same even if we change the values of A and B within the range of 0.1–10.

3.1.2.2 Vertical Structure

In the vertical direction z, we assume the hydrostatic equilibrium,

$$\frac{\partial p}{\partial z} \simeq -\rho\frac{\partial\Phi_g}{\partial z} \simeq -\rho\frac{GM_\varpi}{\varpi^2}\frac{z}{\varpi}, \tag{3.25}$$

where Φ_g is the gravitational potential, and we also assume that the disk is geometrically thin, $z \ll \varpi$. With the isothermal equation of state $p = c_s\rho$, the density and pressure stratification can be approximately described as

$$\rho(\varpi, z) = \rho_0\exp\left(-\frac{z^2}{2H^2}\right), \tag{3.26}$$

$$p(\varpi, z) = p_0\exp\left(-\frac{z^2}{2H^2}\right), \tag{3.27}$$

where the subscript 0 indicates the values at the disk midplane. By integrating Equation (3.26) in the z direction, we obtain

$$\rho_0 = \frac{\Sigma}{H\sqrt{2\pi}} = \frac{\Sigma\Omega}{c_s\sqrt{2\pi}}. \tag{3.28}$$

We use this equation to get the mass density at the disk midplane, ρ_0.

3.1.2.3 Energy Conservation

To calculate the temperature T, which is necessary for evaluating the viscosity ν (see Equations 3.21–3.24), we consider the energy conservation equation including the mass supply from the envelope, thermal processes, and chemical reactions of primordial gas:

$$\frac{\partial}{\partial t}(\Sigma e_{\rm th}) = \frac{1}{2\pi\varpi}\frac{\partial}{\partial\varpi}\left[\dot{M}_{\rm d}\left(\rho e_{\rm th}+\frac{p}{\rho}\right)\right]+\Sigma\nu\Omega^2\left(-\frac{3}{2}+\pi\Sigma\frac{\varpi^2}{M_\varpi}\right)^2 + \frac{1}{2\pi\varpi}\frac{\partial\dot{M}_{\rm e}}{\partial\varpi}e_{\rm th,e}-\Lambda_{\rm rad}-\Lambda_{\rm chem}, \tag{3.29}$$

where $e_{\rm th}$ is the specific thermal energy of the disk gas

$$e_{\rm th}=\frac{1}{\gamma_{\rm ad}-1}\frac{k_BT}{\mu m_{\rm H}}\,, \tag{3.30}$$

$e_{\rm th,e}$ is that of the infalling gas from the envelope, and $\gamma_{\rm ad}$ is the specific heat ratio. On the right-hand side, the first term corresponds to the advection, the second to the viscous heating, the third to the energy influx due to the mass supply, the fourth to the radiative cooling, and the fifth to the cooling by chemical reactions such as hydrogen ionization and dissociation. For simplicity, we estimate $e_{\rm th,e}$ assuming that the gas infalling onto the disk is fully molecular with the temperature of $T = 1000$ K, and we ignore the shock heating at the disk surface. We confirmed that the resultant disk structure is almost the same for various temperatures in the range of 500–5000 K. We evaluate the radiative cooling term $\Lambda_{\rm rad}$ separately for regions with $T < 10^4$ K and $T > 10^4$ K, as the disk vertical structure drastically changes across the boundary temperature $\sim 10^4$ K (e.g., Matsukoba et al., 2019): the optical depth integrated over the disk scale height is $\lesssim 1$ for $T < 10^4$ K and $\gg 1$ for $T > 10^4$ K. In the optically thin regime where $T < 10^4$ K, $\Lambda_{\rm rad}$ consists of the continuum cooling $\Lambda_{\rm cont}$ and the line cooling by H_2 molecules $\Lambda_{\rm H_2}$, which are evaluated with almost the same way by Matsukoba et al. (2019). For H_2 collisional induced cooling, we use the formula by Ripamonti & Abel (2004) for $T < 500$ K, since the formula by Matsukoba et al. (2019) is only valid for 500 K $< T <$ 20000 K. Meanwhile, for the optically thick regime where $T > 10^4$ K, we use the diffusion approximation of the thermal continuum emission (Hubeny, 1990):

$$\Lambda_{\rm rad}=\frac{2}{\Sigma}\sigma_{\rm SB}T_{\rm eff}^4=\frac{2}{\Sigma}\frac{8\sigma_{\rm SB}T^4}{3\tau_{\rm R}}\,, \tag{3.31}$$

where $\sigma_{\rm SB}$ is the Stefan–Boltzmann constant, $T_{\rm eff}$ is the effective temperature of the disk surface, and $\tau_{\rm R}$ is the optical depth evaluated with the Rosseland mean opacity $\kappa_{\rm R}$ as $\tau_{\rm R} = \kappa_{\rm R}\Sigma/2$. We use the opacity table presented by the Opacity Project (see Seaton et al. 1994).

3.1.2.4 Chemical Networks

Regarding chemical reactions, we consider the following 5 chemical species, H, H_2, H^+, H^-, e^-. We compute the abundances of these species with different methods depending on the number density of hydrogen nuclei $n_{\rm H}$. When $n_{\rm H} < 10^{16}$ cm^{-3}, we solve the non-equilibrium rate equations for H, H_2, H^+, e^-, assuming the equilibrium abundance only for H^- (Abel et al., 1997; Matsukoba et al., 2019). When $n_{\rm H} > 10^{16}$cm^{-3}, we solve the Saha

equations assuming that the chemical equilibrium is achieved. The chemical cooling rate is evaluated by

$$\Lambda_{\rm chem} = \left(\chi_{\rm H} \frac{dy({\rm H}^+)}{dt} - \chi_{\rm H_2} \frac{dy({\rm H_2})}{dt} \right) \frac{n_{\rm H}}{\rho} \,, \tag{3.32}$$

where $\chi_{\rm H} = 13.6$ eV is the ionization energy of hydrogen atom, $\chi_{\rm H_2} = 4.48$ eV is the dissociation energy of molecular hydrogen, and $y({\rm A}) \equiv n({\rm A})/n_{\rm H}$ is a number fraction of species A to hydrogen nuclei.

3.1.2.5 Difference from Previous Steady Models

Previous steady models neglect the terms including the time derivatives and the mass supply from the envelope in governing equations. As a result, the accretion rate, which is often assumed to be identical to the total mass supply rate from the envelope, is a constant throughout the disk. Furthermore, for calculating the steady disk structure, it is necessary to give the central stellar mass and disk accretion rate by hand. On the contrary, our non-steady model allows us to determine the accretion rate at each radius using Σ, T, and $\dot{M}_{\rm e}$ from Equation (3.20), which can differ from the mass supply rate. The mass growth history of the central star is determined by the accretion rate at the inner boundary, rather than the mass supply rate from the envelope.

3.1.3 Overall Procedures and Cases Considered

In summary, we solve Equations (3.15) and (3.29) with the finite volume method for calculating the time evolution of the surface density Σ and the midplane temperature T. In Equation (3.15), we evaluate $\partial \dot{M}_{\rm e}/\partial \varpi$ with Equation (3.11) and $\dot{M}_{\rm d}$ at the cell boundaries with Equation (3.20). Additionally, we simultaneously calculate chemical abundances. We set the computational domain from 0.1 AU to 10^5 AU, which is divided into 480 logarithmically equally-spaced cells, and assume that a disk forms in this domain. For boundary conditions, we impose the zero-flux condition at the outer boundary and the zero-torque condition at the inner boundary. The central protostar is assumed to immediately accrete the gas flowing in across the inner boundary. For initial conditions, we only set the protostar at the center without the disk. We set the initial stellar mass to be $10^{-2}\ M_\odot$ for models presented in Section 3.2, and $0.27\ M_\odot$ for comparisons with a 3D simulation in Section 3.3. We continue computational runs until the stellar mass reaches $10\ M_\odot$, except for the case of the low mass supply rate, i.e., $K = 0.1 K_{\rm fid}$. In this case, we stop the run when the stellar mass reaches $7\ M_\odot$ to avoid following long-term calculation, which does not affect our conclusions. We do not follow the evolution after the stellar mass exceeds $10 M_\odot$, in which the protostellar radiative feedback becomes efficient (e.g., Stacy et al., 2012; McKee & Tan, 2008; Hosokawa et al., 2011). The evolution under the influence of radiative feedback is beyond the scope of this work.

In this chapter, with the model presented above, we perform calculations for six cases in total. In Section 3.2.1, we show the results for the fiducial case with $K = K_{\rm fid}$ and $f_{\rm Kep} = 0.5$. In Section 3.2.2, we investigate the effects of varying the mass supply rate by setting $K = 0.1 K_{\rm fid}$ and $10 K_{\rm fid}$. In Section 3.2.3, we study the effects of varying the envelope rotation with $f_{\rm Kep} = 0.3$ and 0.8. In Section 3.3, we show the case tuned for a comparison with the 3D hydrodynamic simulation.

3.2 Results

3.2.1 Fiducial Case

3.2.1.1 Disk Structure

In this section, we overview the results of the fiducial case, where $K = K_{\rm fid}$ and $f_{\rm Kep}$ is 0.5. Figure 3.2 shows the disk structure at the different epochs when $M_* = 0.1\ M_\odot$, $1\ M_\odot$, and $10\ M_\odot$. To understand the evolution in this figure, we also present radial distributions of chemical abundances and effective heating and cooling rates for $\varpi < 60$ AU at epochs when $M_* = 1\ M_\odot$ and $10\ M_\odot$ in Figures 3.3 and 3.4.

Figure 3.2 overall shows that the disk gradually expands as the stellar mass increases. The disk size is ~ 1 AU when $M_* = 0.1\ M_\odot$ and $\sim 10^3$ AU when $M_* = 10\ M_\odot$. Figure 3.2(f) shows that the Toomre Q parameter is always regulated to a nearly constant value

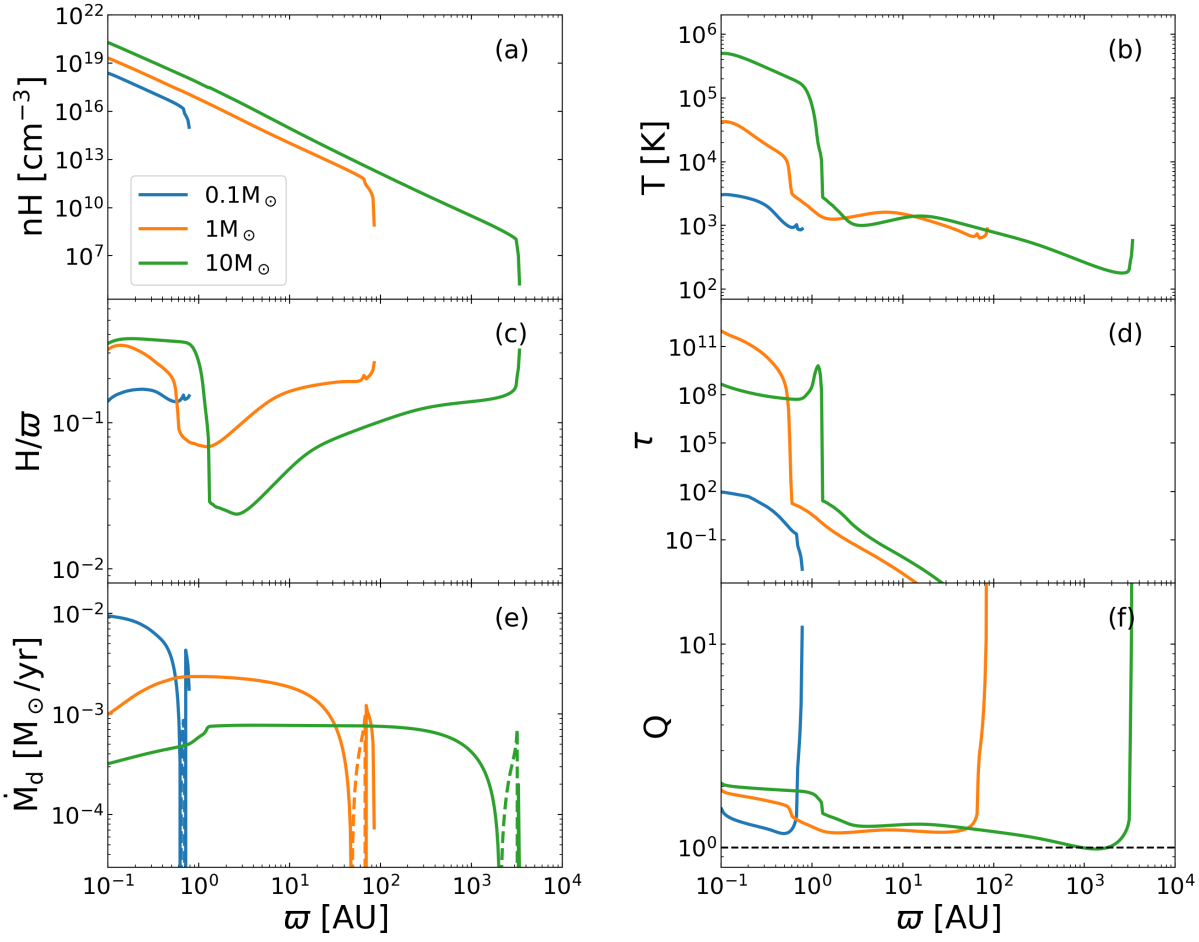

Figure 3.2: Temporal evolution of the disk structure in the fiducial model, where $K = K_{\rm fid}$ and $f_{\rm Kep} = 0.5$. The line colors denote the different epochs when the stellar mass is 0.1 $M_\odot$ (blue), 1 $M_\odot$ (orange), and 10 $M_\odot$ (green). Panels show the radial distributions of (a) gas number density, (b) temperature, (c) disk aspect ratio, (d) optical depth in the vertical direction, (e) accretion rate through the disk, and (f) Toomre Q parameter. In Panel (e), the solid and dashed lines denote the inward and outward flow, respectively. The horizontal line in Panel (f) represents $Q = 1$. This figure is taken from Kimura et al. (2021).

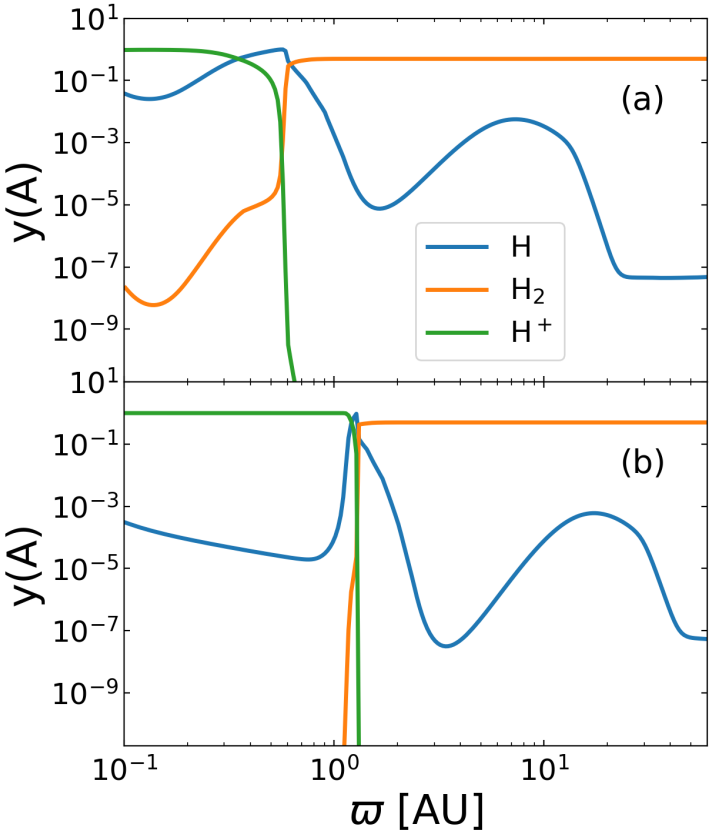

Figure 3.3: The chemical abundances within the disk in the fiducial case for $\varpi < 60$ AU. Panels (a) and (b) correspond to the snapshots at the different epochs when $M_* = 1\ M_\odot$ and 10 $M_\odot$. The blue, orange, and green lines denote the number fractions of H, H_2, and H^+, respectively. This figure is taken from Kimura et al. (2021).

of $Q \sim 1$ throughout the disk, except the outermost part. This is a typical feature of the self-gravitating disks, as found in previous steady 1D models (Tanaka & Omukai, 2014; Matsukoba et al., 2019).

Figure 3.2(a) shows that the density on the disk midplane sharply decreases outward. This behavior is approximately fitted by the power-law function $n_{\rm H} \propto \varpi^{-3}$ and well understood by the following analytical argument. As the disk is marginally stable ($Q \sim 1$), Equation (3.23) gives

$$\Sigma \sim \frac{c_s \Omega}{\pi G}. \tag{3.33}$$

Substituting this into Equation (3.28), we get

$$\rho_0 = \frac{\Sigma}{\sqrt{2\pi} H} \sim \frac{\Omega^2}{\sqrt{2\pi^3 G}} \propto \varpi^{-3}. \tag{3.34}$$

As seen in Figure 3.2(b), the midplane temperature throughout the disk is a few thousand Kelvin when $M_* = 0.1\ M_\odot$. However, in the later snapshots, the temperature dramatically rises only for $\varpi \lesssim 1$ AU and remains at $\sim$ 100–1000 K on the outside. Figure 3.3 shows that the cooler outer part is almost fully molecular, and Figure 3.4 indicates that the viscous heating is in balance with the H_2 molecular cooling via optically

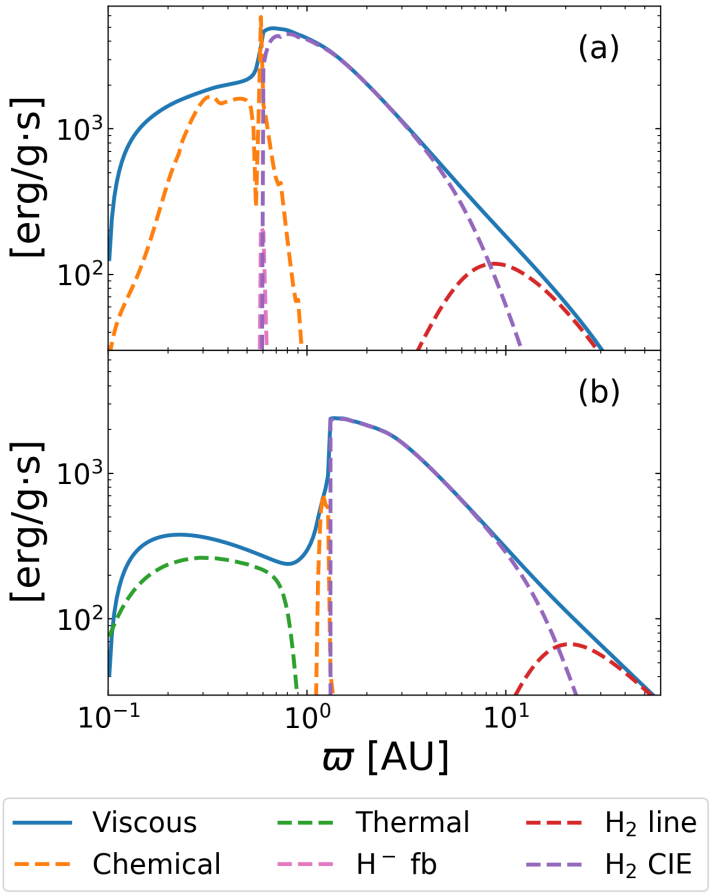

Figure 3.4: Radial distributions of heating and cooling rates for $\varpi < 60$ AU in the fiducial case. Panels (a) and (b) are the snapshots at the same epochs as in Figure 3.3, when $M_* = 1\ M_\odot$ and $10\ M_\odot$. The solid and dashed lines denote the heating and cooling processes, respectively. The line colors correspond to the individual processes as follows: the viscous heating (blue), the endotherm by chemical reactions (orange), the radiative cooling via the H_2 line emission (red), H_2 collisional induced emission (purple), H^- free-bound emission (magenta), and thermal continuum emission (green). This figure is taken from Kimura et al. (2021).

thin continuum and line emission (see also Figure 3.2d). On the other hand, Figure 3.3 also shows that H_2 molecules are almost completely dissociated in the hot inner region. The hot inner region emerges because, as shown in Figure 3.2(d), the optical depth over the disk scale height $\tau_R = \kappa_R \Sigma/2$ abruptly increases when the temperature exceeds ~ 3000 K. This is caused by the bound-free absorption of H^- contributing to the opacity κ_R (Mayer & Duschl, 2005). With increasing τ_R, the efficiency of radiative cooling decreases, and temperature increases due to the viscous heating. With the increasing temperature, hydrogen molecules are dissociated and atoms are ionized through efficient collisions, which absorb the gas thermal energy. However, with hydrogen fully ionized, such endothermic reaction becomes unavailable from the inside out (Figures 3.3a and 3.4a[1]). As a result, the temperature rapidly rises without effective cooling. Such vigorous heating continues until the temperature reaches $\sim 10^5$ K, above which the opacity approaches the Thomson

[1]The viscous heating significantly decreases near the inner boundary owing to the zero-torque boundary condition.

scattering value. The radiative cooling effectively operates again and balances with the viscous heating (Figure 3.4b). Note that, even at $M_* = 10\ M_\odot$, the effective temperature at the disk surface is estimated as only $\simeq 4000$ K from Equation (3.31). The ultraviolet radiation from the hot inner region is thus too weak to induce photoevaporation in the outer part of the disk.

In Figure 3.2(c), we show the evolution of the disk aspect ratio H/ϖ. H/ϖ at a fixed radius gets lower with the increasing stellar mass, except the innermost region where $\varpi \lesssim 1$ AU for $M_* \gtrsim 1\ M_\odot$. That part has an aspect ratio of nearly 0.3, which corresponds to the hot optically thick region mentioned above. However, in the outer part with $T \lesssim 10^3$ K, where the fragmentation is expected to occur, our thin disk approximation $H/\varpi \ll 1$ is still valid. We note that previous 3D simulations mask the vicinity of the star by the sink cells or particles and do not spatially resolve the hot inner region. Further investigation is necessary for understanding the innermost structure of the disk and its role in the primordial star formation.

Figure 3.2(e) shows the accretion rates through the disk $\dot{M}_{\rm d}$. The accretion rates averaged over the disk decrease as the stellar mass increases. This occurs along with the decrease in the mass supply rate from the envelope, as seen in the next section. We can also see that the gas moves inward at the outer edge of the disk in Figure 3.2(e). Such inward motion is induced by the direct mass supply from the envelope to the inner radius, which corresponds to the second term on the right-hand side of Equation (3.20). The gas would move outward at the outermost part only through the viscous evolution, as shown in Lynden-Bell & Pringle (1974). Moreover, for $M_* \gtrsim 1\ M_\odot$, $\dot{M}_{\rm d}$ gradually decreases inward in the hot inner part. This feature is not observed in previous models that assume a constant accretion rate throughout the disk. Figure 3.2(f) indicates that Q in the corresponding area is slightly higher than that in the outer region, suggesting that $\dot{M}_{\rm d}$ declines due to the decrease of the gravitational torque. Since $\dot{M}_{\rm d}$ decreases with the decreasing ϖ, the mass transported from the outside gradually accumulates in the hot ionized part. This effect increases the surface density and the gravitational torque over the time scale of $\tau_{\rm vis} \sim \varpi^2/\nu$. However, as mentioned earlier, viscous heating causes a rapid increase in the temperature until it reaches $\sim 10^5$ K, above which the opacity almost converges to the Thomson scattering value. The heating effect reduces the gravitational torque over the timescale of $\tau_{\rm heat} \sim e_{\rm th}/\nu\Omega^2 \sim c_s^2/\nu\Omega^2 \sim H^2/\nu$. Which of the above competing effects is more effective depends on the timescale ratio $\tau_{\rm heat}/\tau_{\rm vis} \sim H^2/\varpi^2$, which is smaller than unity (see Figure 3.2c). Therefore, the gravitational torque remains inefficient in the hot ionized part for some time after the temperature settles down to $T \simeq 10^5$ K.

3.2.1.2 Disk-to-Star Mass Ratio

Figure 3.5(a) shows the time evolution of the total mass supply rate from the envelope to the disk $\dot{M}_{\rm e,tot}$, the accretion rate from the disk to the central star $\dot{M}_*$, and the radial maximum of the disk accretion rate $\dot{M}_{\rm d,max}$. In Figure 3.5(b), we show the ratio $\dot{M}_{\rm d,max}/\dot{M}_{\rm e,tot}$. Concerning the accretion rate onto the star, strictly speaking, an additional supply rate directly from the envelope onto the star exists. However, this is much smaller than $\dot{M}_*$ except immediately after the birth of the protostar. Hence, we only consider $\dot{M}_*$ here. We take the time average of $\dot{M}_{\rm d,max}$ over $\Delta \log(M_*) = 0.1$. This is for removing numerical oscillations caused by the limited spatial resolution near the boundary between the inner optically thick and outer optically thin regions of the disk. We have checked that these artifacts have little impact on the overall evolution by

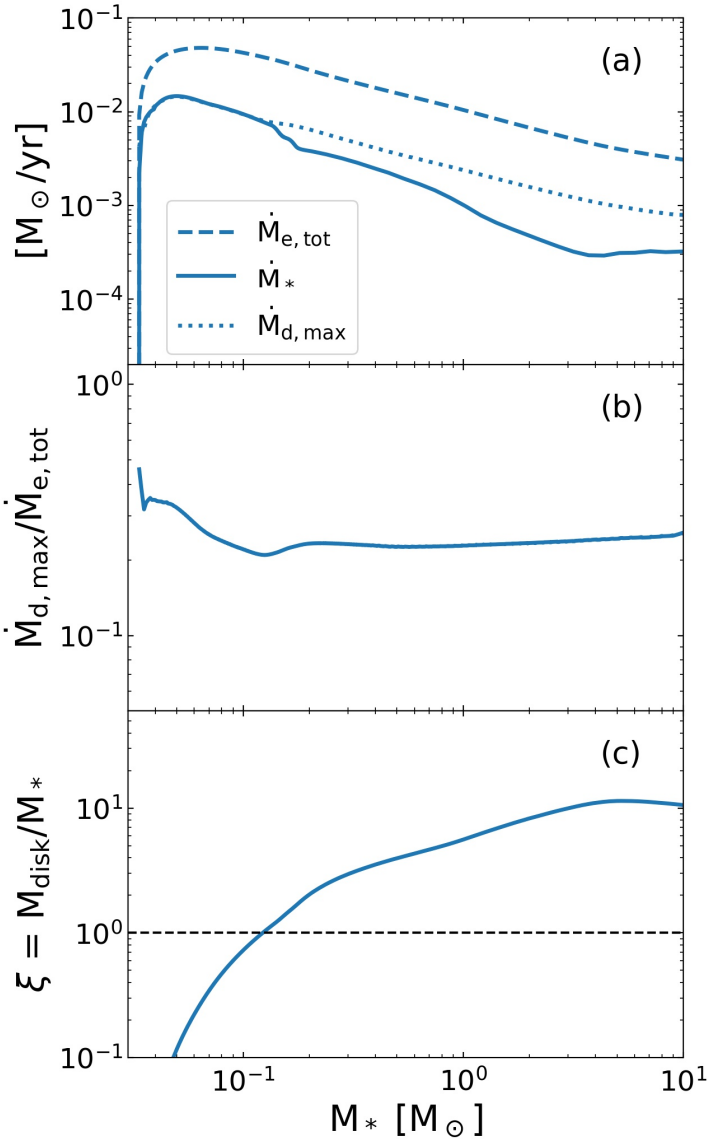

Figure 3.5: Evolution of the mass flux balance through the disk and disk mass growth history against the stellar mass M_* in the fiducial case. Panel (a) presents the evolution of the total mass supply rate from the envelope onto the disk $\dot{M}_{\rm e,tot}$ (dashed line), the accretion rate from the disk onto the star $\dot{M}_*$ (solid line), and the radial maximum of the disk accretion rate $\dot{M}_{\rm d,max}$ (dotted line, also see text). Panel (b) shows the evolution of the ratio of $\dot{M}_{\rm d,max}$ to $\dot{M}_{\rm e,tot}$. Panel (c) presents the evolution of the disk-to-star mass ratio $\xi \equiv M_{\rm disk}/M_*$, and the horizontal line denotes unity. This figure is taken from Kimura et al. (2021).

performing experimental calculations with higher resolution. We note that $\dot{M}_{\rm d,max}$ represents the nearly constant value at the outer part of the disk, which is larger than that in the hot inner part as seen in Figure 3.2(e).

Figure 3.5(a) indicates that $\dot{M}_{\rm e,tot}$ gradually decreases with the increasing stellar mass. This behavior is induced by the structure of the assumed accretion envelope. Furthermore, $\dot{M}_*$ and $\dot{M}_{\rm d,max}$ are an order of magnitude smaller than $\dot{M}_{\rm e,tot}$, although they are often assumed to be equal in previous steady models. The ratio $\dot{M}_*/\dot{M}_{\rm e,tot}$ fluctuates around ~ 0.1, and, as shown in Figure 3.5(b), the ratio $\dot{M}_{\rm d,max}/\dot{M}_{\rm e,tot}$ remains $\simeq 0.2$ throughout

the evolution. This means that most of the infalling gas from the envelope cannot accrete onto the star through the disk. As seen in Figure 3.5(c), when the stellar mass reaches $\sim 0.1\ M_\odot$, the disk becomes more massive than the star. In the fiducial case, the disk mass grows up to 10 times the central stellar mass by the end of the calculation. The evolution of the disk-to-star mass ratio ξ can be described as follows:

$$\begin{aligned} \dot{\xi} &= \frac{d}{dt}\left(\frac{M_{\rm disk}}{M_*}\right) \\ &= \frac{M_*\dot{M}_{\rm e,tot} - (M_* + M_{\rm disk})\dot{M}_*}{M_*^2}. \end{aligned} \tag{3.35}$$

Equation (3.35) implies that ξ stops increasing, i.e., $\dot{\xi} \sim 0$ when $\xi \sim (\dot{M}_{\rm e,tot} - \dot{M}_*)/\dot{M}_* \sim 10$, which is in good agreement with the evolution shown in Figure 3.5(c). The disk-to-star mass ratio ξ is a critical parameter related to the disk fragmentation, as we will discuss in more detail in Section 3.4.1.

Here we develop an analytical model for the accretion rate through the disk to understand the behavior of the disk-to-star mass ratio ξ. We assume that the mass supply from the envelope causes the disk to spread by $d\varpi_{\rm d}$ during the time interval dt, where $\varpi_{\rm d}$ is the radius of the outer disk edge. Below, we consider mass conservation through the annulus whose inner and outer radii are $\varpi_{\rm d}$ and $\varpi_{\rm d} + d\varpi_{\rm d}$. We define the accretion rate at the inner radius as $\dot{M}_{\rm d,edge} \equiv \dot{M}_{\rm d}(\varpi_{\rm d})$ and assume that all the mass supply from the envelope $\dot{M}_{\rm e,tot}$ concentrates on this annulus. Here, $\dot{M}_{\rm d,edge}$ corresponds to $\dot{M}_{\rm d,max}$ in Figure 3.5, and we can regard it as the accretion rate in the outer region. The mass conservation is written as

$$dM = \dot{M}_{\rm e,tot}dt - \dot{M}_{\rm d,edge}dt, \tag{3.36}$$

where dM is the mass increment of the annulus. We further assume that, in the annulus, the gravitational torque regulates the Toomre Q parameter to a constant value $Q_{\rm crit}$. Here, $Q_{\rm crit}$ is the critical value above which the gravitational torque is ineffective. Since the surface density Σ is described as

$$\Sigma = \frac{c_s\Omega}{\pi G Q_{\rm crit}}, \tag{3.37}$$

the mass increment dM can be written as

$$dM = 2\pi\varpi_{\rm d}d\varpi_{\rm d}\Sigma = \frac{2\varpi_{\rm d}c_s\Omega}{GQ_{\rm crit}}d\varpi_{\rm d}. \tag{3.38}$$

From Equations (3.36) and (3.38), we get

$$\begin{aligned} \frac{\dot{M}_{\rm d,edge}}{\dot{M}_{\rm e,tot}} &= 1 - \frac{1}{\dot{M}_{\rm e,tot}}\frac{dM}{dt} \\ &= 1 - \frac{1}{\dot{M}_{\rm e,tot}}\frac{2\varpi_{\rm d}c_s\Omega}{GQ_{\rm crit}}\frac{d\varpi_{\rm d}}{dt}. \end{aligned} \tag{3.39}$$

Due to the second term on the right-hand side, $\dot{M}_{\rm d,edge}$ takes the different value from $\dot{M}_{\rm e,tot}$. This term represents the effect of the disk spread owing to the angular momentum of the infalling gas. In other words, the gas supply from the envelope is used to extend

the outer disk edge. If the disk does not spread or $d\varpi_{\rm d} = 0$, Equation (3.39) gives $\dot{M}_{\rm d,edge} = \dot{M}_{\rm e,tot}$. To rewrite the second term, we approximately describe the effective equation of state within the disk as

$$T = f_T \times 200 \left(\frac{K}{K_{\rm fid}}\right) \left(\frac{n_{\rm H}}{10^4 {\rm cm}^{-3}}\right)^{0.1} {\rm K}, \tag{3.40}$$

where f_T is the temperature ratio of the envelope and disk as the envelope temperature is described by Equation 3.3 for the fiducial case and proportional to K. In the fiducial case, Equation (3.40) with $f_T = 0.4$ provides a good description of the temperature profiles on the disk midplane, except the hot inner region. We can rewrite the second term in Equation (3.39) with Equation (3.40) as described in Appendix A, and finally get

$$\frac{\dot{M}_{\rm d,edge}}{\dot{M}_{\rm e,tot}} = 1 - 0.68 \left(\frac{Q_{\rm crit}}{1.0}\right)^{-21/20} \left(\frac{f_T}{0.4}\right)^{1/2} \left(\frac{f_{\rm Kep}}{0.5}\right)^{7/10}. \tag{3.41}$$

This equation implies that the ratio $\dot{M}_{\rm d,edge}/\dot{M}_{\rm e,tot}$ is independent of the stellar mass M_* and remains ~ 0.3 throughout the evolution in the fiducial case. These features are consistent with our numerical results shown in Figure 3.5(b) where $\dot{M}_{\rm d,max}/\dot{M}_{\rm e,tot}$ remains ~ 0.2. Note that our formulation breaks down when Equation (3.41) returns negative values for $\dot{M}_{\rm d,edge}/\dot{M}_{\rm e,tot}$,. In this case, $\dot{M}_{\rm d,edge}$ is negative because the mass supply $\dot{M}_{\rm e,tot}dt$ is less than the increment of the disk mass dM under the assumption that $Q \sim Q_{\rm crit}$ in equation (3.36). In other words, the mass supply rate is insufficient to maintain $Q < Q_{\rm crit}$. Therefore, our assumption that the gravitational torque regulates Toomre Q parameter to $Q_{\rm crit}$ is no longer valid.

As we can see in Figure 3.5(a), the accretion rate onto the star $\dot{M}_*$ is the same as the maximum disk accretion rate $\dot{M}_{\rm d,max}$ for $M_* < 0.1\ M_\odot$. After that, the hot inner part emerges. As a result, $\dot{M}_*$ becomes slightly lower than $\dot{M}_{\rm d,max}$ (see also Figure 3.2e). Moreover, at $M_* \simeq 4\ M_\odot$, $\dot{M}_*$ begins to increase and approaches $\dot{M}_{\rm d,max}$. When M_* reaches 4 $M_\odot$, the opacity almost converges to the Thomson scattering value, and the radiative cooling efficiently operates. Thus, $t_{\rm heat}/t_{\rm vis}$ becomes greater than unity, and $\dot{M}_{\rm d,max}$ and $\dot{M}_*$ get closer with each other as seen in Section 3.2.1.1.

3.2.2 Effects of Varying Mass Supply Rates

In this section, we consider the cases with $K = 0.1K_{\rm fid}$, $K_{\rm fid}$, and $10K_{\rm fid}$ (see Equations 3.1 and 3.2), to investigate the effects of varying the mass supply rate from the accretion envelope onto the disk. For these cases, we fix the envelope rotation at $f_{\rm Kep} = 0.5$. In fact, the mass supply rate varies depending on different properties of star-forming clouds, as shown in previous cosmological simulations (e.g., Hirano et al., 2014, 2015). In the fiducial case with $K = K_{\rm fid}$ a supply rate is $\sim 10^{-2} M_\odot$ yr^{-1}, which is typical in ordinal primordial star formation. The supply rate for the case with $K = 0.1K_{\rm fid}$ is $\sim 1/50$ times lower than that of the fiducial case. Such low rates are realized in the so-called Pop III.2 cases, where HD cooling is effective during the cloud collapse (e.g., Yoshida et al., 2007; Hosokawa et al., 2012b). The rate for the case with $K = 10K_{\rm fid}$ is ~ 50 times larger than the standard value, and it almost corresponds to the DC scenario.

Figure 3.6 shows the disk structure when $M_* = 1M_\odot$ for these cases. Figure3.6(c) demonstrates that the mean accretion rate through the disk is lower for cases with the lower K, i.e., the lower mass supply rates. We note that, for lower K, the envelope gas

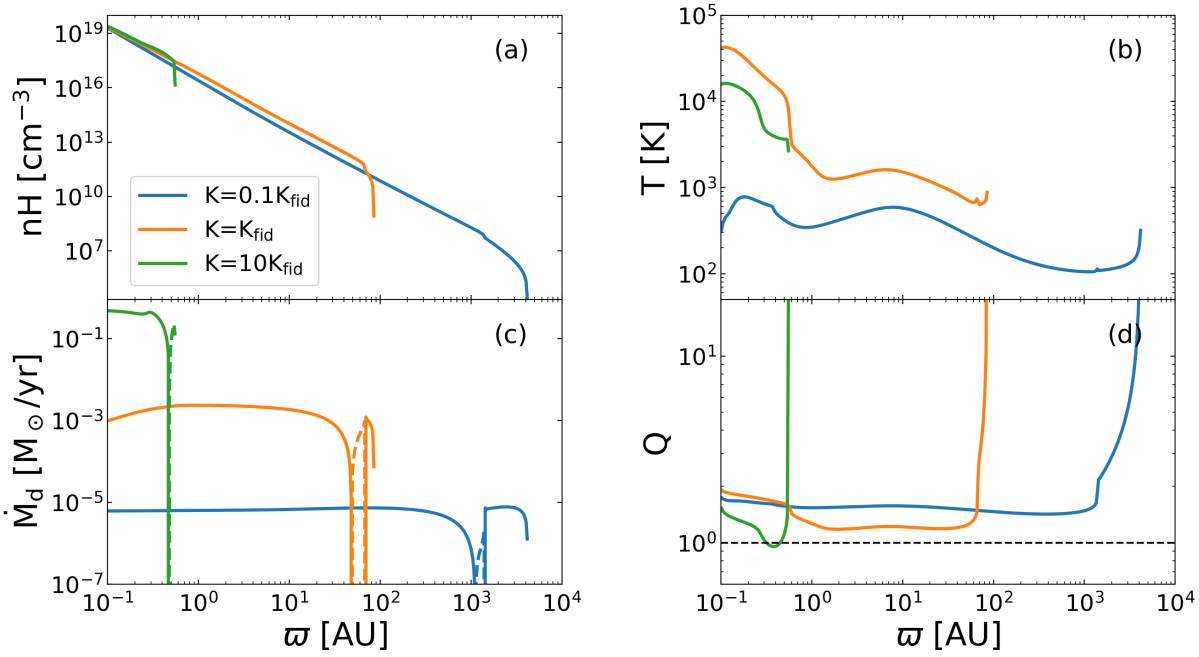

Figure 3.6: Variations of the disk structure with different mass supply rates from the envelope. The blue, orange, and green lines denote the cases with $K = 0.1\ K_{\rm fid}$, $K_{\rm fid}$, and $10\ K_{\rm fid}$, respectively. We assume the same rotation parameter $f_{\rm Kep} = 0.5$ for these cases. The presented snapshots correspond to the epochs when the stellar mass is 1 $M_\odot$ in each case. Panels show the radial distributions of (a) temperature, (b) number density, (c) accretion rate through the disk, and (d) Toomre Q parameter. In Panel (c), the solid and dashed lines represent the inward and outward flow, respectively. The horizontal line in Panel (d) indicates $Q = 1$. This figure is taken from Kimura et al. (2021).

initially located at the outer region falls onto the disk until the stellar mass reaches $1M_\odot$, as the envelope density is lower. Consequently, the disk size is larger due to the conservation of angular momentum. As seen in Figure3.6(d), $Q \sim 1$ throughout the disk for all the presented cases, although the averaged value is slightly lower with the higher K. For the case with $K = 10\ K_{\rm fid}$, where the disk accretion rate is highest, the minimum value of Q is slightly below unity at $\varpi \simeq 0.4$ AU. The previous steady models also exhibit the same trend that the disk becomes more gravitationally unstable with increasing the disk accretion rate (Matsukoba et al., 2019). Figure 3.6(a) shows that the number density approximately follows the power-law distribution $\rho \propto \varpi^{-3}$ shown by Equation (3.34) for all cases where $Q \sim 1$. The temperature distributions are presented in Figure 3.6(b). For the case with $K = 0.1K_{\rm fid}$, the temperature is less than 10^3 K throughout the disk, as Q is large and the viscous heating is weak. There is no hot ionized region, which emerges once the temperature reaches $\simeq 3000$ K (see Section 3.2.1.1).

In Figure3.7(a), we show the time evolution of the mass supply rate from the envelope $\dot{M}_{\rm e,tot}$ and the accretion rate from the disk to the central star $\dot{M}$. In all the cases, $\dot{M}_*$ is an order of magnitude smaller than $\dot{M}_{\rm e,tot}$, and the disk-to-star mass ratio ξ rises above unity when $M_* \lesssim 1\ M_\odot$, as shown in Figure3.7(c). Figure 3.7(b) describes the ratio of the maximum disk accretion rate $\dot{M}_{\rm d,max}$ to the mass supply rate $\dot{M}_{\rm e,tot}$. We find that, for the case with $K = 0.1K_{\rm fid}$, $\dot{M}_{\rm d,max}/\dot{M}_{\rm e,tot}$ takes almost constant value throughout the evolution, as in the fiducial case, and smaller than that in the other cases. This feature

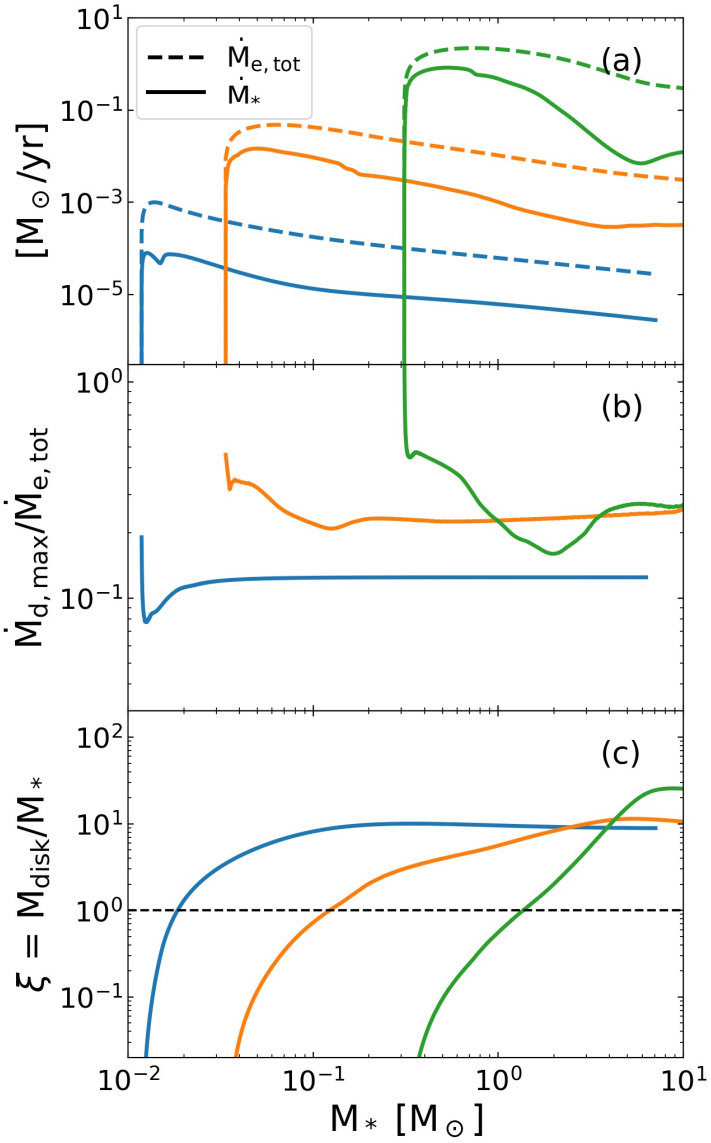

Figure 3.7: Almost the same as Figure 3.5 but for the cases with different mass supply rates from the envelope. The line colors denote the same cases as in Figure 3.6: $K = 0.1K_{\rm fid}$ (blue), $K_{\rm fid}$ (orange), $10K_{\rm fid}$ (green). In Panel (a), we refrain from showing the radial maximum of the disk accretion rate $\dot{M}_{\rm d,max}$ for clarity, unlike in Figure 3.5. This figure is taken from Kimura et al. (2021).

can be interpreted with Equation (3.41) as follows. As shown in Figure3.6(b), the overall disk temperature is lower with the lower K. The envelope temperature is also lower following the effective equation of state $P = K\rho^\gamma$. However, our models generally show that the decrease in the disk temperature is always milder than that of the envelope temperature. Consequently, the temperature ratio f_T tends to be larger with the lower K, for which Equation (3.41) gives the smaller $\dot{M}_{\rm d,max}/\dot{M}_{\rm e,tot}$.

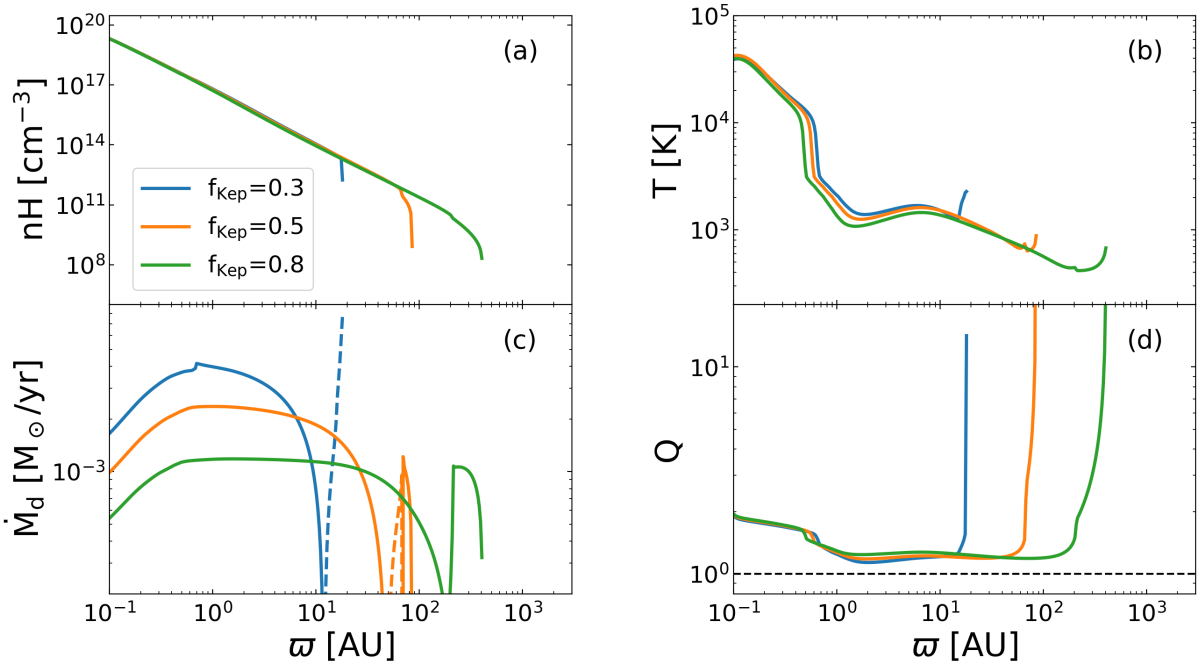

Figure 3.8: Same as Figure 3.6 but for the cases with the different rotational strength of the envelope, i.e., with $f_{\rm Kep} = 0.3$ (blue), 0.5 (orange), and 0.8 (green). We asuume the same parameter $K = K_{\rm fid}$ (see Equations 3.5 and 3.5) for these cases. The presented snapshots correspond to the epochs when $M_* = 1\ M_\odot$ in each case. This figure is taken from Kimura et al. (2021).

3.2.3 Effects of Varying Rotation of Envelope

We next show the results for the cases with $f_{\rm Kep} = 0.3$, 0.5, and 0.8, with the fixed $K = K_{\rm fid}$, to understand the impact of varying the rotation of the envelope. A large sample of primordial star-forming clouds exhibits some scatter of $f_{\rm Kep}$ around the typical value of 0.5 (e.g., Hirano et al., 2014).

In Figure 3.8, we show the disk structure when $M_* = 1 M_\odot$ for these cases. The disk structure is almost identical for all the cases, apart from the disk size and the accretion rate through the disk. The disk size is larger with the higher $f_{\rm Kep}$, i.e., with the faster rotation of the envelope owing to the angular momentum conservation. As shown in Figure3.8(c), the accretion rate through the disk $\dot{M}_{\rm d}$ is smaller with the higher $f_{\rm Kep}$ onaverage. This feature, as described below, agrees with Equation (3.41).

Figure 3.9(a) shows the time evolution of the mass supply rate from the envelope $\dot{M}_{\rm e,tot}$, and the accretion rate from the disk to the central star $\dot{M}$. Although both the rates $\dot{M}_*$ and $\dot{M}_{\rm e,tot}$ are lower with the higher $f_{\rm Kep}$ at a given stellar mass, $\dot{M}_*$ is more than an order of magnitude smaller than $\dot{M}_{\rm e,tot}$ in general. The disk-to-star mass ratio ξ exceeds unity well before M_* reaches $1 M_\odot$ for all the cases as shown in Figure 3.9(c). In Figure3.9(b), we show the ratio $\dot{M}_{\rm d,max}/\dot{M}_{\rm e,tot}$. We find that this ratio is systematically higher with the lower $f_{\rm Kep}$ and nearly constant throughout the evolution in all cases. Equation (3.41) well explains such dependencies on $f_{\rm Kep}$.

Stacy & Bromm (2014) report that the evolution of the total stellar and disk masses significantly changes depending on the spin of star-forming clouds taken from cosmological

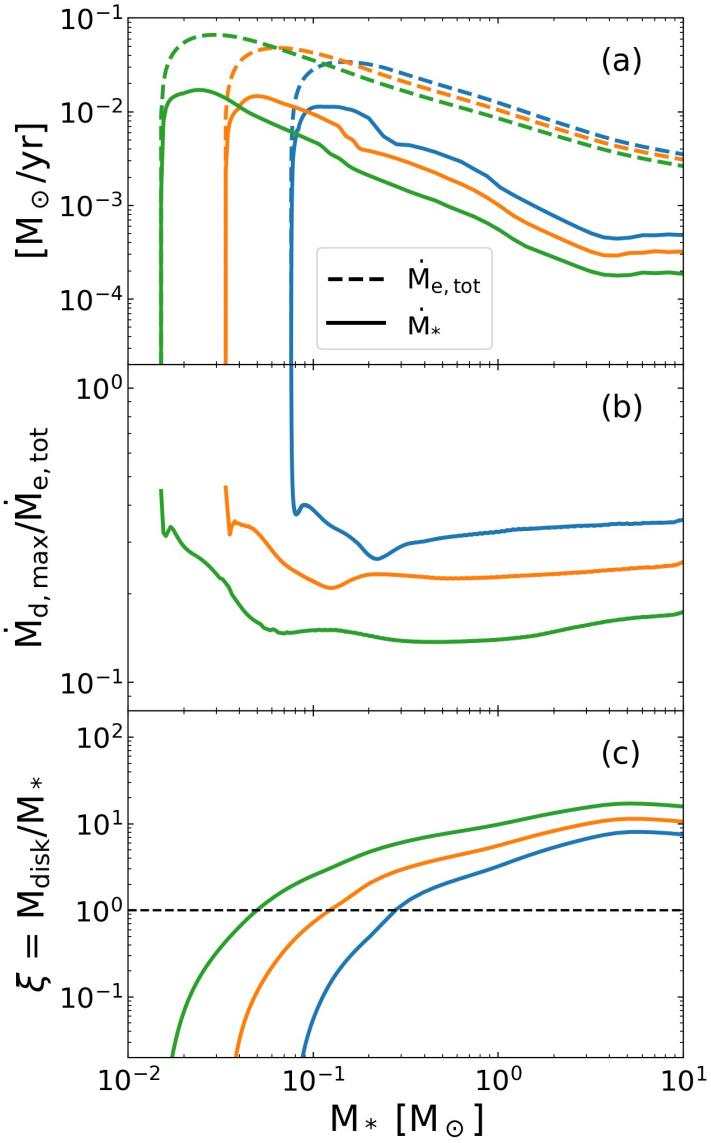

Figure 3.9: Same as Figure 3.7 but for the same cases as presented in Figure 3.8, i.e., cases with $f_{\rm Kep} = 0.3$ (blue), 0.5 (orange), and 0.8 (green). This figure is taken from Kimura et al. (2021).

simulations, which seems to contradict our results. However, we note that they also show a systematic correlation between the mass supply rate from the envelope and the cloud's spin: the lower rate with the higher spin. In this study, we examine these effects separately. The evolution in our model exhibits the same dependence on the mass supply rate as in Stacy & Bromm (2014) (see Section 3.2.2).

3.3 Comparison with 3D Simulation

We perform a 3D hydrodynamic simulation using the code SFUMATO-RT developed in Sugimura et al. (2020) with some modifications. Sugimura et al. (2020) have implemented radiative transfer from primordial protostars to the AMR code SFUMATO (Matsumoto 2007). Additionally, they have implemented heating and cooling processes

and a chemical network of pristine gas relevant for the density of $n_{\rm H} < 10^{13}$ cm^{-3}. They pick up a typical primordial star-forming cloud from the cosmological simulations (Hirano et al. 2014; Hirano et al. 2015) and set it as the initial condition. They set the sink radius as $r_{\rm sink} = 64$ AU and follow the long-term evolution over 1.2×10^5 yr after the birth of the protostar until protostellar radiative feedback determines the final stellar masses. In their simulation, the first disk fragmentation takes place at ~ 1000 yr after the first protostar formation, when $M_* \simeq 10\ M_\odot$.

Previous simulations already demonstrate that the disk tends to fragment earlier with a higher spatial resolution. For example, Clark et al. (2011) follow the evolution with a sink radius of 0.5 AU, showing that disk fragmentation occurs when $M_* \simeq 0.5\ M_\odot$. Moreover, Greif et al. (2012) perform simulations with the higher resolution of 0.05 $R_\odot$ and report that the disk fragments when M_* is less than 0.1 $M_\odot$ for all their examined cases. In this study, we also consider such early fragmentation when $M_* < 1\ M_\odot$, for which we have developed 1D non-steady model as presented in Section 3.2. We use the latest version of the code, which includes the cooling processes effective for the higher densities up to $n_{\rm H} \sim 10^{16}$ cm^{-3}, such as H^- free-free emission, H_2-H_2 and H_2-He collisional induced emission, and start the simulation from the same initial condition as in Sugimura et al. (2020). We set the sink radius to be more than a hundred times smaller than that in Sugimura et al. (2020), $r_{\rm sink} = 0.5$ AU. To reduce the computational cost, we ignore the irradiation from the accreting stars as its effect is too weak compared to compressional and viscous heating in the regime of our simulation (Clark et al., 2011).

Figure 3.10 shows the simulation snapshots of the number density of hydrogen nuclei from the face-on view at 50, 100, 220, and 230yr after the first protostellar birth. We observe that the disk forms around the central star and eventually fragments. The initial fragmentation occurs at ~ 220 yr after the protostar formation when the stellar mass reaches 0.73 $M_\odot$ (Panel c). White arrows in Panels (c) and (d) indicate the positions of a fragment. We end the simulation at 250 yr after the protostar formation.

For comparisons, we also calculate the disk evolution using the 1D model from the initial condition mimicking the envelope structure observed in the simulation. We set the parameters in Equations (3.1) and (3.2) to fit its profiles with the spherically-averaged profile of the simulation result. We adopt $K = 1.07 K_{\rm fid}$, $C_1 = 6.1 \times 10^7$, $C_2 = -4.5$, and $\gamma = 1.1$. Although C_1 and C_2 are originally constants and not parameters, we adjust C_2 so that the model envelope matches the simulation envelope. We take the inner boundary at 0.1 AU.

3.3.1 Disk Structure

In Figure 3.11, We show the radial distributions of the temperature and number density at the disk midplane in the model and the simulation at 100 yr after the protostellar birth. Although the disk gradually spreads due to the mass supply from the envelope, the temperature and density profiles are similar during most of our computational time. Thus, we consider the disk structure only at this epoch as a representative snapshot.

Figure 3.11(a) shows that the model and the simulation have a common trend that the temperature is several thousand Kelvin in the outer part ($\varpi > 0.5$ AU in the model and $\varpi > 1$ AU in the simulation) and it rapidly increases toward the central star. However, in the simulation data, the temperature is approximately twice as high as that in the model and rises monotonically as ϖ decreases. Similar trends are also found in the simulation results reported by Clark et al. (2011). As shown in Figure 3.11(b), the number densities

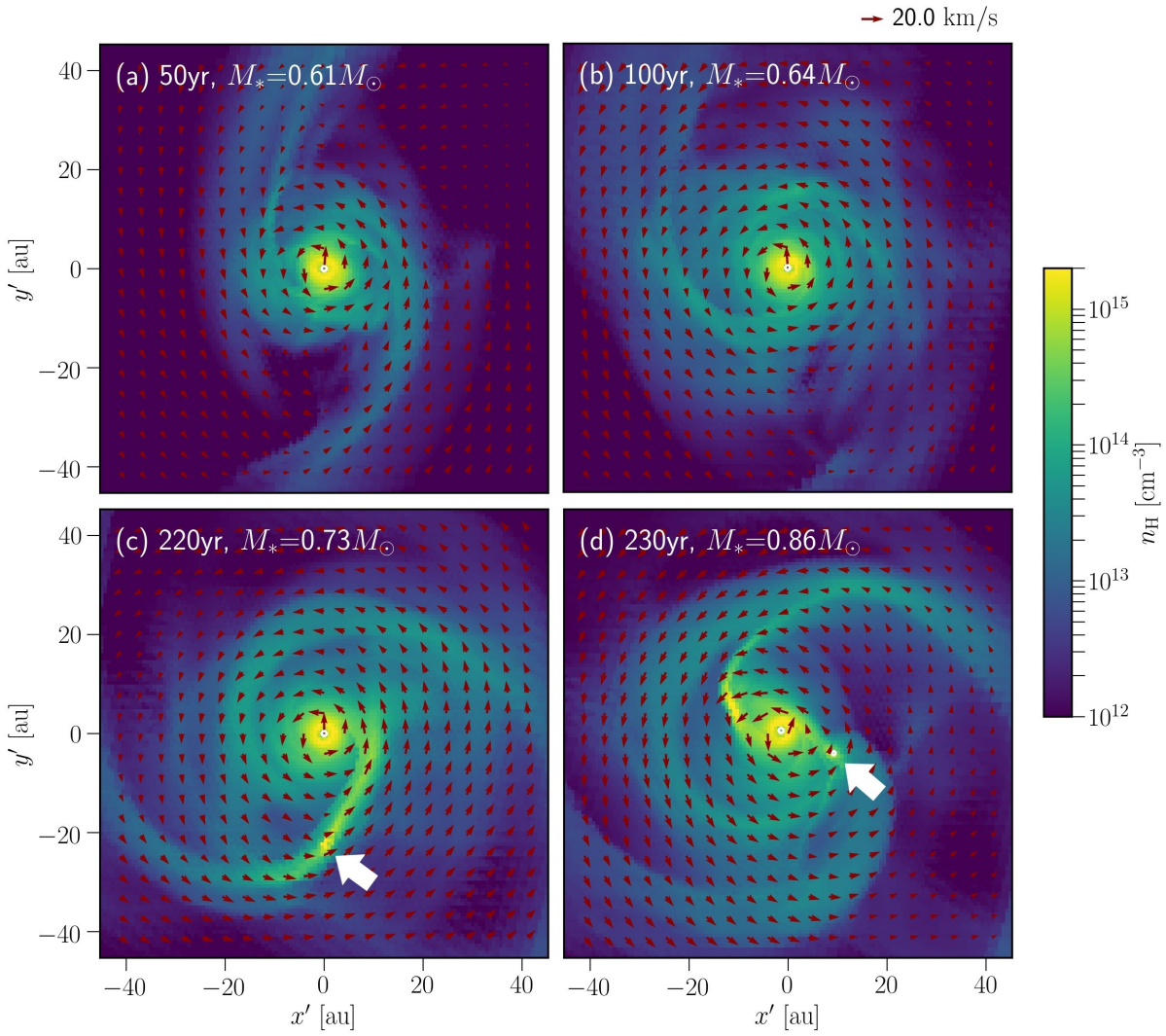

Figure 3.10: Evolution of the circumstellar disk observed in our 3D simulation. Four panels show the face-on views of the disk at different epochs: (a) 50 yr, (b) 100 yr, (c) 220 yr, and (d) 230 yr after the protostellar birth. The mass of the central star at each epoch is also displayed. In each panel, the color contour and red arrows denote the density and velocity distributions in the disk midplane. The thick white arrows in Panels (c) and (d) indicate the positions of a fragment. This figure is taken from Kimura et al. (2021).

are consistent in the range of $\varpi > 2$ AU. The simulation data shows the decline in the number density within $\varpi \simeq 2$ AU, which is attributed to the influence of the sink particle.

Although the disk has no distinct outer boundary in the simulation, we determine the disk size as follows. First, we estimate the radius $r(t)$ within which the gas reaches the disk by the time t using Equation (3.7) with the spherically-averaged radial velocity at the moment when the protostar forms. Next, using the envelope angular momentum $J_{\rm env}(r)$, we define the angular momentum supplied to the disk at the time t as $J_{\rm env}(t) = J_{\rm env}(r(t))$. Finally, we determine the disk size $\varpi_{\rm d}$ so that $J_{\rm disk}(\varpi_{\rm d})$ is equal to $J_{\rm env}(t)$. In Figure 3.11, the resulting outer disk boundary in the simulation is $\simeq 20$ AU, as denoted by the red arrow. The deviation from the model is less than a factor of two. Furthermore, the simulation data shows the low-temperature component ($T < 10^3$ K) in the outer region

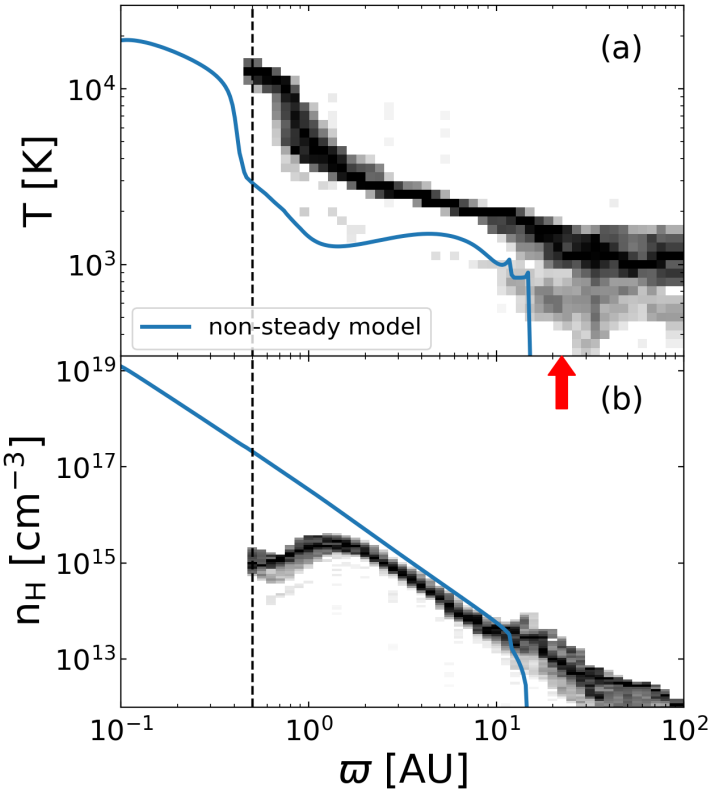

Figure 3.11: Comparisons of radial distributions of the (a) temperature and (b) number density between the non-steady model and simulation. The snapshots are taken at the same time as in Figure 3.10(b), the epoch of 100 yr after the protostellar birth. Blue solid lines denote the 1D non-steady model. Black shades show the mass distributions in the simulation data. The vertical dashed line indicates the sink radius of the simulation, 0.5 AU. The red arrow in Panel (b) marks the estimated outer disk boundary in the simulation (also see text). This figure is taken from Kimura et al. (2021).

of $\varpi \gtrsim 10$ AU. This is the residual of the original envelope structure. A similar low-temperature component originally exists for $\varpi \lesssim 10$ AU, but it disappears as the disk expands radially. This fact also demonstrates that the outer disk boundary is located at $\varpi \sim 10$ AU in the simulation data.

3.3.2 Accretion Rate and Disk-to-Star Mass Ratio

In this section, we make a comparison of the evolution of the accretion rate onto the star $\dot{M}_*$ and the disk-to-star mass ratio $\xi = M_{\rm disk}/M_*$ in our non-steady model and the simulation. As for ξ, we also show the result of the previous steady model for comparison. In Figure 3.12, we show the mass accretion histories onto the central star in the model and the simulation. The vertical lines indicate the elapsed times of 50, 100, 220, and 230 yr after the protostellar birth, which correspond to the snapshots in Figure 3.10. While the accretion rates in the simulation show the substantial time variability, the mean rates in the model are only slightly larger than those in the simulation until 220 yr. The accretion rate in the simulation rapidly increases for $t > 220$ yr, which leads to the burst-like event at $t \simeq 240$yr. This is attributed to the inward migration of the fragment, as shown in Figure3.10(c) and (d).

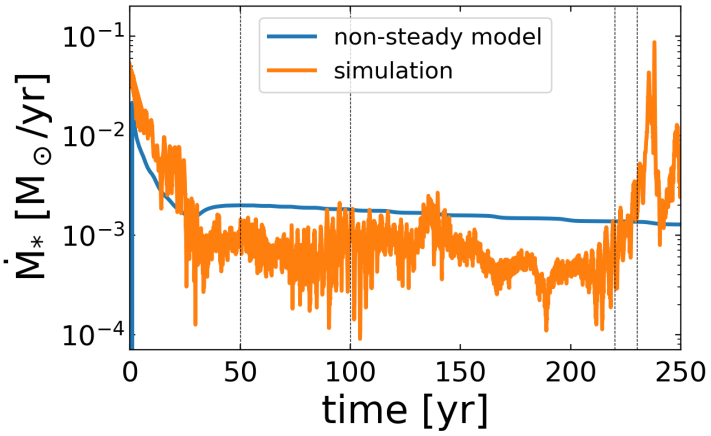

Figure 3.12: Comparisons between the non-steady model (blue) and simulation (orange), on the mass accretion histories onto the central star. The time for the simulation is measured from the formation of the first sink. Vertical lines denote the epochs of 50, 100, 220, and 230 yr after the protostellar birth, which correspond to the snapshots shown in Figure 3.10. This figure is taken from Kimura et al. (2021).

Figure 3.13 presents the evolution of the disk-to-star mass ratio ξ. For comparison, we here also reproduce the steady disk model by Tanaka & Omukai (2014) in addition to our non-steady model and 3D simulation. In our non-steady disk model (blue line), ξ rapidly increases in the beginning, and the disk mass exceeds the stellar mass at $M_* \simeq 0.45\ M_\odot$. Subsequently, ξ gradually increases, finally reaching ~ 10. This is because the accretion rate onto the star is an order of magnitude lower than the mass supply rate from the envelope, as discussed in Section 3.2.1.2. The simulation (orange dots) also shows that ξ rapidly rises in the beginning. The mass ratio ξ exceeds unity at $M_* \simeq 0.6 M_\odot$, and the disk fragmentation occurs at $M_* \simeq 0.73\ M_\odot$ when $\xi \simeq 3.9$. This suggests that in the simulation only a fraction of the total gas supplied from the envelope is transferred to the protostar via the gravitational torque as in the non-steady model. The green line represents ξ of the steady model by Tanaka & Omukai (2014). They consider the envelope structure with thermal evolution during the collapse calculated by a one-zone model (Omukai et al., 2005; Hosokawa & Omukai, 2009a). They assume the accretion rate through the disk is equal to that from the envelope, $\dot{M} \sim c_s^3/G$. In their model, the central stellar mass is estimated as the total mass supplied from the envelope by a given epoch under the assumption that the stellar mass always dominates the disk mass. Contrary to our non-steady model and simulation, ξ remains almost constant at 0.2–0.3 throughout the evolution in their model.

3.4 Discussion

3.4.1 Instability of Massive Disk

We have developed the 1D non-steady model to follow the disk evolution, taking into account the mass supply from the surrounding accretion envelope. In our model, the disk becomes more massive than the central star soon after the protostellar birth as the accretion rate through the disk is ~ 10 times lower than the mass supply rate from the

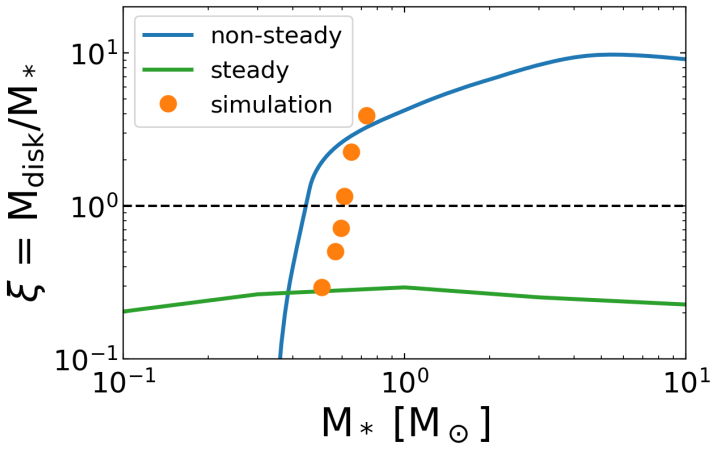

Figure 3.13: Comparisons between the non-steady model (blue line) and simulation (orange data) on the evolution of the disk-to-star mass ratio $\xi = M_{\rm disk}/M_*$. In further comparison, the evolution in the 1D steady disk model by Tanaka & Omukai (2014) is also presented by the green line. The horizontal dashed line denotes $\xi = 1$, i.e., when the disk and star have the same masses. This figure is taken from Kimura et al. (2021).

envelope. Additionally, we have confirmed that this trend is consistent with the evolution observed in the 3D simulation.

Previous studies show that a specific effect plays a significant role in the gravitational stability of the disk much more massive than the central star (e.g., Kratter & Lodato, 2016). When the disk is sufficiently massive, the protostar no longer stays at the mass center of the system due to the gravitational force from the perturbed disk. It has been known that the perturbation with $m = 1$ mode rapidly grows in such a case, even if the Toomre Q parameter is well above unity (SLING instability, e.g., Adams et al., 1989; Shu et al., 1990). Although linear analyses alone do not predict that the SLING instability inevitably results in the fragmentation, numerical simulations for the present-day star formation show that the disk fragmentation generally occurs when the disk-to-star mass ratio ξ is above unity (Kratter et al., 2010).

To study whether the SLING instability is active in our 3D simulation, we analyze the disk structure before the fragmentation, following the methodology of Krumholz et al. (2007). We calculate the power c_m of the disk spiral arms as follows:

$$c_m = \frac{1}{2\pi} \int_{-\pi}^{\pi} d\phi \int_0^{\infty} d\varpi e^{im\phi} \varpi \Sigma. \tag{3.42}$$

Figure 3.14 shows the normalized power $|c_m|^2/|c_0|^2$ for modes $m = 1$–10 derived for the different epochs corresponding to the snapshots in Figure3.10(a) and (b). We find that the $m = 1$ spiral mode is dominant, and odd modes are always stronger than even modes. As the evolution proceeds toward the fragmentation, the contrast between even and odd modes is amplified. This feature is also observed in Krumholz et al. (2007) and is a possible signature of the SLING instability.

As mentioned above, the SLING instability promotes the growth of the perturbation with $m = 1$ mode, but it does not necessarily result in the fragmentation. Although the fragmentation condition is still under debate, many authors have investigated the

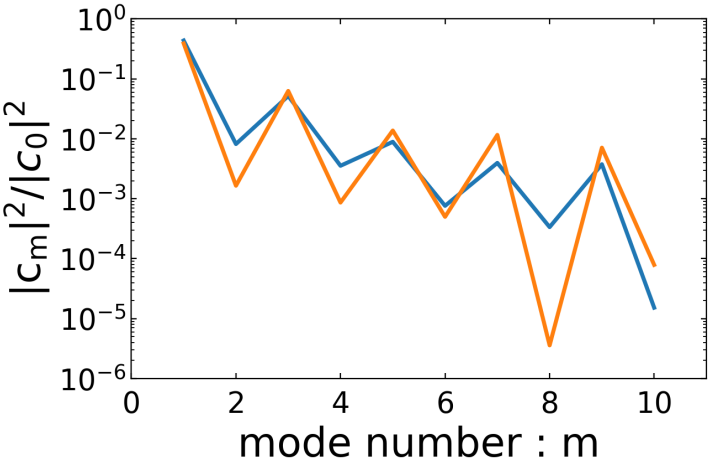

Figure 3.14: Normalized power $|c_m|^2/|c_0|^2$ in azimuthal modes m in the disk calculated with the simulation data. The blue and orange lines denote the snapshots at the epochs of 50 and 100 yr after the protostar formation, the same as in Figure 3.10(a) and (b). This figure is taken from Kimura et al. (2021).

condition (Gammie, 2001; Rice et al., 2003; Tsukamoto et al., 2015; Takahashi et al., 2016; Inoue & Yoshida, 2018, 2020). Especially, Takahashi et al. (2016) analytically derive the fragmentation condition for self-gravitating spiral arms forming in circumstellar disks, which is consistent with their 2D simulation results. Inoue & Yoshida (2020) modify the condition of Takahashi et al. (2016) considering disk thickness and shearing motion and apply it to the cosmological simulation performed by Greif et al. (2012). They demonstrate that the disk fragmentation in primordial star formation can also be explained within essentially the same framework. Nonetheless, it remains unclear which mechanism leads to the spiral arms that meet their fragmentation condition. Our results suggest that, in the primordial star formation, the disk becomes massive due to the significantly lower stellar accretion rate compared to the mass supply rate from the envelope, which triggers the SLING instability and results in the formation of such spiral arms.

3.4.2 Resolution Dependence

In our 1D disk model, the disk mass generally becomes larger than the central stellar mass before the stellar mass reaches 1 $M_\odot$ (see Section 3.2). We here note that the disk-to-star mass ratio $\xi = M_{\rm disk}/M_*$ is significantly dependent on the resolution. In Figure 3.15, we show the evolution of ξ with the different locations of the inner boundary, 0.01 AU, 0.1 AU, and 1 AU. The same envelope structure as in the fiducial case is assumed for these experimental runs, i.e., $K = K_{\rm fid}$ and $f_{\rm Kep} = 0.5$. In the case with the smallest boundary at 0.01 AU (the solid blue line), ξ reaches unity early at $M_{\simeq}0.03M_\odot$. In contrast, with the largest boundary at 1 AU (the solid green line), $\xi \simeq 1$ when the stellar mass is larger, at $M_* \simeq 0.7\ M_\odot$. Note that this variation is not attributed to the different disk evolutions caused by the changes in the inner radius. To show this, we perform two additional computational runs in which the inner boundary is fixed at 0.01 AU but the disk mass inside 0.1 AU (1 AU) is regarded as a part of the central stellar mass. The blue dashed and dot-dashed lines in Figure 3.15 denote these cases. These lines agree well with the orange and green lines, suggesting that the disk evolution is insensitive to the inner

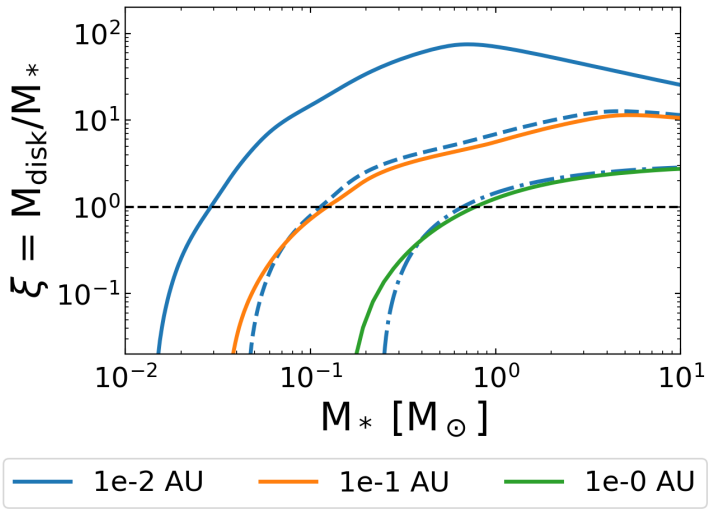

Figure 3.15: Effects of varying the inner boundary radius in 1D non-steady models. Plotted are the evolution of the disk-to-star mass ratio $\xi = M_{\rm disk}/M_*$ with the same envelope structure as in the fiducial case (Section 3.2.1) with different inner boundary positions, 0.01 AU (blue), 0.1 AU (orange) and 1 AU (green). The blue dashed and dot-dashed lines represent ξ when we regard the disk mass inside 0.1 AU and 1 AU as the stellar mass using the same inner boundary at 0.01 AU. This figure is taken from Kimura et al. (2021).

boundary radius.

In the 1D model, we can set an arbitrarily small inner boundary position. However, its minimum value should be physically limited by the location of the stellar surface. Stellar evolution calculations indicate that the protostellar radius evolves depending on the accretion histories (e.g., Stahler et al., 1980; Omukai & Palla, 2001, 2003; Hosokawa & Omukai, 2009b). For typical primordial star formation cases, where the accretion rate ranges in $\sim 10^{-3}$–10^{-2} $M_\odot {\rm yr}^{-1}$, the evolution of the stellar radius can be well approximated by

$$R_* \simeq 26\ R_\odot \left(\frac{M_*}{M_\odot}\right)^{0.27} \left(\frac{\dot{M}_*}{10^{-3} M_\odot {\rm yr}^{-1}}\right)^{0.41}, \tag{3.43}$$

during so-called the early adiabatic accretion stage for $M* \lesssim 10\ M_\odot$ (Stahler et al., 1986). Since the above value corresponds to $R_* \sim 0.1$ AU, our default choice of 0.1 AU for the inner boundary position in Section3.2 is justified. In Figure3.15, the orange line denotes this most realistic case.

On the other hand, 3D simulations also have resolution dependence. However, as Greif et al. (2012) follow an early evolution of the protostellar accretion even resolving the stellar interior structure, it is reasonable to consider their high-resolution simulations as the most realistic ones among the previous simulations. They demonstrate that the disks fragment early when the stellar masses are only 0.1–0.3 $M_\odot$ for all their examined cosmological mini-halos. This early fragmentation agrees well with the implication of our non-steady model that the disk becomes massive quite early, leading to the fragmentation, as discussed in Section 3.4.1.

The above discussion strongly suggests that the early disk fragmentation is inevitable. Although this makes the 1D disk models inapplicable to the later evolution, it is not

necessarily the case. Extending 1D models should still be valuable for situations where the disk fragmentation is suppressed or delayed by some processes, such as mass and angular momentum transfer via magnetic forces (e.g., Machida & Doi, 2013). It is also possible that a binary system surrounded by a global disk appears due to the fragmentation event (e.g., Sugimura et al., 2020). Semi-analytic modeling of such circumbinary disks is to be studied to elucidate the mass growth of the binary systems.

3.5 Summary and Conclusion

We have developed a 1D semi-analytical disk model surrounding a primordial protostar, accounting for mass supply from an envelope onto the disk. We do not assume steady accretion throughout the disk. In our model, the mass accretion rates within the disk are neither constant nor equivalent to the mass supply rate from the envelope. We have systematically investigated how the disk evolution changes with various mass supply rates from the envelope and angular momentum of the infalling gas onto the disk. Additionally, we have examined to what extent the non-steady model explains the disk evolution observed in a high-resolution 3D simulation, where the disk fragments when the protostellar mass is below 1 $M_\odot$.

First, we have investigated the fiducial case, in which we assume the typical envelope structure observed in 1D hydrodynamical calculations following the gravitational collapse of the cloud (Omukai & Nishi, 1998). In our model, a self-gravitating disk grows and evolves around the protostar. The gravitational torque controls the mass and angular momentum transfer, ensuring the Toomre Q parameter remains close to unity almost everywhere in the disk. We find that the accretion rate onto the star is an order of magnitude lower than the mass supply rate from the envelope. Consequently, the disk mass becomes larger than the protostellar mass before the star accretes the gas of $0.1M_\odot$. Such an evolution has not been observed in the previous steady disk models (e.g., Tanaka & Omukai, 2014).

We have also established an analytical model to reveal why only a minor fraction of the gas supplied from the envelope onto the disk accretes onto the central star. We show that a significant fraction of the mass supply is used to extend the disk outer edge. Such evolution occurs because the gas infalling onto the disk later has larger angular momentum, which is predetermined by the envelope structure. The analytical model predicts that the accretion rate onto the star is about one-tenth of the mass supply rate from the envelope, which is consistent with our 1D non-steady model.

We have next investigated the parameter dependence of the disk evolution in the 1D model by changing the mass supply rate from the envelope and its rotational degree. We find that the disk is more gravitationally unstable with the larger mass supply rate. This trend has already been seen in previous studies (Matsukoba et al., 2019). The disk structure is almost the same for various rotational strengths of the envelope, except that the disk size is larger with the higher angular momentum of the envelope. Regardless of some variations, the accretion rate onto the star is much lower than the mass supply rate from the envelope in all cases. As a result, the disk-to-star mass ratio ξ generally exceeds unity before the stellar mass reaches $\sim 1\ M_\odot$.

To validate our 1D model, we have additionally compared it with a 3D hydrodynamic simulation. For this purpose, we have newly performed a high-resolution simulation following the early disk evolution in the accretion phase with a modified version of the AMR code SFUMATO-RT (Matsumoto, 2007; Sugimura et al., 2020). Our simulation run re-

veals that the disk fragmentation takes place before the stellar mass reaches 1 $M_\odot$, which is consistent with the previous simulations (e.g., Clark et al., 2011). The disk-to-star mass ratio ξ reaches $\simeq 4$ immediately before the fragmentation, which is in good agreement with the evolution described by the 1D model. The overall structure of the self-gravitating disk is also similar between the simulation and the model, although the temperature in the simulation is roughly twice higher than that in the model.

We have shown that both the 1D non-steady model and 3D simulation exhibit the emergence of the massive disk soon after the birth of the protostar. We argue that the formation of such a massive disk triggers the early disk fragmentation, as commonly observed in the previous 3D simulations. Interestingly, the formation of the disk more massive than the central star occurs even in the present-day star formation (e.g., Inutsuka et al., 2010), despite the substantial difference in the thermal evolution of the star-forming gas. A comprehensive understanding of the massive disk formation, including the primordial and present-day cases, remains a subject for future research.

Chapter 4

3D Radiation Hydrodynamic Simulations Resolving the Structure of the Rapidly Accreting Primordial Protostars

In Section 2.3, we reviewed the formation processes of SMSs, which are possible origins of the observed high-redshift SMBHs. For SMS formation, it is necessary that radiative feedback does not effectively operate during the accretion phase. To estimate the strength of the protostellar radiation, we need to follow the protostellar evolution. The main methodology for studying its evolution has been 1D stellar evolution calculations (Hosokawa et al., 2012a; Umeda et al., 2016; Haemmerlé et al., 2018a). According to previous 1D calculations, protostars significantly expand and maintain low effective temperatures under the rapid accretion supposed in the DC scenario, which results in too weak radiative feedback to disturb the gas accretion.

However, these 1D models have some limitations. For example, they generally assume the hydrostatic balance for stellar materials and steady accretion flow for the surrounding environment. Moreover, it is challenging to model realistic 3D structures, such as stellar rotation induced by the angular momentum of the accretion flow. The protostellar spin should have an impact on the evolution as it triggers efficient chemical mixing within the stellar interior (Maeder, 1987; Brott et al., 2011). Additionally, fast rotation can lead to the $\Omega\Gamma$-limit, which may halt the mass accretion through the surrounding disk (Maeder & Meynet, 2000; Lee & Yoon, 2016; Takahashi & Omukai, 2017; Haemmerlé et al., 2018b). Therefore, the actual protostellar evolution and resulting feedback may be different from predictions by previous 1D calculations.

For elucidating the realistic 3D protostellar evolution, 3D RHD simulations are necessary. Luo et al. (2018) perform 3D RHD simulations following an early protostellar evolution in the SMS formation, with the flux-limited diffusion approximation, resolving the internal structure of the protostar. They find that the increasing pressure dissolves the protostar. This evolution is completely different from the previous 1D calculations. Further investigation is necessary for addressing how generally such evolution occurs and what 3D RHD effects may cause such evolution.

In this chapter, we perform 3D simulations with a newly developed RHD solver that employs an explicit M1 closure scheme, enabling us to resolve the protostellar interior. We present simulations starting from two different initial conditions: spherical and turbulent

clouds. We examine the idealized spherical case for comparisons to 1D calculations. Meanwhile, we study the turbulent case to reveal a realistic protostellar structure. In both cases, we follow the early protostellar evolution until a protostellar mass reaches $\sim 10\ M_\odot$.

The organization of this chapter is as follows. We present our numerical method in Section 4.1. In Section 4.2.1 and 4.2.2, we show our simulation results for the spherical and turbulent cases, respectively. The implication of our results is given in Section 4.3. Finally, we give summary in Section 4.4. We note that this chapter follows the author's work Kimura et al. (2023).

4.1 Numerical Method

4.1.1 Radiation Hydrodynamics Code

We employ the self-gravitational magneto-hydrodynamics code with AMR, SFUMATO-RT (Matsumoto, 2007; Matsumoto et al., 2015; Sugimura et al., 2020). SFUMATO-RT incorporates the primordial gas chemistry module, which is applicable only to a regime with a density lower than 10^{13} cm^{-3}. We add chemical reactions effective at high-density region (see also Sadanari et al., 2021). Furthermore, we implement the newly developed radiation solver with an explicit M1 closure scheme applicable even for the optically thick medium (Pomraning, 1969; Kershaw, 1976; Levermore, 1984; Rosdahl & Teyssier, 2015; Fukushima & Yajima, 2021). Our radiation solver incorporates the effect of the radiation force. We compute the local opacity consistent with the non-equilibrium chemistry, following the framework developed in Matsukoba et al. (2019). In this work, we do not use the ray-tracing radiation solver implemented by Sugimura et al. (2020).

Regarding the chemistry network, we calculate the non-equilibrium reactions among six species, H, H_2, H^+, H^-, H_2^+, and e^-, as in Sugimura et al. (2020). The fractional abundance of He is set to be $y_{\rm He} = 9.722 \times 10^{-2}$. We have added chemical reactions relevant in the dense medium with $n_{\rm H} \gtrsim 10^{13}{\rm cm}^{-3}$, following Omukai (2001). Our chemical network includes the photon emission and absorption processes, which allows us to solve the coupled evolution of the gas and radiation in the optically thick medium. We simultaneously update the gas temperature, chemical abundances, and radiation fields with the implicit method for computing their evolution consistently.

We develop a new explicit M1 closure scheme based on Rosdahl & Teyssier (2015). Their scheme is suitable for both the optically thin and thick domains, particularly for situations where the optical depth over a single grid cell is significantly larger than unity. We have improved their scheme to handle cases where the optical thickness rapidly changes across a few cells, which occurs near the protostellar surface in our simulations.

In the radiation solver, we consider two frequency bins: low energy ($h\nu < 13.6$ eV) and extreme-ultraviolet (EUV; $h\nu > 13.6$ eV). During SMS formation, the emission of the low-energy radiation is a dominant process in the cooling of the collapsing gas. Meanwhile, if the protostellar effective temperature increases to $\sim 10^5$ K, it emits a substantial amount of EUV photons, which ionize the surrounding gas and inhibit the gas accretion. Therefore, we need to take these two frequency bins to investigate the SMS formation. Moreover, we separately solve the photon energy and number densities for each frequency bin. Their ratio yields the photon mean energy. We locally reconstruct a consistent spectral distribution within each bin, assuming the Planck distribution for the temperature corresponding to the mean energy. This method improves our approximation

with only two bins, enabling us to accurately follow the radiation physics, such as heating by absorption. We note that the luminosity presented in Section4.2 is the sum of low-energy and EUV radiation.

4.1.2 Initial Conditions and Settings

One initial condition we consider is the "spherical" case, where we begin with an isothermal Bonner-Ebert sphere (Bonnar, 1956) whose central density and temperature are 10^9 cm^{-3} and 4.8×10^3 K. These values are realized on the SMS-evolution path by the one-zone model of the cloud collapse (Omukai, 2001). To ensure the collapse, we enhance the density profile by a factor of 1.6.

The other initial condition is the "turbulent" case, where we start from the same Bonner-Ebert sphere as above but with additional turbulent velocity fields. We set the power spectrum of the turbulence following the Larson's law, $P(k) \propto k^{-4}$, where k is the wavenumber (Larson, 1981), and its Mach number as unity. Recent studies demonstrate that the turbulence grows up to this level during the collapse phase (Federrath et al., 2011; Higashi et al., 2021).

The side length of the computational domain is 0.09 pc. This value is 3.3 times larger than the radius of the Bonner-Ebert sphere. The base grid consists of 40 cells in each direction, and we adaptively refine the grids to resolve the Jeans length with 8 cells. The resulting minimum cell size is 3.4×10^{-3} AU in the spherical case and 6.9×10^{-2} AU in the turbulent case. To prevent the artificial increase in entropy in the stellar interior, we prohibit the grid de-refinement.

As we employ the explicit M1 closure scheme, the time steps in simulations are restricted by the Courant-Friedrichs-Lewy condition with the speed of light (Gnedin & Abel, 2001; Skinner & Ostriker, 2013). To relax this restriction, we adopt the reduced speed of light approximation. We set the reduced light speed $\tilde{c}$ as $10^{-3}c$.

In our simulations, the emergence of a standing accretion shock marks the epoch of the protostellar birth (Omukai & Nishi, 1998). We define the stellar radius as the location where the radial velocity drops below the sound speed and the photospheric radius as where the optical depth measured from the outside reaches unity. The photospheric radius is often larger than the stellar radius, and the area between them is called a radiative precursor (Stahler et al., 1980). We regard the total mass within the stellar surface as the protostellar mass.

We follow the evolution for ~ 10 yr after the protostellar birth in both spherical and turbulent cases. Since the average accretion rates of the collapsing clouds are 1 $M_\odot \mathrm{yr}^{-1}$, protostars accrete the gas of ~ 10 $M_\odot$ until the end of the simulations. The spherical and turbulent simulation runs have taken 2 weeks with 896 cores and 2 months with 2000 cores, respectively.

4.2 Results

We show the final snapshots for the spherical and turbulent cases in Figure 4.1. In both cases, an accreting protostar with a mass of ~ 10 $M_\odot$ appears, and its radius is $\sim 10^3$ $R_\odot$. Nonetheless, we can see the significant differences between these cases. Especially the protostar rotates and has an oblate shape in the turbulent case. In the following sections, we provide a detailed view of the protostellar structure and evolution for each case.

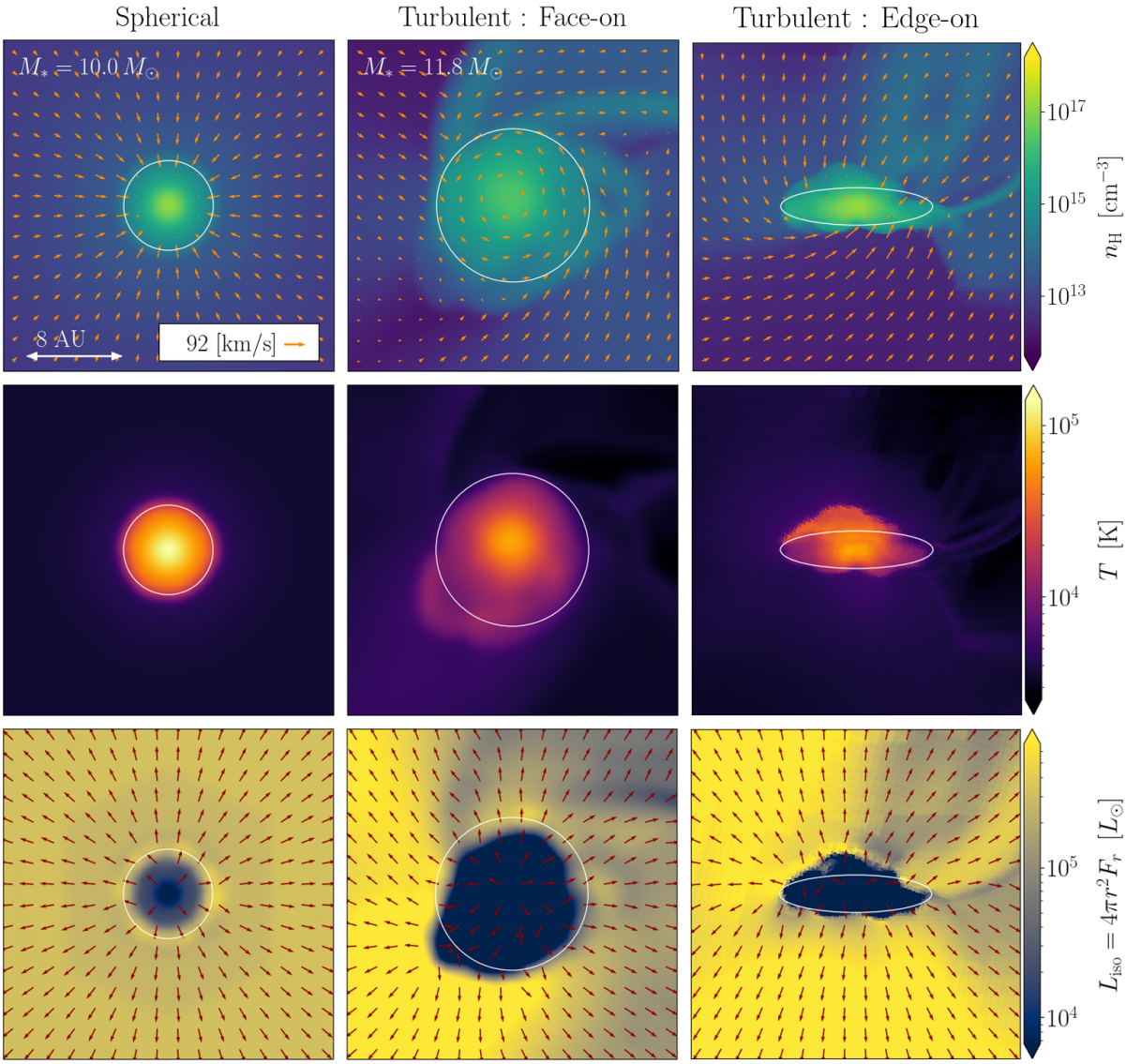

Figure 4.1: Snapshots at end of the simulation. The left column cprresponds to the spherical case. The middle and right columns display the face-on and edge-on slices in the turbulent case, respectively. The top, middle, and bottom panels show the distributions of the density, temperature, and isotropic luminosity $L_{\rm iso} \equiv 4\pi r^2 F_r$, where F_r is the local outward radiation flux. The isotropic luminosity is the flux intensity corrected for the geometrical dilution. In the top panels, we denote the velocity distributions by arrows. In the bottom panels, arrows indicate only the directions of the radiation flux. The white ellipses approximate the protostellar surfaces. This figure is taken from Kimura et al. (2023).

4.2.1 Spherical Case

In this case, the spherical symmetry is maintained throughout the evolution, as shown in Figure 4.1. We show the protostellar evolution in Figure 4.2. A protostar first appears at $M_* \sim 0.1\ M_\odot$. The top panel indicates that the stellar radius is $\simeq 10\ R_\odot$, much smaller than the photospheric radius of $\simeq 300\ R_\odot$. The protostellar radius is almost identical to the Jeans length when the collapsing gas becomes adiabatic at $n_{\rm H} \sim 10^{20}$ cm^{-3}

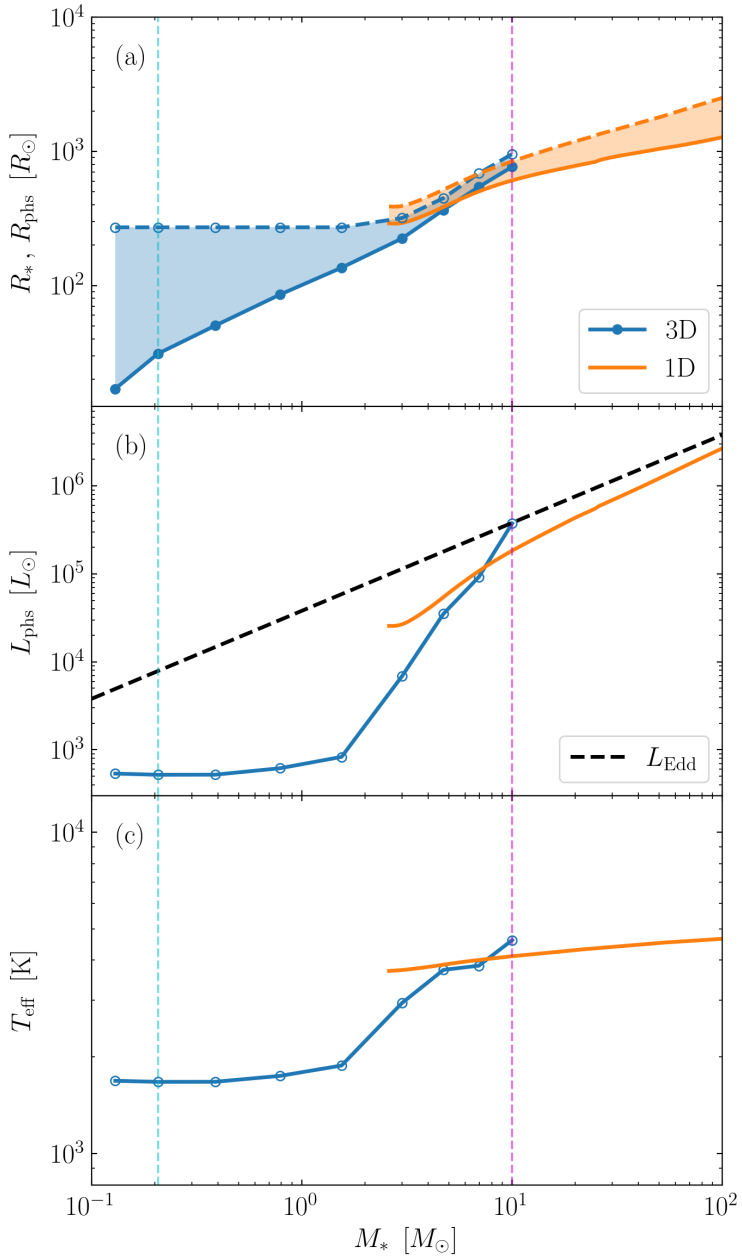

Figure 4.2: Stellar evolution in the spherical case. Each Panel shows the evolution of (a) protostellar radius R_* and photospheric radius $R_{\rm phs}$, (b) photospheric luminosity $L_{\rm phs}$, and (c) effective temperature $T_{\rm eff} \equiv (L_{\rm phs}/(4\pi R_{\rm phs}^2 \sigma_{\rm SB}))^{1/4}$, where $\sigma_{\rm SB}$ is the Stefan-Boltzmann constant, against the stellar mass M_*. In all the panels, the blue and orange colors indicate our 3D simulation and the 1D stellar evolution calculation at the constant accretion rate 1 $M_\odot {\rm yr}^{-1}$ taken from Hosokawa et al. (2012a). The open and filled circles represent the actual values evaluated from the simulation data. In panel (a), the solid and dashed lines denote the protostellar and photospheric radii, respectively. The shaded region corresponds to the radiative precursor. In panel (b), we plot the Eddington luminosity defined with the Thomson scattering cross section by the dashed line. The vertical cyan and magenta lines mark the epochs whose radial profiles are shown in Figure 4.3. This figure is taken from Kimura et al. (2023).

(Omukai, 2001), and the photospheric radius is determined by the envelope structure

created during the collapse. As the accretion continues, only the protostellar radius increases and becomes close to the photospheric radius. These radii grow in tandem for $M_* \gtrsim 3\ M_\odot$ after the stellar radius reaches $\sim 100\ R_\odot$. At this stage, the protostellar and photospheric radii are consistent with the 1D stellar evolution calculations from Hosokawa et al. (2012a), which assume the steady spherical accretion at a constant accretion rate of 1 $M_\odot \mathrm{yr}^{-1}$. We note that there are no 1D results in the range of $M_* \lesssim 2.5\ M_\odot$ due to the numerical difficulties in model construction. Hosokawa et al. (2012a) employed an arbitrary initial model with $M_* \simeq 2.5\ M_\odot$ and $R_* \simeq 298.4\ R_\odot$. Meanwhile, our 3D simulation follows the protostellar birth and its early evolution consistently with the cloud collapse.

We plot the luminosity evolution at the photosphere in the middle panel of Figure 4.2. During the initial phase, where $M_* \lesssim 2\ M_\odot$, the radiative precursor near the photosphere keeps its structure as that created during the collapse, leading to the constant luminosity of $\sim 5 \times 10^2\ L_\odot$. Subsequently, when $M_* \gtrsim 2\ M_\odot$, the photospheric radius expands. Along with this, the luminosity also increases and approaches the Eddington values. However, the radiative feedback has little impact on the accretion because the surrounding gas is neutral and its opacity is lower than the Thomson scattering value. The bottom panel presents the evolution of the effective temperature, $T_{\rm eff}$. Despite the substantial luminosities, $T_{\rm eff}$ takes low values of a few $\times 10^3$ K due to the large radius of the protostar. This evolution is consistent with the previous 1D calculation.

We show the spherically averaged radial profiles of physical quantities when the stellar mass reaches 0.2 $M_\odot$ and 10.0 $M_\odot$ in Figure 4.3. As seen in panels (a)–(c), the accretion shock exists at the stellar surface, where the inward velocity abruptly drops and both the density and temperature rise instead. Throughout the evolution, the stellar interior remains fully radiative, or convectively stable, which agrees with the 1D calculation for the early "adiabatic accretion" stage (see, for example, Hosokawa & Omukai, 2009a).

For comparison, we also present the profiles of 1D stellar evolution calculations by Hosokawa et al. (2012a), the snapshots at the epoch when the stellar mass reaches $\simeq$ 10 $M_\odot$ with the constant accretion rate of 1 $M_\odot \mathrm{yr}^{-1}$. Our results are consistent with the 1D calculations except for the deep stellar interior of $r \lesssim 0.1$ AU. The 1D calculations do not solve the initial core formation and, alternatively, assume an arbitrary initial model with 2.5 $M_\odot$. On the contrary, our 3D simulations follow the protostellar evolution consistently from the embryonic protostar with $\sim 0.1\ M_\odot$. This causes the different structures at the innermost part at $M_* \simeq 10\ M_\odot$.

As shown in panel (d), in the deep stellar interior the luminosity is small due to the slow diffusion. Each profile exhibits a local maximum near the stellar surface owing to the significant temperature gradient induced by the shock heating. When $M_* = 0.2\ M_\odot$, the luminosity in the radiative precursor increases outward because the H^- opacity decreases with the decreasing temperature. Additionally, at this time, the luminosity moderately increases further outward from the photosphere. This is attributed to the H^- free-bound emission, which serves as the dominant cooling process for the envelope gas. This cooling generates low energy ($h\nu < 13.6$ eV) radiation and contributes to the overall luminosity.

4.2.2 Turbulent Case

Figure 4.4 shows the protostellar evolution. As seen in the middle and right columns of Figure 4.1, the protostellar shape deviates from the spherical symmetry. In this section, we separately show the evolution in equatorial and polar directions. Panel (a) demonstrates

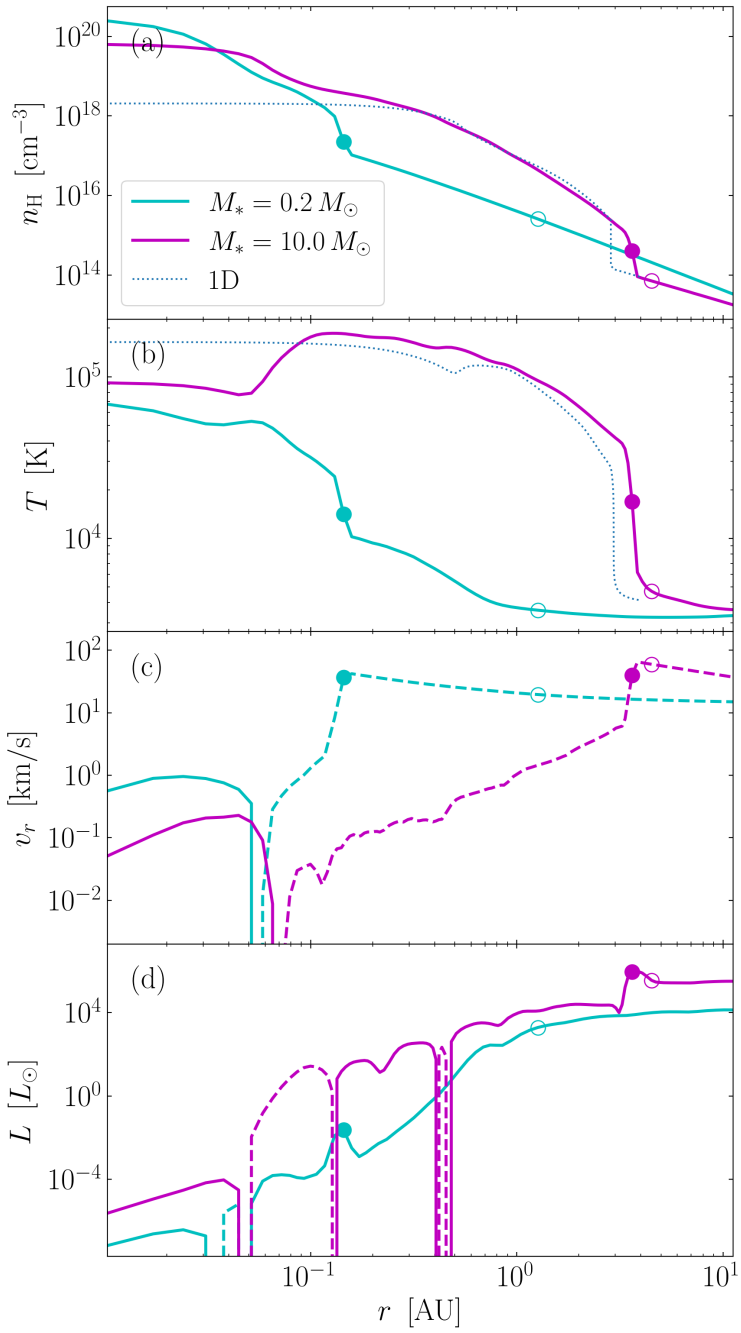

Figure 4.3: Spherically averaged radial profiles of physical quantities in the spherical case. The cyan and magenta lines denote represent different epochs when the stellar mass is 0.2 $M_\odot$ and 10.0 $M_\odot$. The filled and open circles indicate the protostellar and photospheric radii (see the top panel in Fig. 4.2). Each Panel shows the distributions of (a) gas number density, (b) temperature, (c) radial velocity, and (d) luminosity against the distance from the stellar center. In panels (c) and (d), the solid and dashed lines correspond to the outward and inward flux, respectively. In Panels (a) and (b), the dotted lines denote the 1D stellar evolution calculations by Hosokawa et al. (2012a), the profiles when the stellar mass increases to 10 $M_\odot$ with the constant accretion rate of 1 $M_\odot$yr^{-1}. This figure is taken from Kimura et al. (2023).

that both the stellar and photospheric radii increase with the increasing stellar mass. For

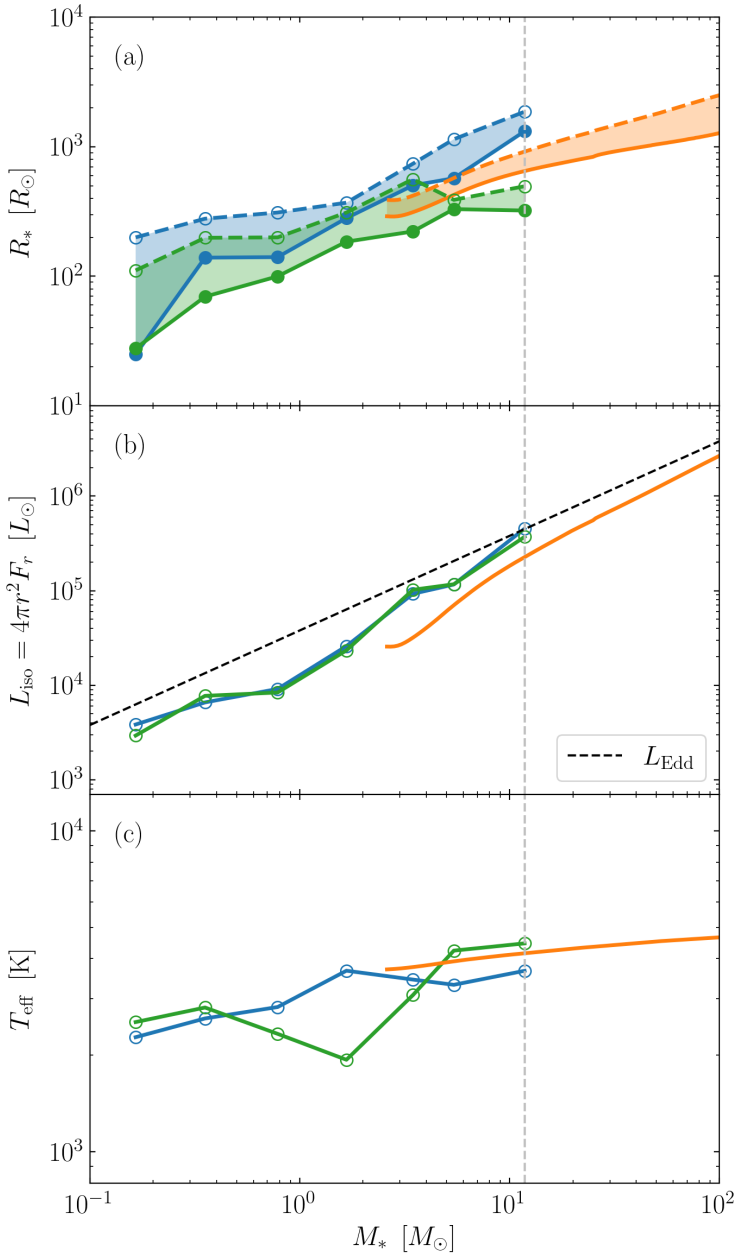

Figure 4.4: Stellar evolution in the turbulent case. Panels (a) and (c) present the same quantities as in Figure 4.2, and Panel (b) shows the isotropic luminosity. The blue and green circles denote the quantities in the equatorial and polar directions. In panel (a), the equatorial radii (blue) are those averaged over the equatorial plane. The polar radii (green) represent the minimum values on the polar axis, i.e., whether in the positive or negative directions. This definition allows us to avoid a temporal dense structure created by the turbulence and resulting spurious large radius. These equatorial and polar radii correspond to the ellipses in Figure 4.1. In panels (b) and (c), the equatorial and polar values denote those averaged over the region within $\pi/4$ radians from the equatorial plane and polar axis. The vertical dashed line corresponds to the epoch whose snapshots are shown in Figures 4.1 and 4.5. This figure is taken from Kimura et al. (2023)

$M_* \gtrsim 3\ M_\odot$, the stellar and photospheric radii are comparable to those in the previous 1D calculation. However, the rotation makes the equatorial radii more than twice as large

as the polar radii. The rapid protostellar rotation results in the centrifugal force almost equivalent to the pressure gradient force near the surface in the equatorial direction, which influences the equilibrium shape, as described below.

Panel (b) shows that, at the end of the simulation, the luminosity is almost identical to that in the 1D calculation and near the Eddington value. At this time, the radiative feedback is ineffective as the surrounding gas remains neutral, like in the spherical case. Although the radiative flux is anisotropic depending on the structure of the accreting gas (Figure 4.1), the average luminosity over the equatorial and polar regions is almost the same. Panel (c) indicates that the effective temperature always takes a few thousand Kelvin in agreement with the 1D calculation. Consequently, the EUV feedback is too weak to disrupt the rapid accretion onto the protostar.

We show snapshots at the end of the simulation when $M_* = 11.8\ M_\odot$ in the middle and right columns of Figure 4.1. While the turbulence complicates the gas structure around the protostar, the protostar rotates and has an oblate shape. This is because the accreting gas brings into the protostar the angular momentum of the initial turbulence. Furthermore, a circumstellar disk is beginning to form at this time. In our current definition of the stellar surface, which compares the radial velocity to the sound velocity, the white ellipse in Figure 4.1 approximately delineates a protostar. However, even within this ellipse, the gravity is counterbalanced by the centrifugal force, rather than the pressure gradient, in an outer region near the equatorial plane. From this perspective, such a region can be interpreted as a circumstellar disk. As shown in the middle panels, the stellar interior is much hotter than the surrounding gas, which remains nearly constant at several thousands of Kelvin with some fluctuations. Moreover, the top and bottom panels show that $L_{\rm iso}$ is anti-correlated with the density, indicating that the stellar radiation primarily escapes through low-density regions.

Figure 4.5 presents the radial profiles of physical quantities at the end of the simulation. As illustrated in Panel (a), the equatorial density is basically higher than the polar one due to the rotation. Panels (b) and (c) show that the radial infall velocity sharply declines and the temperature increases after the shock front.

As seen in Panel (d), $L_{\rm iso}$ profiles are similar for both equatorial and polar directions. In the deep stellar interior, the luminosity is very low because of the high optical depth. Outside the protostar, the luminosity is large enough that, in contrast to the case with $M_* = 0.2\ M_\odot$ in Figure 4.3, the emissivity of the infalling gas barely contributes to the overall luminosity.

We show the spherically averaged angular velocity distribution in Panel (e). For comparison, we also plot by the dashed line the Keplerian angular velocity $\Omega_{\rm Kep} = \sqrt{GM_r/r}$, where M_r denotes the mass enclosed within radius r. The angular velocity is nearly constant within the protostar, indicating rigid rotation. The protostellar rotational velocity is more than 0.4 times larger than the Keplerian velocity at any given radius. Notably, the rotational velocity is near the Keplerian value near the stellar surface at $r \simeq 5$ AU.

4.3 Discussions

We have developed a new RHD solver and investigated the protostellar evolution in SMS formation with 3D RHD simulations until its mass increases to $\sim 10 M_\odot$. Our simulations demonstrate that a swollen protostar steadily accretes mass and its radius gradually expands, which differs from the evolution shown in Luo et al. (2018). The discrepancy may be attributed to differences in the RHD solvers or initial conditions.

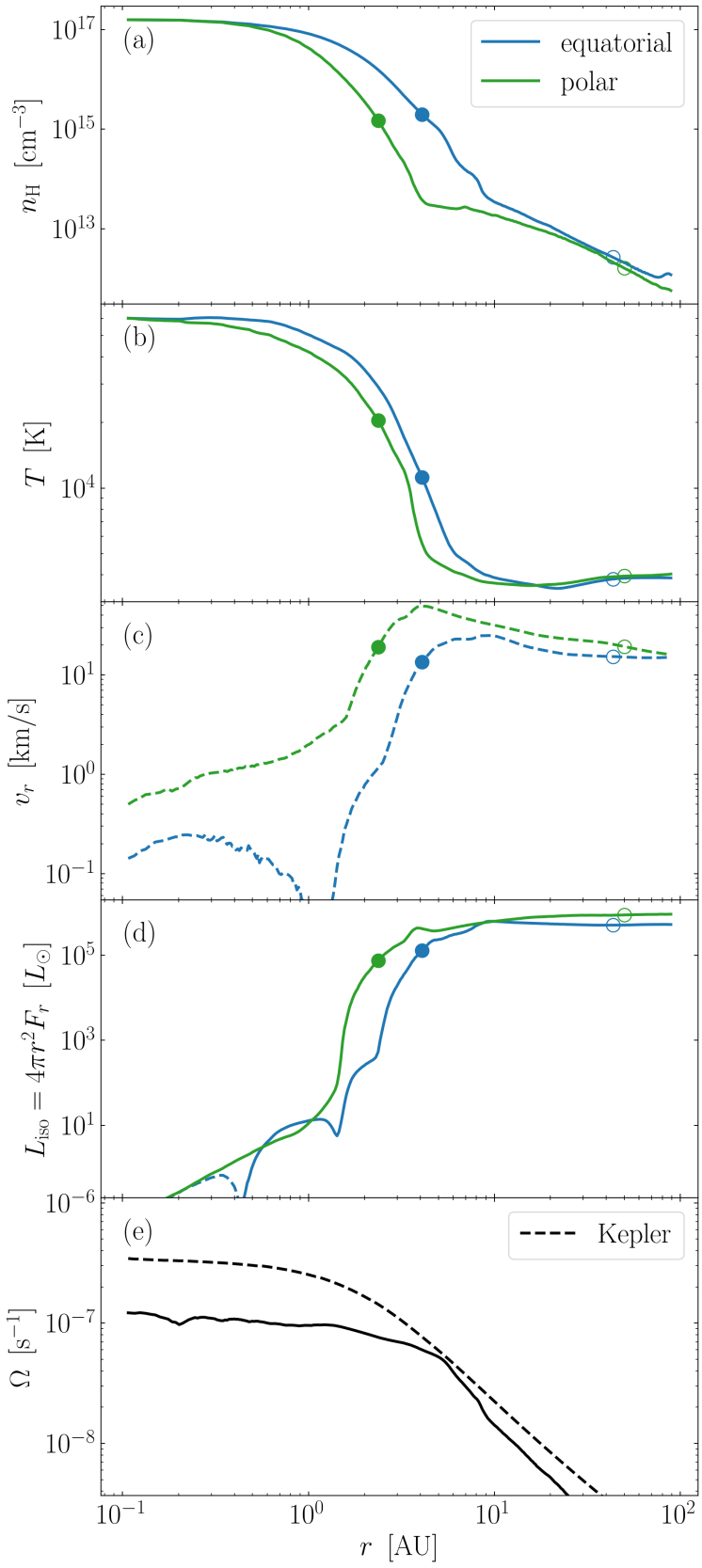

Figure 4.5: Radial profiles of physical quantities at the end of the turbulent case. Panels (a)–(d) show the same quantities as in Figure 4.3. The blue and green lines denote the averaged radial profiles over the region within $\pi/4$ radians from the equatorial plane and polar axis. The filled and open circles represent the protostellar and photospheric radii. Panel (e) presents the spherically averaged angular velocities compared to the Keplerian values. This figure is taken from Kimura et al. (2023)

However, the main reason is currently uncertain, and further investigation is necessary. As for protostellar rotation, our simulation shows the rigid rotation within the protostar and almost Keplerian motion near the stellar surface, which agrees with the trends observed in Greif et al. (2012) and Stacy et al. (2013). These studies examine the ordinal primordial star formation without solving the radiative transfer and show that protostars forming in various mini-halos typically have high spins. Both their and our results imply that primordial stars should be rapid rotators if no processes efficiently extract the angular momentum. The structure and evolution of such stars should differ from the non-rotating case.

While we stop our simulations when $M_* \sim 10\ M_\odot$, our code can follow the longer-term evolution if we implement nuclear fusion processes effective in the later stage ($M \gtrsim 50\ M_\odot$). This will directly reveal how the protostar evolves under the rapid rotation and whether it grows into a SMS as predicted by 1D stellar evolution calculations. The stellar rotation influences its evolution in various ways. First, it potentially induces instabilities generating turbulence, which leads to chemical mixing and alters the nuclear fusion rates and overall stellar structure (Maeder, 1987; Brott et al., 2011). Second, the rotation suppresses the general relativistic instability of SMSs and increases their maximum masses by an order of magnitude compared to the non-rotating cases (Haemmerlé, 2021). As a result, the seed BH masses can be elevated, which assists the formation of the observed high-redshift SMBHs.

At the end of our simulation, a circumstellar disk forms. The disk should continue to grow in both mass and size afterward. The disk accretion process onto a rapidly rotating SMS is still an open question. For example, Lee & Yoon (2016) suggest that the $\Omega\Gamma$ limit prohibits the gas accretion. Meanwhile, Takahashi & Omukai (2017) show the existence of steady disk accretion solutions for arbitrary angular momentum flux, implying that protostars can grow even under the $\Omega\Gamma$ limit. Although these works only rely on 1D models, our 3D RHD simulations can reveal the realistic disk structure and the accretion process. The circumstellar disk will also become gravitationally unstable and fragment (Becerra et al., 2015; Kimura et al., 2021). If some fragments migrate inward and merge with the central rotating protostar, the protostellar evolution may change with resulting highly fluctuating accretion rates (Sakurai et al., 2016). To elucidate the evolution of the star-disk system, further 3D RHD simulations investigating these effects are necessary.

4.4 Summary

In this chapter, we have examined the protostellar evolution under the rapid accretion supposed for the DC scenario, using 3D RHD simulations resolving the internal structure of the protostars. Our simulations employ the AMR code SFUMATO-RT, in which we have implemented a newly-developed RHD solver with an explicit M1 closure method. We follow the evolution for ~ 10 yr after the protostar formation, during which its mass reaches $\sim 10\ M_\odot$.

For the case starting from a spherical cloud, a swollen protostar forms as predicted by previous 1D stellar evolution calculations. At the end of the simulation when $M_* \sim 10\ M_\odot$, the stellar radius is $\sim 1000\ R_\odot$, the luminosity is $\sim 10^5\ L_\odot$, and the effective temperature is ~ 4000 K. Such protostars with the cool atmosphere emit few ionizing photons. As a result, the radiative feedback is too weak to halt the gas accretion.

In the other case starting from a turbulent cloud, a swollen protostar with high spin appears. It exhibits some different properties from the counterpart in the spherical case.

Due to the angular momentum supplied by the accreting gas, the protostar rotates at more than 0.4 times the Keplerian velocity throughout its interior. This rotation leads to the equatorial radius more than twice as large as the polar one. Also in this case, the protostellar effective temperature takes several thousand Kelvin, and the radiative feedback is ineffective.

We have followed the protostellar birth and its subsequent evolution for ~ 10 yr under the environment supposed for the DC scenario, which is merely the beginning of the evolution until the seed BH formation after $\sim$ Myr. Our 3D RHD simulations have a potential to reveal the realistic protostellar evolution in the later stage, which has been investigated only with 1D modeling so far.

Chapter 5

Summary and Future Directions

Since primordial stars are main drivers of the early cosmic evolution, great efforts have been devoted to elucidating their formation processes. Primordial stars form from the gravitational collapse of the pristine gas via H_2 molecular or H atomic cooling. The collapse with the H_2 cooling is typical in the early universe, and the literature suggests that the stellar masses range in $\sim 10^1$–10^3 $M_\odot$ in this case. Meanwhile, the H cooling can trigger the collapse under the environment where the H_2 cooling is suppressed. In this case, primordial stars are expected to grow to SMSs ($\sim 10^5$–10^6 $M_\odot$). Such SMSs are possible origins of observed high-redshift SMBHs. This formation pathway is called the DC scenario. In both the normal primordial star formation and the DC scenario, the gas infall from the envelope follows the collapse. Due to the angular momentum of the infalling gas, circumstellar disks generally emerge, and primordial protostars grow in mass via the disk accretion. In this thesis, we have studied the evolution of the circumstellar disk and protostellar structure during this accretion phase.

In Chapter 3, we have investigated the disk evolution around primordial stars using 1D non-steady disk model. Unlike the previous steady disk models, our model can follow the evolution of the disk and stellar masses consistently with the gas infall from the envelope. Especially, the disk-to-star mass ratio $\xi \equiv M_{\rm disk}/M_*$ is one of the indicators for the gravitational instability as well as the Toomre Q parameter. We find that the disk mass rapidly increases as the accretion rate onto the central star is an order of magnitude smaller than the mass supply rate from the envelope. As a result, ξ exceeds unity in the early stage when $M_* \lesssim 1$ $M_\odot$. This evolutionary feature is observed for various parameters covering the normal primordial star formation and the DC scenario. Moreover, using the 3D AMR hydrodynamics code SFUMATO-RT, we perform a simulation to confirm the evolution predicted by our 1D models. Our simulation demonstrates the disk fragmentation before the protostellar mass reaches 1 $M_\odot$. Moreover, we find that ξ reaches $\simeq 4$ immediately before the fragmentation. This evolution agrees with our 1D model. Our results suggest that the growth of a massive disk ubiquitously triggers the early disk fragmentation in the primordial star formation.

In Chapter 4, we have studied the protostellar evolution under the rapid gas accretion for the DC scenario with 3D RHD simulations. We have implemented a newly developed RHD solver that can solve the stellar interior in SFUMATO-RT. Our simulations follow the protostellar evolution until their masses reach ~ 10 $M_\odot$ from two different initial conditions of spherical and turbulent clouds. In both cases, giant protostars whose radii are ~ 1000 $R_\odot$ appear. Such swollen protostars have low effective temperatures and emit few ionizing photons, resulting in too weak radiative feedback to halt the gas accretion

up to the epoch examined in this work. Although previous 1D stellar evolution calculations predict this evolution, we demonstrate its realization in more realistic 3D RHD simulations for the first time. Moreover, we find that, in the turbulent case, the protostar rotates rapidly at more than 0.4 times Keplerian velocity due to the angular momentum of the accreting gas. We need to clarify the impacts of the rapid rotation on the ensuing protostellar evolution.

In this thesis, we have discussed the evolution of circumstellar disks and protostars separately. However, they originally influence each other. The accretion properties are significantly variable due to the disk fragmentation, and some fragments migrate inward and merge with the central protostar. It is still uncertain how such mergers change the 3D protostellar structure. The protostellar rotation also affects the disk structure through the boundary layer between the disk and the protostar. Furthermore, protostellar radiation may suppress disk fragmentation by heating the disk gas. We can follow the above star-disk interaction with our 3D RHD code. Actually, the circumstellar disk is about to emerge within our simulations presented in Chapter 4, and it should grow in mass and size afterward. We will extend our simulations to much longer time and reveal the evolution of the star-disk system in the future. Moreover, we also need to apply 3D RHD simulations to the normal primordial star formation for revealing their IMF.

Acknowledgement

First, I would like to express my deep gratitude to my supervisor, Takashi Hosokawa. He introduced me to the attractive theme, primordial star formation, and his attitude told me what researchers should be. This work would have been impossible without his continuous support. I also sincerely thank my collaborators, Kazuyuki Sugimura and Hajime Fukushima, for many fruitful discussions and comments, which drove my research. Furthermore, I gratefully acknowledge Tomoaki Matsumoto, the developer of the hydrodynamics code SFUMATO. Our 3D simulations in this thesis are based on his great code.

I appreciate Hidetoshi Omiya, Kota Hayashi, Tomoki Matsuoka, Yuh Tsuneto, and Taisuke Matsuda, who spend five years together as graduate students at Kyoto University. I also thank group members of Yukawa Institute for Theoretical Physics (YITP) and Theoretical Astrophysics Group for daily converstaion and seminar: Takahiro Tanaka, Kunihito Ioka, Kyutoku Kotaro, Yoshiyuki Yamada, Ryoki Matsukoba, Hamidani Hamid, Kazuya Takahashi, Wataru Ishizaki, Tomoki Wada, Saikat DAS. I thank all people who are interested in my works and discuss with me: Kazuyuki Omukai, Shinsuke Takasao, Kengo Tomida, Sanemichi Takahashi, Kengo Tomida, Koh Takahashi, Kei Tanaka, Kohei Inayoshi, Daisuke Toyouchi, Kazuhiro Shima, Chon Syunmon, Kenji Eric Sadanari.

Our 3D numerical simulations were carried out on XC50 Aterui II at the Center for Computational Astrophysics of the National Astronomical Observatory of Japan and Yukawa-21 at YITP of Kyoto University. I thank all people involved in the system maintenance of these machines.

This work is supported by JST SPRING, Grant Number JPMJSP2110, and the ANRI Fellowship. Their financial support was very helpful in carrying out my research.

I also thank all my friends who spend their holidays together and make me feel refleshed. Finally, I would like to express my greatest gratitude to my parents and grandparents for supporting me in numerous ways since I was born.

Appendix A

Ratio of Accretion Rate to Disk and Star

To derive Equation (3.41), we rewrite the second term on the right-hand side in Equation (3.39). To this end, we transform the quantities the second term includes, i.e., $\dot{M}_{\rm e,tot}$, c_s, Ω, and $d\varpi_{\rm d}/dt$, considering the structure of the accretion envelope and marginally stable ($Q \sim Q_{\rm crit}$) disk.

We suppose that the enclosed gas inside the radius $r_{\rm in}$ of the original accretion envelope has accreted onto the disk by the epoch considered. Assuming the mass distribution in the envelope presented by Equation (3.1) with $\gamma = 1.1$, we express the total mass of the accreted gas $M_{r_{\rm in}}$ as

$$\begin{aligned} M_{r_{\rm in}} &= M_{*,\rm ini} + \int_{r_*}^{r_{\rm in}} 4\pi r_{\rm in}^2 \rho dr \\ &\simeq \frac{36\pi}{7} C_1 K^{10/9} r_{\rm in}^{7/9}, \end{aligned} \tag{A.1}$$

where $M_{*,\rm ini}$ and r_* are the initial mass and radius of the protostar, and, for the second equality, we assume that $M_{r_{\rm in}} \gg M_{*,\rm ini}$ and $r_{\rm in} \gg r_*$. We denote the radius of the outer disk edge as $\varpi_{\rm d}$, similarly as in Section 3.2.1.2. The enclosed mass $M_{\varpi_{\rm d}}$ is thus written by

$$M_{\varpi_{\rm d}} = M_{r_{\rm in}}. \tag{A.2}$$

From the angular momentum conservation during the infall from the envelope onto the disk,

$$\sqrt{\varpi_{\rm d} G M_{\varpi_{\rm d}}} = f_{\rm Kep} \sqrt{r_{\rm in} G M_{r_{\rm in}}},$$

which leads to the relation between $\varpi_{\rm d}$ and $r_{\rm in}$,

$$\varpi_{\rm d} = f_{\rm Kep}^2 r_{\rm in}. \tag{A.3}$$

Using Equations (3.13), (A.1), (A.2), and (A.3), we can write the angular velocity Ω at the disk outer edge as

$$\Omega = 6\sqrt{\frac{\pi G}{7}} C_1^{1/2} K^{5/9} f_{\rm Kep}^{-7/9} \varpi_{\rm d}^{-10/9}. \tag{A.4}$$

We can obtain the relation between t and $r_{\rm in}$ from Equations (3.2) and (3.7), and $dr_{\rm in}/dt$ is expressed by

$$\frac{dr_{\rm in}}{dt} = \frac{9}{10} C_2 K^{5/9} r_{\rm in}^{-1/9}. \tag{A.5}$$

From Equation (A.3), we get

$$\frac{d\varpi_{\rm d}}{dt} = \frac{9}{10} C_2 K^{5/9} f_{\rm Kep}^{20/9} \varpi_{\rm d}^{-1/9}. \tag{A.6}$$

With Equations (3.1), (3.8), (A.3), and (A.5), the total mass supply rate from the envelope $\dot{M}_{\rm e,tot}$ is described as

$$\dot{M}_{\rm e,tot} = \frac{18\pi}{5} C_1 C_2 K^{5/3} f_{\rm Kep}^{2/3} \varpi_{\rm d}^{-1/3}. \tag{A.7}$$

From Equation (3.23) the surface density in the marginally stable disk with $Q \sim Q_{\rm crit}$ is

$$\Sigma \sim \frac{\Omega c_s}{\pi G Q_{\rm crit}}. \tag{A.8}$$

From Equations (3.4) and (3.28), the number density of hydrogen nuclei at the disk edge is

$$\begin{aligned} n_{\rm H} &= \frac{1}{m_{\rm H}} \frac{\Sigma}{\sqrt{2\pi} H} \\ &\sim \frac{M_{\varpi_{\rm d}}}{\sqrt{2\pi^3} m_{\rm H} Q_{\rm crit} \varpi_{\rm d}^3}, \end{aligned} \tag{A.9}$$

where we neglect $y_{\rm He}$ in Equation (3.4). The sound velocity c_s is written as $c_s = c_{s,1000}(T/1000\ {\rm K})^{1/2}$ where $c_{s,1000} = 3.3 \times 10^5$ cm/s is the sound velocity at $T = 1000$ K. With Equations (3.40) and (A.9), we can describe c_s as

$$c_s = 3.7 \times 10^5 \left(\frac{Q_{\rm crit}}{1.0}\right)^{-1/20} \left(\frac{f_T}{0.4}\right)^{1/2} \left(\frac{K}{K_{\rm fid}}\right)^{5/9} \left(\frac{f_{\rm Kep}}{0.5}\right)^{-7/90} \left(\frac{\varpi_{\rm d}}{1{\rm AU}}\right)^{-1/9} \ {\rm cm/s}. \tag{A.10}$$

Substituting Equations (A.4), (A.6), (A.7), and (A.10) into Equation (3.39), we finally get

$$\frac{\dot{M}_{\rm d,edge}}{\dot{M}_{\rm e,tot}} = 1 \ - \ 0.68 \left(\frac{Q_{\rm crit}}{1.0}\right)^{-21/20} \left(\frac{f_T}{0.4}\right)^{1/2} \left(\frac{f_{\rm Kep}}{0.5}\right)^{7/10}. \tag{A.11}$$

Bibliography

Abel, T., Anninos, P., Zhang, Y., & Norman, M. L. 1997, NewA, 2, 181, doi: 10.1016/S1384-1076(97)00010-9

Abel, T., Bryan, G. L., & Norman, M. L. 2002, Science, 295, 93, doi: 10.1126/science.295.5552.93

Adams, F. C., Ruden, S. P., & Shu, F. H. 1989, ApJ, 347, 959, doi: 10.1086/168187

Barkana, R., & Loeb, A. 2001, Physics reports, 349, 125

Becerra, F., Greif, T. H., Springel, V., & Hernquist, L. E. 2015, MNRAS, 446, 2380, doi: 10.1093/mnras/stu2284

Begelman, M. C. 1978, MNRAS, 184, 53, doi: 10.1093/mnras/184.1.53

Bertin, G. 2000, Dynamics of Galaxies

Binney, J., & Tremaine, S. 1987, Galactic dynamics

Boley, A. C., Mejía, A. C., Durisen, R. H., et al. 2006, ApJ, 651, 517, doi: 10.1086/507478

Bonnar, W. 1956, Monthly Notices of the Royal Astronomical Society, 116, 351

Boylan-Kolchin, M. 2023, Nature Astronomy, doi: 10.1038/s41550-023-01937-7

Bromm, V., Coppi, P. S., & Larson, R. B. 2002, ApJ, 564, 23, doi: 10.1086/323947

Bromm, V., & Loeb, A. 2003, ApJ, 596, 34, doi: 10.1086/377529

Brott, I., de Mink, S. E., Cantiello, M., et al. 2011, A&A, 530, A115, doi: 10.1051/0004-6361/201016113

Chandrasekhar, S. 1964, ApJ, 140, 417, doi: 10.1086/147938

Chon, S., & Hosokawa, T. 2019, MNRAS, 488, 2658, doi: 10.1093/mnras/stz1824

Chon, S., Hosokawa, T., & Yoshida, N. 2018, MNRAS, 475, 4104, doi: 10.1093/mnras/sty086

Clark, P. C., Glover, S. C. O., Smith, R. J., et al. 2011, Science, 331, 1040, doi: 10.1126/science.1198027

Federrath, C., Sur, S., Schleicher, D. R. G., Banerjee, R., & Klessen, R. S. 2011, ApJ, 731, 62, doi: 10.1088/0004-637X/731/1/62

Fernandez, R., Bryan, G. L., Haiman, Z., & Li, M. 2014, MNRAS, 439, 3798, doi: 10.1093/mnras/stu230

Fukushima, H., & Yajima, H. 2021, MNRAS, 506, 5512, doi: 10.1093/mnras/stab2099

Gammie, C. F. 2001, ApJ, 553, 174, doi: 10.1086/320631

Gnedin, N. Y., & Abel, T. 2001, NewA, 6, 437, doi: 10.1016/S1384-1076(01)00068-9

Greif, T. H., Bromm, V., Clark, P. C., et al. 2012, MNRAS, 424, 399, doi: 10.1111/j.1365-2966.2012.21212.x

Greif, T. H., White, S. D. M., Klessen, R. S., & Springel, V. 2011, ApJ, 736, 147, doi: 10.1088/0004-637X/736/2/147

Haemmerlé, L. 2021, A&A, 650, A204, doi: 10.1051/0004-6361/202140893

Haemmerlé, L., Woods, T. E., Klessen, R. S., Heger, A., & Whalen, D. J. 2018a, MNRAS, 474, 2757, doi: 10.1093/mnras/stx2919

—. 2018b, ApJL, 853, L3, doi: 10.3847/2041-8213/aaa462

Harikane, Y., Ono, Y., Ouchi, M., et al. 2022, ApJS, 259, 20, doi: 10.3847/1538-4365/ac3dfc

Hartwig, T., Volonteri, M., Bromm, V., et al. 2016, MNRAS, 460, L74, doi: 10.1093/mnrasl/slw074

Higashi, S., Susa, H., & Chiaki, G. 2021, ApJ, 915, 107, doi: 10.3847/1538-4357/ac01c7

Hirano, S., & Bromm, V. 2017, MNRAS, 470, 898, doi: 10.1093/mnras/stx1220

Hirano, S., Hosokawa, T., Yoshida, N., & Kuiper, R. 2017, Science, 357, 1375, doi: 10.1126/science.aai9119

Hirano, S., Hosokawa, T., Yoshida, N., Omukai, K., & Yorke, H. W. 2015, MNRAS, 448, 568, doi: 10.1093/mnras/stv044

Hirano, S., Hosokawa, T., Yoshida, N., et al. 2014, ApJ, 781, 60, doi: 10.1088/0004-637X/781/2/60

Hirasawa, T. 1969, Progress of Theoretical Physics, 42, 523

Hollenbach, D., & McKee, C. F. 1979, The Astrophysical Journal Supplement Series, 41, 555

Hong, J., Vesperini, E., Askar, A., et al. 2018, MNRAS, 480, 5645, doi: 10.1093/mnras/sty2211

Hosokawa, T., & Omukai, K. 2009a, ApJ, 703, 1810, doi: 10.1088/0004-637X/703/2/1810

—. 2009b, ApJ, 691, 823, doi: 10.1088/0004-637X/691/1/823

Hosokawa, T., Omukai, K., & Yorke, H. W. 2012a, ApJ, 756, 93, doi: 10.1088/0004-637X/756/1/93

Hosokawa, T., Omukai, K., Yoshida, N., & Yorke, H. W. 2011, Science, 334, 1250, doi: 10.1126/science.1207433

Hosokawa, T., Yorke, H. W., Inayoshi, K., Omukai, K., & Yoshida, N. 2013, ApJ, 778, 178, doi: 10.1088/0004-637X/778/2/178

Hosokawa, T., Yoshida, N., Omukai, K., & Yorke, H. W. 2012b, ApJL, 760, L37, doi: 10.1088/2041-8205/760/2/L37

Hubeny, I. 1990, ApJ, 351, 632, doi: 10.1086/168501

Hutchins, J. 1976, The Astrophysical Journal, 205, 103

Ilee, J. D., Cyganowski, C. J., Brogan, C. L., et al. 2018, ApJL, 869, L24, doi: 10.3847/2041-8213/aaeffc

Inayoshi, K., & Haiman, Z. 2014, MNRAS, 445, 1549, doi: 10.1093/mnras/stu1870

Inayoshi, K., Haiman, Z., & Ostriker, J. P. 2016, MNRAS, 459, 3738, doi: 10.1093/mnras/stw836

Inayoshi, K., Harikane, Y., Inoue, A. K., Li, W., & Ho, L. C. 2022, ApJL, 938, L10, doi: 10.3847/2041-8213/ac9310

Inayoshi, K., Omukai, K., & Tasker, E. 2014, MNRAS, 445, L109, doi: 10.1093/mnrasl/slu151

Inayoshi, K., Visbal, E., & Haiman, Z. 2020, ARA&A, 58, 27, doi: 10.1146/annurev-astro-120419-014455

Inoue, S., & Yoshida, N. 2018, MNRAS, 474, 3466, doi: 10.1093/mnras/stx2978

—. 2020, MNRAS, 491, L24, doi: 10.1093/mnrasl/slz160

Inutsuka, S.-i., Machida, M. N., & Matsumoto, T. 2010, ApJL, 718, L58, doi: 10.1088/2041-8205/718/2/L58

Inutsuka, S.-I., & Miyama, S. M. 1992, The Astrophysical Journal, 388, 392

Ishiyama, T., Sudo, K., Yokoi, S., et al. 2016, ApJ, 826, 9, doi: 10.3847/0004-637X/826/1/9

Jiang, Y.-F., Stone, J. M., & Davis, S. W. 2014, ApJ, 796, 106, doi: 10.1088/0004-637X/796/2/106

Johnston, K. G., Hoare, M. G., Beuther, H., et al. 2020, A&A, 634, L11, doi: 10.1051/0004-6361/201937154

Karpasb, Z., Anicich, V., & Huntress Jr, W. 1979, The Journal of Chemical Physics, 70, 2877

Kershaw, D. S. 1976, doi: 10.2172/104974

Kimura, K., Hosokawa, T., & Sugimura, K. 2021, ApJ, 911, 52, doi: 10.3847/1538-4357/abe866

Kimura, K., Hosokawa, T., Sugimura, K., & Fukushima, H. 2023, arXiv e-prints, arXiv:2303.12100, doi: 10.48550/arXiv.2303.12100

Kinugawa, T., Inayoshi, K., Hotokezaka, K., Nakauchi, D., & Nakamura, T. 2014, MNRAS, 442, 2963, doi: 10.1093/mnras/stu1022

Kratter, K., & Lodato, G. 2016, ARA&A, 54, 271, doi: 10.1146/annurev-astro-081915-023307

Kratter, K. M., Matzner, C. D., Krumholz, M. R., & Klein, R. I. 2010, ApJ, 708, 1585, doi: 10.1088/0004-637X/708/2/1585

Krumholz, M. R., Klein, R. I., & McKee, C. F. 2007, ApJ, 656, 959, doi: 10.1086/510664

Kumamoto, J., Fujii, M. S., & Tanikawa, A. 2020, MNRAS, 495, 4268, doi: 10.1093/mnras/staa1440

Larson, R. B. 1969, MNRAS, 145, 271, doi: 10.1093/mnras/145.3.271

—. 1981, MNRAS, 194, 809, doi: 10.1093/mnras/194.4.809

Latif, M. A., Khochfar, S., & Whalen, D. 2020, ApJL, 892, L4, doi: 10.3847/2041-8213/ab7c61

Latif, M. A., & Schleicher, D. R. G. 2015, A&A, 578, A118, doi: 10.1051/0004-6361/201525855

Latif, M. A., Schleicher, D. R. G., Schmidt, W., & Niemeyer, J. 2013, MNRAS, 433, 1607, doi: 10.1093/mnras/stt834

Lee, H., & Yoon, S.-C. 2016, ApJ, 820, 135, doi: 10.3847/0004-637X/820/2/135

Levermore, C. D. 1984, JQSRT, 31, 149, doi: 10.1016/0022-4073(84)90112-2

Liu, B., Meynet, G., & Bromm, V. 2020, arXiv e-prints, arXiv:2010.05824. https://arxiv.org/abs/2010.05824

Luo, Y., Ardaneh, K., Shlosman, I., et al. 2018, MNRAS, 476, 3523, doi: 10.1093/mnras/sty362

Lynden-Bell, D., & Kalnajs, A. 1972, Monthly Notices of the Royal Astronomical Society, 157, 1

Lynden-Bell, D., & Pringle, J. E. 1974, MNRAS, 168, 603, doi: 10.1093/mnras/168.3.603

Machida, M. N., & Doi, K. 2013, MNRAS, 435, 3283, doi: 10.1093/mnras/stt1524

Maeder, A. 1987, A&A, 178, 159

Maeder, A., & Meynet, G. 2000, A&A, 361, 159, doi: 10.48550/arXiv.astro-ph/0006405

Matsukoba, R., Takahashi, S. Z., Sugimura, K., & Omukai, K. 2019, MNRAS, 484, 2605, doi: 10.1093/mnras/sty3522

Matsukoba, R., Vorobyov, E. I., Sugimura, K., Hosokawa, S. C. T., & Omukai, K. 2020, MNRAS, doi: 10.1093/mnras/staa3462

Matsumoto, T. 2007, PASJ, 59, 905, doi: 10.1093/pasj/59.5.905

Matsumoto, T., Dobashi, K., & Shimoikura, T. 2015, ApJ, 801, 77, doi: 10.1088/0004-637X/801/2/77

Mayer, M., & Duschl, W. J. 2005, MNRAS, 358, 614, doi: 10.1111/j.1365-2966.2005.08826.x

McKee, C. F., & Tan, J. C. 2008, ApJ, 681, 771, doi: 10.1086/587434

Ohsuga, K., Mori, M., Nakamoto, T., & Mineshige, S. 2005, ApJ, 628, 368, doi: 10.1086/430728

Omukai, K. 2001, ApJ, 546, 635, doi: 10.1086/318296

Omukai, K., & Nishi, R. 1998, ApJ, 508, 141, doi: 10.1086/306395

Omukai, K., & Palla, F. 2001, ApJL, 561, L55, doi: 10.1086/324410

—. 2003, ApJ, 589, 677, doi: 10.1086/374810

Omukai, K., Tsuribe, T., Schneider, R., & Ferrara, A. 2005, ApJ, 626, 627, doi: 10.1086/429955

Palla, F., & Stahler, S. W. 1990, ApJL, 360, L47, doi: 10.1086/185809

Penston, M. V. 1969, MNRAS, 144, 425, doi: 10.1093/mnras/144.4.425

Planck Collaboration, Aghanim, N., Akrami, Y., et al. 2020, A&A, 641, A6, doi: 10.1051/0004-6361/201833910

Pomraning, G. C. 1969, JQSRT, 9, 407, doi: 10.1016/0022-4073(69)90036-3

Regan, J. A., & Downes, T. P. 2018, MNRAS, 475, 4636, doi: 10.1093/mnras/sty134

Rice, W. K. M., Armitage, P. J., Bate, M. R., & Bonnell, I. A. 2003, MNRAS, 339, 1025, doi: 10.1046/j.1365-8711.2003.06253.x

Ripamonti, E., & Abel, T. 2004, MNRAS, 348, 1019, doi: 10.1111/j.1365-2966.2004.07422.x

Robertson, B. E., Ellis, R. S., Dunlop, J. S., McLure, R. J., & Stark, D. P. 2010, Nature, 468, 49, doi: 10.1038/nature09527

Rosdahl, J., & Teyssier, R. 2015, MNRAS, 449, 4380, doi: 10.1093/mnras/stv567

Sadanari, K. E., Omukai, K., Sugimura, K., Matsumoto, T., & Tomida, K. 2021, MNRAS, 505, 4197, doi: 10.1093/mnras/stab1330

Sakurai, Y., Vorobyov, E. I., Hosokawa, T., et al. 2016, MNRAS, 459, 1137, doi: 10.1093/mnras/stw637

Seaton, M. J., Yan, Y., Mihalas, D., & Pradhan, A. K. 1994, MNRAS, 266, 805, doi: 10.1093/mnras/266.4.805

Shakura, N. I., & Sunyaev, R. A. 1973, A&A, 500, 33

Shapiro, P. R., & Kang, H. 1987, Symposium - International Astronomical Union, 117, 365, doi: 10.1017/s0074180900150521

Shapiro, S. L., & Teukolsky, S. A. 1983, Black holes, white dwarfs, and neutron stars : the physics of compact objects

Shibata, M., & Shapiro, S. L. 2002, ApJL, 572, L39, doi: 10.1086/341516

Shu, F. H., Tremaine, S., Adams, F. C., & Ruden, S. P. 1990, ApJ, 358, 495, doi: 10.1086/169003

Skinner, M. A., & Ostriker, E. C. 2013, ApJS, 206, 21, doi: 10.1088/0067-0049/206/2/21

Stacy, A., & Bromm, V. 2014, ApJ, 785, 73, doi: 10.1088/0004-637X/785/1/73

Stacy, A., Greif, T. H., & Bromm, V. 2010, MNRAS, 403, 45, doi: 10.1111/j.1365-2966.2009.16113.x

—. 2012, MNRAS, 422, 290, doi: 10.1111/j.1365-2966.2012.20605.x

Stacy, A., Greif, T. H., Klessen, R. S., Bromm, V., & Loeb, A. 2013, MNRAS, 431, 1470, doi: 10.1093/mnras/stt264

Stahler, S. W., Palla, F., & Salpeter, E. E. 1986, ApJ, 302, 590, doi: 10.1086/164018

Stahler, S. W., Shu, F. H., & Taam, R. E. 1980, ApJ, 241, 637, doi: 10.1086/158377

Stecher, T. P., & Williams, D. A. 1967, ApJL, 149, L29, doi: 10.1086/180047

Sugimura, K., Matsumoto, T., Hosokawa, T., Hirano, S., & Omukai, K. 2020, ApJL, 892, L14, doi: 10.3847/2041-8213/ab7d37

Sugimura, K., Mizuno, Y., Matsumoto, T., & Omukai, K. 2017, MNRAS, 469, 4022, doi: 10.1093/mnras/stx1129

Takahashi, S. Z., Inutsuka, S.-i., & Machida, M. N. 2013, ApJ, 770, 71, doi: 10.1088/0004-637X/770/1/71

Takahashi, S. Z., & Omukai, K. 2017, MNRAS, 472, 532, doi: 10.1093/mnras/stx1988

Takahashi, S. Z., Tsukamoto, Y., & Inutsuka, S. 2016, MNRAS, 458, 3597, doi: 10.1093/mnras/stw557

Tan, J. C., & McKee, C. F. 2004, ApJ, 603, 383, doi: 10.1086/381490

Tanaka, K. E. I., & Omukai, K. 2014, MNRAS, 439, 1884, doi: 10.1093/mnras/stu069

Tanikawa, A., Susa, H., Yoshida, T., Trani, A. A., & Kinugawa, T. 2020, arXiv e-prints, arXiv:2008.01890. https://arxiv.org/abs/2008.01890

Tegmark, M., Silk, J., Rees, M. J., et al. 1997, The Astrophysical Journal, 474, 1

Tobin, J. J., Kratter, K. M., Persson, M. V., et al. 2016, Nature, 538, 483, doi: 10.1038/nature20094

Toomre, A. 1964, The Astrophysical Journal, 139, 1217, doi: 10.1086/147861

Tsukamoto, Y., Takahashi, S. Z., Machida, M. N., & Inutsuka, S. 2015, MNRAS, 446, 1175, doi: 10.1093/mnras/stu2160

Turk, M. J., Abel, T., & O'Shea, B. 2009, Science, 325, 601, doi: 10.1126/science.1173540

Umeda, H., Hosokawa, T., Omukai, K., & Yoshida, N. 2016, ApJL, 830, L34, doi: 10.3847/2041-8205/830/2/L34

Vandervoort, P. O. 1970, ApJ, 161, 87, doi: 10.1086/150514

Volonteri, M. 2010, A&A Rv, 18, 279, doi: 10.1007/s00159-010-0029-x

Wise, J. H., Regan, J. A., O'Shea, B. W., et al. 2019, Nature, 566, 85, doi: 10.1038/s41586-019-0873-4

Wolcott-Green, J., Haiman, Z., & Bryan, G. L. 2017, MNRAS, 469, 3329, doi: 10.1093/mnras/stx167

—. 2021, MNRAS, 500, 138, doi: 10.1093/mnras/staa3057

Woods, T. E., Agarwal, B., Bromm, V., et al. 2019, PASA, 36, e027, doi: 10.1017/pasa.2019.14

Yoshida, N., Omukai, K., & Hernquist, L. 2007, ApJL, 667, L117, doi: 10.1086/522202

Yoshida, N., Omukai, K., Hernquist, L., & Abel, T. 2006, ApJ, 652, 6, doi: 10.1086/507978

Zeldovich, Y. B., & Novikov, I. D. 1971, Relativistic astrophysics. Vol.1: Stars and relativity

Zhu, Z., Hartmann, L., & Gammie, C. 2010, ApJ, 713, 1143, doi: 10.1088/0004-637X/713/2/1143